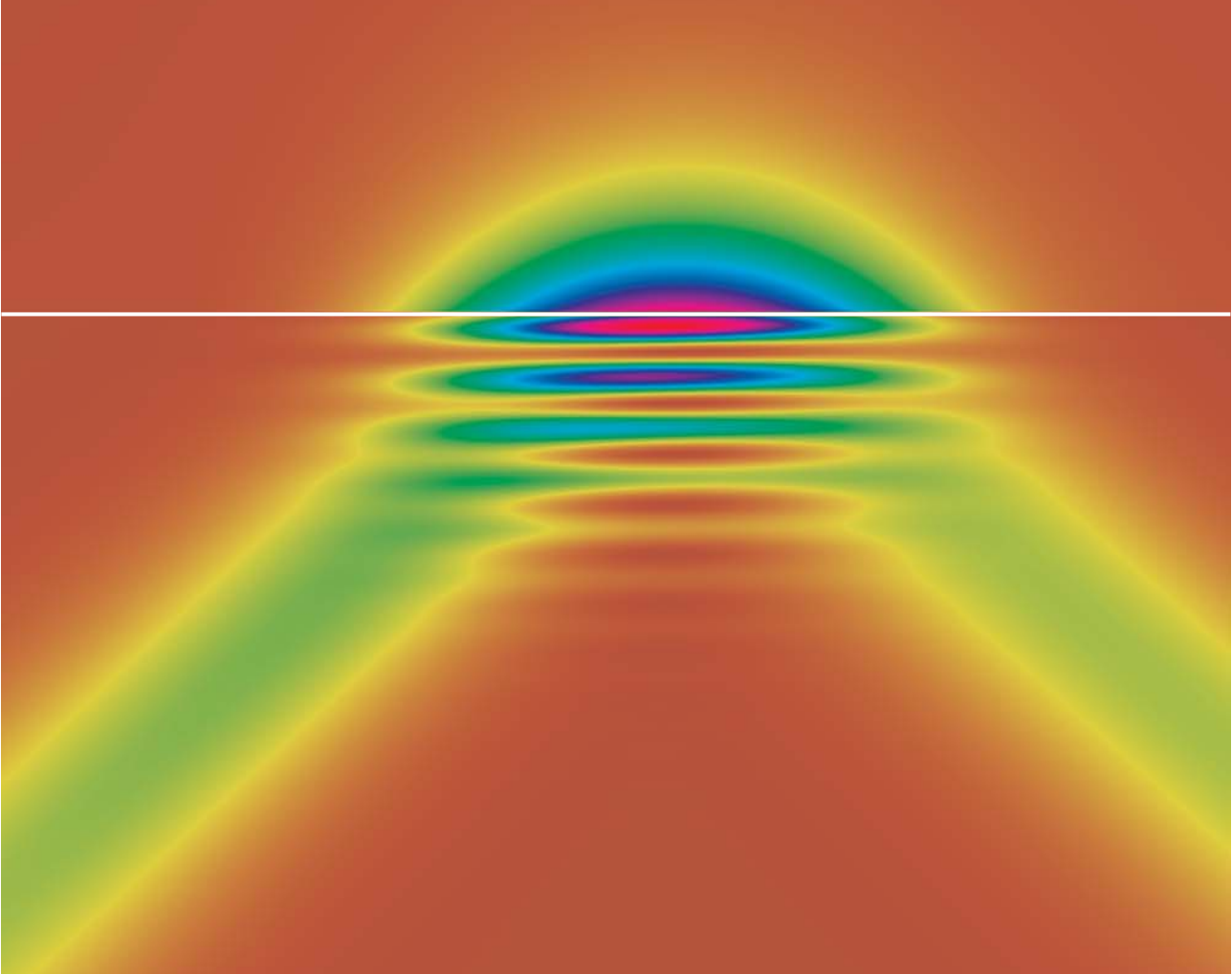# Optical trapping and manipulation of atoms near surfaces

Ronald Cornelussen

Optical trapping

and manipulation

of atoms near surfaces

Optical trapping

and manipulation

of atoms near surfaces

ACADEMISCH PROEFSCHRIFT

ter verkrijging van de graad van doctor
aan de Universiteit van Amsterdam,
op gezag van de Rector Magnificus
prof. mr. P.F. van der Heijden
ten overstaan van een door het college voor promoties ingestelde
commissie, in het openbaar te verdedigen in de Aula der Universiteit
op dinsdag 16 november 2004, te 10:00 uur

door

Ronald Alexander Cornelussen

geboren te Maastricht

Promotiecommissie:

Promotor: prof. dr. H.B. van Linden van den Heuvell
Co-promotor: dr. R.J.C. Spreeuw

Overige leden: prof. dr. W.J. Buma
                     dr. N.J. van Druten
                     prof. dr. H.F. Henrichs
                     prof. dr. K.A.H. van Leeuwen
                     dr. G.H. Wegdam

Faculteit der Natuurwetenschappen, Wiskunde en Informatica

aan mijn ouders

Omslag: Intensiteitsverdeling van een laserbundel bij interne reflectie aan een glas-vacuüm overgang met een hoek van inval groter dan de kritische hoek. Er zijn verschillende effecten te zien. Aan de glaszijde, onder de witte lijn, zijn de inkomende en de gereflecteerde bundel zichtbaar, de invallende bundel is iets intenser dan de gereflecteerde. Door de fasesprong bij de reflectie heeft het *interferentie-patroon* geen maximum of minimum op het oppervlak. Er zijn dispersie-effecten zichtbaar: de bundel is *divergent* met de waist op het oppervlak en het interferentie-patroon is *niet parallel* aan het oppervlak. Verder is de *Goos-Hänchen* shift zichtbaar: de gereflecteerde bundel is verschoven ten opzichte van de speculaire reflectie, d.w.z. het snijpunt van de inkomende en de gereflecteerde bundel ligt boven het glasoppervlak. Aan de vacuümzijde, boven de witte lijn, is de intensiteitsverdeling van het *evanescente veld* weergegeven. Dit deel is vijf keer uitgerekt in verticale richting. Het plaatje is berekend met de vergelijkingen uit paragraaf 2.2. De hoek van inval is $5.7°$ groter dan de kritische hoek en de waist is $1.6~\mu$m, resulterend in een bundeldivergentie van $7°$. Door de extreem kleine bundeldiameter zijn al deze effecten in één plaatje zichtbaar.

Contents

1 General introduction

This thesis exploits the possibilities of optical evanescent fields as tools to manipulate cold atoms. An evanescent wave (EW) appears when a light wave undergoes total internal reflection at the surface of a dielectric. At the vacuum side of this surface an optical field exists that decays exponentially on a length scale comparable to the optical wavelength. There are many applications of EWs in combination with cold atoms. It can be used as a mirror for cold atoms. Scattering evanescent photons can lead to further cooling of the atoms. A combination of more EWs can lead to low-dimensional traps for cold atoms. Finally, they enable us to probe atoms in close proximity to a dielectric surface. Our samples of cold atoms are prepared using conventional laser-cooling techniques. This chapter will briefly review the major developments in the field of cold atoms, focussing in particular on the interaction of cold atoms with evanescent fields.

1.1   Laser cooling

The development of laser-cooling techniques in the 1980s quickly resulted in atomic samples with high phase-space densities and adopted quantum degeneracy as a goal. In particular the development of the magneto-optical trap that was proposed by Dalibard (according to [1]) and realized by Chu and co-workers [2] was a major breakthrough. This system provides an easy way to collect several millions of atoms and cool them to temperatures of less than a milli-Kelvin. Even lower temperatures can be achieved by applying techniques like polarization-gradient cooling. Both techniques are currently employed in hundreds of experiments worldwide. They are used to collect and cool numerous gaseous atomic species to relatively high densities and low temperatures. In 1997 S. Chu, C. Cohen-Tannoudji, and W. Phillips were awarded the Nobel prize *for development of methods to cool and trap atoms with laser light* [1, 3, 4]. The phase-space density that can be achieved by these techniques is ultimately limited by re-absorption of the spontaneously emitted secondary photons.

Far off-resonant dipole potentials created by far-detuned laser beams are very well suited to act as conservative traps for atoms. The scattering rate can be made arbitrarily small when sufficient laser power is available, as will be discussed in chapter 2. Since laser beams can be focussed, and multiple beams can be crossed, it is possible to create traps of almost any geometry. However, trapping atoms in these traps does not result in an increase of the phase-space density.

More advanced laser-cooling techniques, combining dipole traps with dissipative laser cooling, has resulted in a further increase of the phase-space density. In particular low-dimensional geometries are interesting, since these provide a large solid angle for secondary photons to escape, so that the problem of re-absorption is reduced. The highest phase-space densities obtained are for Cs for which a phase-space density of 1/30 has been realized using Raman sideband cooling [5], and for Sr, where a sample of 4×10^4 atoms has been cooled to a phase-space density of 1/10 using Doppler cooling on a narrow, spin-forbidden optical transition, while the atoms were trapped in a far off-resonance dipole trap [6].

1.2   Manipulating atoms using evanescent waves

An EW that is far detuned from an atomic transition such that it becomes a repulsive potential acts as a mirror for atoms. Such a mirror was proposed by Cook and Hill [7]. It was first demonstrated with an atomic beam at grazing incidence by Balykin *et al.* [8] and later with cold atoms at normal incidence by Kasevich *et al.* [9].

An atom can undergo a Raman transition to another internal state when it reflects from an EW mirror. This dissipative process leads to a loss of energy of the atom. Atoms that have made such a transition will bounce inelastically, i.e. to a lower height. This process will also lead to cooling of the sample of atoms, which was first demonstrated by Laryushin *et al.* [10]. This feature is used in the gravito-optical surface trap (GOST) by Ovchinikov *et al.* [11] where multiple inelastic bounces led

to a significant increase of the phase-space density.

The combination of an attractive and a repulsive EW potential can lead to a trapping configuration. This is called a double EW trap (DEWT) and was proposed by Ovchinikov *et al.* [12]. Hammes *et al.* [13] have successfully demonstrated loading a DEWT trap from a GOST trap combined with a "dimple potential", trapping 20 000 Cs atoms at a temperature of 100 nK.

EWs also provide a tool to selectively detect atoms in close proximity to a dielectric surface. This is useful to detect atoms that are trapped close to such a surface. Aspect *et al* [14] have proposed a technique to detect atoms close to a surface in a non-destructive manner by detecting the phase change of a far detuned EW. In chapter 6 we present a novel technique to probe atoms at distances on the order of an optical wavelength from a dielectric surface, by measuring the *absorption* of a resonant EW. The approach is tested using cold atoms that are dropped onto the surface [15]. The possibility to detect atoms at these distances from a dielectric surface gives access to measuring cavity QED effects. An experiment that measures the effect of a nearby surface on the linewidth of the atoms was recently published [16].

1.3   Loading scheme for evanescent-wave traps

The phase-space densities obtained by laser cooling fuelled the hope that Bose-Einstein condensation could be realized using these techniques. The theory of Bose-Einstein statistics [17, 18, 19] predicts that for non-interacting atoms with sufficiently low temperature a large fraction of the atoms accumulate in the lowest energy quantum state. This happens when the de Broglie wavelength λ_{dB} becomes larger than the mean interparticle separation $n^{-1/3}$, or better $n\lambda_{dB}^3 > 2.61$. All these atoms are in the same quantum state and thus form a macroscopically sized quantum system. Such a system is called a Bose-Einstein condensate (BEC). However, this has not been achieved using laser cooling until today.

EWs are common in schemes for further increasing the phase-space density in a fully dissipative optical way. During the reflection of a sample of atoms from an EW mirror the density in the turning point is significantly increased. This density increase can be employed by making use of the highly localized scattering properties of EWs. A Raman transfer, induced by scattering an evanescent photon, to an internal state that no longer interacts with the repelling evanescent field, but does interact with a tightly confining trapping potential will lead to an increase of the phase-space density [20]. The low dimensionality automatically deals with the problem of the re-absorption of the secondary photon.

Gauck *et al.* [21] have demonstrated the proof of principle of this loading scheme using metastable Ar* atoms. Their attempts were restricted by the metastable character of the Ar* atoms, which enables Penning ionization and therefore excludes high densities. For sufficiently high phase-space densities the transfer into a single state of the trap will be enhanced due to the bosonic nature of the atoms [22], which corresponds to the stimulated emission process of a laser. Inouye *et al.* [23] demonstrated this effect in free space using condensed samples.

Chapters 6 and 7 discuss our efforts to implement this method for ^{87}Rb atoms. These atoms are advantageous because they are trapped in the ground state and therefore do not suffer from Penning ionization. On the other hand the energy separation between the bouncing and trapped state is too small to decouple the trapped atoms from the repelling evanescent field. Spreeuw *et al.* [20] discuss a dark-state trap that should by-pass this problem.

In chapter 6 the atoms are trapped in a standing-wave dipole trap after their transfer. Due to the highly localized scattering of an EW all atoms are concentrated in just a few potential minima of this trap. The evanescent probing technique was used to detect the trapped atoms. Chapter 7 discusses the EW dark state trap proposed in [20] in more detail. Several geometries are discussed. Within the range of experimentally realistic parameters, optimum values for these parameters are derived from a numerical analysis of the experiment. The actual implementation of the experiment was prevented by technical problems, which are also discussed.

1.4 Bose-Einstein condensation

In 1995 Bose-Einstein condensation was realized using evaporative cooling of magnetically trapped atoms in Boulder [24], MIT [25], and at Rice university [26, 27]. Laser cooling was only used as the initial step to prepare a sample of atoms that was loaded in a magnetic trap. A subsequent phase of forced evaporation led to an increase of the phase-space density until the quantum degeneracy limit was reached. By outcoupling atoms from a BEC, atom lasers have been realized [28, 29, 30, 31, 32]. However, because the condensate is depleted their output is pulsed. In 2001 E. Cornell, W. Ketterle, and C. Wieman were awarded the Nobel prize *for the achievement of Bose-Einstein condensation in dilute gases of alkali atoms, and for early fundamental studies of the properties of the condensates* [33, 34]. Since the first realization of a BEC, it has been realized for many atomic species, and diatomic molecules [35, 36, 37]. Furthermore several trapping geometries are commonly used nowadays and BEC is for instance achieved for atoms trapped in micro-structured atom chips [38, 39].

Bose-Einstein condensation of atoms trapped in far off-resonance dipole traps has also been realized [40, 41]. The phase-space density density is, however, still increased by means of forced evaporation while the atoms remain trapped in a conservative potential. So far these experiments were only successful for dipole traps created by CO_2 lasers with a wavelength of 10.6 μm. Chapter 3 discusses a possible extension for obtaining BEC in a far off-resonance dipole trap. It investigates the possibility to use an alternative, experimentally more practical wavelength in order to accomplish the same goal.

There are other experiments that aim at or have realised high phase-space densities using EWs. However they all make use of an evaporative cooling stage. Colombe *et al.* [42] are working towards loading a DEWT surface trap from a 3D ^{87}Rb BEC. Rychtarik *et al.* [43] have created a two-dimensional BEC of Cs atoms, by trapping thermal atoms in a GOST, increasing the density using a dimple potential [44], and

a subsequent evaporative cooling stage.

Even though BEC has been realized, it is still interesting to investigate the possibility of realizing a quantum degenerate system in a fully dissipative, optical way. One reason is that this could open routes to reaching quantum degeneracy for atomic species with unfavorable s-wave scattering lengths, for which evaporative cooling can not be applied. Another reason is that it is possible to create quantum degenerate samples in excited vibrational states of the trap. With a thermal process like evaporative cooling, only condensation to the ground state is possible. Finally these systems may lead to cw atom lasers. Even before BEC was realized several schemes to realize this have been proposed, e.g. [22, 45].

1.5   Interferometry

Chapter 8 describes a novel type of interferometer and addresses the question whether spontaneous emission can perform the role of the beam splitter. Atoms that bounce inelastically from an EW mirror have made a transition to another internal state during their reflection, see e.g. [46]. This transition can occur on the ingoing or the outgoing part of the trajectory, and the two possible paths follow a different trajectory through phase space. Since this transition is a spontaneous Raman transition, which is generally considered to be an incoherent process, the question arises whether these paths could give rise to interference. This thesis ends with an unambiguous and surprising answer to this fairly general question by numerically solving the Schrödinger equation.

2 Theory

This chapter provides the theoretical background needed for the rest of this thesis. The first section deals with the description of light in general and evanescent waves in particular. A generalized expression for the intensity of light is derived, that can also be applied to evanescent waves. Subsequently, some equations for dealing with diffraction limited, finite-size beams are presented

The third section focuses on the interaction of atoms with light. Special attention is paid to the description of multi-level atoms and the different conventions used in the literature. The spontaneous light pressure force and the dipole force are introduced. Accurate information of the ^{87}Rb D lines is given. The last section deals briefly with the Van der Waals interaction of atoms in the vicinity of a dielectric surface.

2.1 Propagating and evanescent light

This section focuses on the description of light fields as they occur in our experiment. The main result will be the derivation of some characteristics of evanescent waves. Since an evanescent wave is not a propagating wave and the energy flux perpendicular to the surface is imaginary, we have to modify the usual expression for the intensity. Since many of the equations dealing with the interaction of atoms with light are expressed in terms of the light intensity, they are not straightforwardly applicable to the case of atoms interacting with evanescent waves. In the first parts of this section we will deal with plane waves and an effective intensity is defined that is generally usable for describing the interaction of atoms with electromagnetic waves. Subsequently some basic concepts of evanescent waves are defined and we will introduce the concept of the evanescent-wave intensity. Finally we will focus on some effects specific for circularly-polarized evanescent waves.

2.1.1 Plane waves, definitions and refraction phenomena

We consider a plane monochromatic light wave with an electric-field component $\mathbf{E}(\mathbf{x}, t)$ at position $\mathbf{x}$ and time t. It is described by

$$\mathbf{E}(\mathbf{x}, t) = \Re\left(\widetilde{\mathbf{E}} e^{i(\mathbf{k} \cdot \mathbf{x} - \omega t)}\right), \tag{2.1}$$

with angular frequency ω, wavevector $\mathbf{k}$, and $\widetilde{\mathbf{E}}$ a complex vector describing the amplitude and the polarization of the wave. The symbol $\Re(\cdot)$ denotes the real part of an expression. The frequency ω and the amplitude k of the wavevector $\mathbf{k}$ are proportional $k = (n/c)\omega$. Here c is the velocity of light in vacuum and n the refractive index of the medium in which the wave propagates; the fraction c/n is the velocity of light in this medium. Since we consider monochromatic light we can consider n to be constant. The wavevector $\mathbf{k}$ is parallel to the propagation direction of the wave. The wavelength λ is defined by $\lambda = 2\pi/k$. In vacuum, with $n = 1$, we define the free space wavevector $k_0 = \omega/c$ and the free space wavelength $\lambda_0 = 2\pi/k_0$.

When this plane wave hits a boundary, separating two media with different optical properties, it will be partially reflected and partially transmitted. In this section we consider a plane wave, incident at an angle θ_i with respect to the surface normal, as is shown in Fig. 2.1. This figure also shows the geometry in which we will describe this problem. The surface boundary is in the $\mathcal{O}xy$ plane and the plane of incidence of the wave is in the $\mathcal{O}xz$ plane. The angle of the reflected wave θ_r is equal to θ_i, and the angle of the transmitted wave θ_t is given by Snell's law

$$\frac{\sin \theta_t}{\sin \theta_i} = \frac{n_1}{n_2}. \tag{2.2}$$

The wavevector $\mathbf{k}_i$ of the incident wave in this geometry is given by

$$\mathbf{k}_i = n_1 k_0 \left(\sin \theta_i, 0, \cos \theta_i\right), \tag{2.3}$$
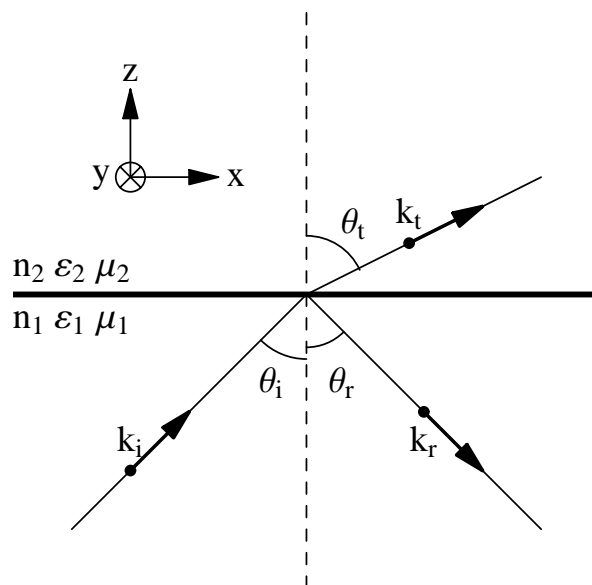
Figure 2.1: Schematic representation of the geometry of a beam reflected and refracted from a surface boundary between two media with refractive indices n_1 and n_2. Since the refracted angle θ_t is larger than the angle of incidence θ_i, $n_1 > n_2$ for this example.

and the electric-field amplitude $\widetilde{\mathbf{E}}_i$ of this wave is now

$$\widetilde{\mathbf{E}}_i = \left(-E_i^{\text{TM}} \cos\theta_i, E_i^{\text{TE}} e^{i\varphi}, E_i^{\text{TM}} \sin\theta_i \right). \tag{2.4}$$

Here E_i^{TM} and E_i^{TE} represent the components of the electric-field vector parallel respectively perpendicular to the plane of incidence $\mathcal{O}xz$. The exponent $\exp(i\varphi)$ describes the phase difference between the TE and TM-polarized components. Similar equations hold for the wavevector of the reflected field $\mathbf{k}_r$ and the transmitted field $\mathbf{k}_t$, and for the reflected electric field $\mathbf{E}_r(\mathbf{x}, t)$ and the transmitted electric field $\mathbf{E}_t(\mathbf{x}, t)$.

For these plane waves the corresponding magnetic field is given by

$$\widetilde{\mathbf{H}} = \sqrt{\frac{\varepsilon}{\mu}} \frac{\mathbf{k}}{k} \times \widetilde{\mathbf{E}}, \tag{2.5}$$

with ε the electric, and μ the magnetic permeability of the medium.

2.1.2   Energy density and energy flow

The time-averaged energy density u of a wave or field that obeys Maxwell's equations is in general defined by

$$u = \frac{1}{4} \left(\widetilde{\mathbf{E}} \cdot \widetilde{\mathbf{D}}^* + \widetilde{\mathbf{B}} \cdot \widetilde{\mathbf{H}}^* \right), \tag{2.6}$$

where we have introduced the electric displacement $\mathbf{D} = \varepsilon\mathbf{E}$ and the magnetic induction $\mathbf{B} = \mu\mathbf{H}$. Here we follow the terminology of Jackson [47]. Unless specified otherwise, we will work in S.I. units throughout this thesis. The first term is called

the time-averaged energy density of the electric field u_E and the second term is the time-averaged energy density of the magnetic field u_H. From Eqs. (2.5) and (2.6) it is obvious that the electric and magnetic-field energy densities are equal for a plane wave. For the specific case of a plane wave, the total time-averaged energy density reduces to

$$u_\mathrm{pw} = \frac{1}{2}\varepsilon|\widetilde{\mathbf{E}}|^2, \tag{2.7}$$

where the subscript "pw" denotes plane wave.

The time-averaged energy flow is in general defined by Poynting's vector $\mathbf{S}$

$$\mathbf{S} = \frac{1}{2}\,\widetilde{\mathbf{E}} \times \widetilde{\mathbf{H}}^*, \tag{2.8}$$

which for a plane wave, by substituting Eq. (2.5), reduces to

$$\mathbf{S}_\mathrm{pw} = \frac{\varepsilon c}{2n}|\widetilde{\mathbf{E}}|^2\frac{\mathbf{k}}{k}. \tag{2.9}$$

The amplitude $|\mathbf{S}_\mathrm{pw}|$ is equal to the intensity I of the wave and it points in the direction of propagation. This intensity I can also be defined from the energy density (2.7)

$$I = u_\mathrm{pw}\frac{c}{n}. \tag{2.10}$$

The main reason why we are interested in the intensity of light is because we want to determine its interaction with atoms, which we will examine in more detail in section 2.3. This interaction is, however, almost completely dominated by the electric-field component of the light. For plane waves the intensity I is a valid parameter to describe this interaction because the energy densities of the electric and magnetic fields are equal under all circumstances. It is commonly used because it is an experimentally convenient quantity. A more generally applicable quantity would be the electric energy density u_E, or the electric-field energy flux density $u_\mathrm{E}c/n$. Based on this we can define an effective intensity I_eff, which is generally valid for describing the interaction of atoms with light

$$I_\mathrm{eff} = \frac{2c}{n}u_\mathrm{E} = \frac{\varepsilon c}{2n}\widetilde{\mathbf{E}} \cdot \widetilde{\mathbf{E}}^*. \tag{2.11}$$

In the remainder of this thesis we will drop the subscript "eff". For virtually all optical materials $\mu = \mu_0$ is satisfied and the pre factor $\varepsilon c/2n$ in Eqs. (2.9) and (2.11) can be replaced by $n\varepsilon_0 c/2$.

2.1.3 Evanescent waves

When a light wave is refracted from a medium with a higher index of refraction n_1 to a medium with a lower index of refraction $n_2 < n_1$, the refracted wave propagates more parallel to the surface. Using Snell's law (2.2) we can determine a critical angle θ_c

$$\theta_\mathrm{i} = \theta_\mathrm{c} = \arcsin\frac{n_2}{n_1}, \tag{2.12}$$

at which the refracted wave propagates parallel to this surface, $\theta_t = \pi/2$. For even larger angles of incidence θ_i, Eq. (2.2) yields a complex value for θ_t, which is associated with the appearance of an evanescent wave. In the remainder of this section and the rest of this thesis we will consider evanescent waves in vacuum, thus $n_2 = 1$, near a dielectric medium with $n_1 = n$. The general result can be obtained by replacing n with n_1/n_2 and k_0 with k_0/n_2.

For this case with $\theta_i > \theta_c$ it is convenient to write the Fresnel equations [48, 49] as follows

$$r_{\mathrm{TE}} = \frac{n\cos\theta_i - i\sqrt{n^2\sin^2\theta_i - 1}}{n\cos\theta_i + i\sqrt{n^2\sin^2\theta_i - 1}}, \tag{2.13}$$

$$r_{\mathrm{TM}} = \frac{\cos\theta_i - in\sqrt{n^2\sin^2\theta_i - 1}}{\cos\theta_i + in\sqrt{n^2\sin^2\theta_i - 1}}, \tag{2.14}$$

$$t_{\mathrm{TE}} = \frac{2n\cos\theta_i}{n\cos\theta_i + i\sqrt{n^2\sin^2\theta_i - 1}}, \tag{2.15}$$

$$t_{\mathrm{TM}} = \frac{2n\cos\theta_i}{\cos\theta_i + in\sqrt{n^2\sin^2\theta_i - 1}}. \tag{2.16}$$

These Fresnel equations give us the reflected amplitudes $E_r^{\mathrm{TE}} = r_{\mathrm{TE}} E_i^{\mathrm{TE}}$ and $E_r^{\mathrm{TM}} = r_{\mathrm{TM}} E_i^{\mathrm{TM}}$, and refracted amplitudes $E_t^{\mathrm{TE}} = t_{\mathrm{TE}} E_i^{\mathrm{TE}}$ and $E_t^{\mathrm{TM}} = t_{\mathrm{TM}} E_i^{\mathrm{TM}}$ of the TE and TM-polarized electric-field components, directly at the surface. They show that $|r_{\mathrm{TE}}| = |r_{\mathrm{TM}}| = 1$ for $\theta_i \geq \theta_c$, which is called total internal reflection. The field on the transmission side is called an evanescent wave. Although this is not a plane wave, we can derive some properties by substituting the complex value of θ_t in the plane wave results of sections 2.1.1 and 2.1.2.

For example the wavevector $\mathbf{k}_t$ can be written similar to Eq. (2.3) with θ_i replaced by θ_t. By rewriting the $\sin\theta_t$ and $\cos\theta_t$ terms with use of Eq. (2.2) this results in

$$\mathbf{k}_t = k_0\left(n\sin\theta_i, 0, \pm i\sqrt{n^2\sin^2\theta_i - 1}\right), \tag{2.17}$$

from which is obvious that the component perpendicular to the surface has become imaginary. The field

$$\mathbf{E}_t(\mathbf{x}, t) = \mathcal{R}\left(\widetilde{\mathbf{E}}_t e^{i(\mathbf{k}_t \cdot \mathbf{x} - \omega t)}\right) = \mathcal{R}\left(\widetilde{\mathbf{E}}_t e^{-\kappa z} e^{ik_0 n \sin\theta_i x} e^{-i\omega t}\right), \tag{2.18}$$

with $\kappa = k_0\sqrt{n^2\sin^2\theta_i - 1}$, represents a non-homogeneous wave propagating along the boundary and whose amplitude varies exponentially in the direction perpendicular to the boundary. It is obvious that in this case the plus sign needs to be used in Eq. (2.17) otherwise Eq. (2.18) would diverge for $z \to \infty$. The decay length ξ of this evanescent wave is given by

$$\xi = \frac{1}{\kappa} = \frac{\lambda_0}{2\pi} \frac{1}{\sqrt{n^2\sin^2\theta_i - 1}}. \tag{2.19}$$

This decay length is typically on the order of λ_0.

2.1.4 Effective evanescent-wave intensity

By substitution of the complex value of θ_t, the electric and magnetic-field vectors $\mathbf{E}_t(\mathbf{x}, t)$ and $\mathbf{H}_t(\mathbf{x}, t)$ become

$$\widetilde{\mathbf{E}}_t = \left(-iE_t^{\mathrm{TM}}\sqrt{n^2\sin^2\theta_i - 1}, E_t^{\mathrm{TE}}e^{i\varphi}, E_t^{\mathrm{TM}}n\sin\theta_i \right), \tag{2.20}$$

$$\widetilde{\mathbf{H}}_t = \frac{\varepsilon c}{n} \left(-iE_t^{\mathrm{TE}}\sqrt{n^2\sin^2\theta_i - 1}\,e^{i\varphi}, -E_t^{\mathrm{TM}}, E_t^{\mathrm{TE}}n\sin\theta_i e^{i\varphi} \right), \tag{2.21}$$

where $\mathbf{H}_t$ is defined analogous to $\mathbf{E}_t$ in Eq. (2.18). The fields $\mathbf{E}_t(\mathbf{x}, t)$ and $\mathbf{H}_t(\mathbf{x}, t)$ are still orthogonal as in the plane wave case, and they are both orthogonal to $\mathbf{k}_t$ and the total energy density u is still independent of the polarization. However, the electric and magnetic energy densities u_{E} and u_{H} are no longer equal, and their ratio depends on the polarization. Since the z component of the energy flow $\mathbf{S}$ becomes imaginary [47, 48] it is not possible to define an intensity for this evanescent wave in the usual way. However, in order to describe the interaction with atoms, an effective intensity based on Eq. (2.11) can still be defined.

We now introduce transmissivity coefficients T^{TE} and T^{TM} for the effective evanescent-wave intensities for the TE and TM-polarized components as

$$T_{\mathrm{EW}}^{\mathrm{TM}} = \frac{I_t^{\mathrm{TM}}}{I_i^{\mathrm{TM}}} = \frac{1}{n}\frac{|E_t^{\mathrm{TM}}|^2}{|E_i^{\mathrm{TM}}|^2} = \frac{1}{n}(2n^2\sin^2\theta_i - 1)t_{\mathrm{TM}}t_{\mathrm{TM}}^*, \tag{2.22}$$

$$T_{\mathrm{EW}}^{\mathrm{TE}} = \frac{I_t^{\mathrm{TE}}}{I_i^{\mathrm{TE}}} = \frac{1}{n}\frac{|E_r^{\mathrm{TM}}|^2}{|E_i^{\mathrm{TM}}|^2} = \frac{1}{n}t_{\mathrm{TE}}t_{\mathrm{TE}}^*, \tag{2.23}$$

where in the last step Eq. (2.20) and the substitutions for E_t^{TM} and E_t^{TE} have been used. The transmissivities have been explicitly evaluated. By substituting Eqs. (2.15) and (2.16) in Eqs. (2.22) and (2.23), these transmissivities become

$$T_{\mathrm{EW}}^{\mathrm{TM}} = \frac{4n\cos^2\theta_i(2n^2\sin^2\theta_i - 1)}{\cos^2\theta_i + n^2(n^2\sin^2\theta_i - 1)}, \tag{2.24}$$

$$T_{\mathrm{EW}}^{\mathrm{TE}} = \frac{4n\cos^2\theta_i}{n^2 - 1}. \tag{2.25}$$

2.1.5 Elliptically and circularly-polarized evanescent waves

From Eqs. (2.20) and (2.21) it is clear that a TM-polarized incident wave leads to an "elliptically-polarized" and a TE-polarized incident wave to a "linearly-polarized" electric field at the vacuum side of the surface. In the latter case, however, the magnetic field has a similar "elliptical polarization" as the electric field in the first case. The fact that the "polarizations" of the electric and magnetic fields are different is another striking difference between the evanescent and the more common propagating light fields. The aspect ratio of this elliptical polarization depends on the angle of incidence of the incident wave. In the limit of θ_i approaching the critical angle θ_c, the polarization tends to linear.
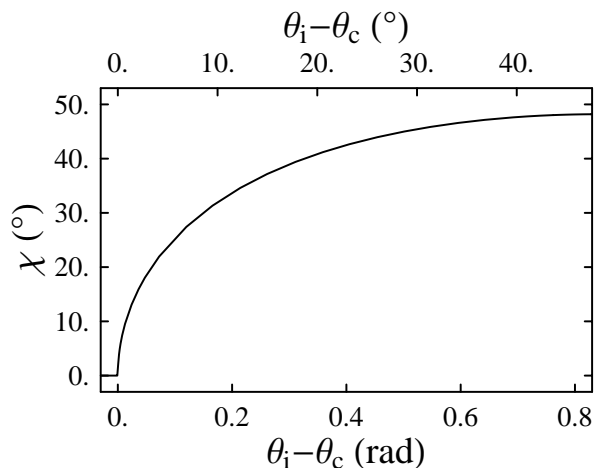
Figure 2.2: The tilt angle χ of the plane of circular polarization versus the angle of incidence θ_i for a medium with $n = 1.5$.

With $\varphi = \pm\pi/2$ and $E_t^{\mathrm{TE}} = E_t^{\mathrm{TM}}$, Eq. (2.20) represents a circularly-polarized evanescent wave. The plane of polarization is however not perpendicular to the real part of the $\mathbf{k}$ vector $\mathcal{R}(\mathbf{k})$ as in the case of a propagating wave. Instead it makes an angle in the $\mathcal{O}xy$ plane with $\mathcal{R}(\mathbf{k})$ of $\chi = \arctan(\sqrt{n^2 \sin^2 \theta_i - 1})$. This angle is equal to the angle between the Poynting vector and $\mathcal{R}(\mathbf{k})$. Fig. 2.2 shows this angle χ as a function of the angle of incidence θ_i for a medium with $n = 1.5$. For $\theta_i = \theta_c + 20$ mrad this tilt angle is $12°$ and it increases up to $48°$ when θ_i approaches $\pi/2$.

2.2 Description of diffraction limited beams

The description of light beams presented in the previous section is valid for plane waves. Many features of a physically realistic beam with a finite beam diameter can be properly described by a plane wave. However, this is not sufficient e.g. in the case of total internal reflection, for angles of incidence very close to the critical angle. This is important for the analysis of experiments where atoms are probed using evanescent fields, that is presented in chapter 6. In the first part of this section is derived how a diffraction limited beam can be treated as a coherent superposition of plane waves. The second part of this section describes how the reflected and transmitted fields can be calculated. Also a method to determine the effective EW intensity is presented.

2.2.1 Propagating beam equations

A plane wave propagating in the xz plane at an angle θ with the z axis is described by $\exp(ik_x(\theta)x)\exp(ik_z(\theta)z)$, as is obvious from Eq. (2.1), with $k_x(\theta) = nk_0 \sin\theta$ and $k_z(\theta) = nk_0 \cos\theta$. Here n is the index of refraction of the medium. A Gaussian beam can be described as a coherent sum over several propagation directions θ.

These are normally distributed around a central value θ_0 and the distribution has a $1/e$ width of ϕ. From the theory of Gaussian beams [49, 50], we know that the far field divergence of a beam is equal to $\lambda_0/\pi n w_0$, with λ_0 the wavelength of the light and w_0 the waist (minimum $1/e$ radius of the electric field distribution) of the beam. This divergence is equal to the angular spread ϕ

$$\phi = \frac{\lambda_0}{\pi n w_0}. \tag{2.26}$$

The electric field distribution of a propagating beam is now given by

$$E(x, z) = \frac{1}{\pi\phi} \int_0^{2\pi} e^{ik_x(\theta)x} e^{ik_z(\theta)z} e^{inkd(\theta-\theta_0)^2/2} e^{-(\theta-\theta_0)^2/\phi^2} \mathrm{d}\theta, \tag{2.27}$$

where the factor $\exp(inkd\,(\theta - \theta_0)^2\,/2)$ displaces the waist by a distance d along the propagation direction of the beam. The integral is normalized such that $|E|^2 = 1$ in the waist of the incident beam. Eq. (2.27) is completely similar to the more common notation in the literature where the integration is over the wavevector [50], instead of over the angle of the wavevector with an interface.

2.2.2 Reflection and transmission

The reflection of a propagating wave given by Eq. (2.27) from a boundary at $z = 0$ between a medium with index of refraction $n_1 = n$ and a medium with index of refraction $n_2 = 1$, as depicted in Fig. 2.1, is described by

$$E_{\mathrm{r}}(x, z) = \frac{1}{\pi\phi} \int_{-\pi/2}^{\pi/2} r(\theta) e^{ik_x(\theta)} e^{-ik_z(\theta)z} e^{ink_0 d(\theta-\theta_0)^2/2} e^{-(\theta-\theta_0)^2/\phi^2} \mathrm{d}\theta, \tag{2.28}$$

where $r(\theta)$ is a Fresnel reflection coefficient $r_{\mathrm{TE}}(\theta)$ or $r_{\mathrm{TM}}(\theta)$, as defined by Eqs. (2.13) and (2.14), depending on the polarization of the light. Obviously only the vector k_z has changed sign with respect to Eq. (2.27). We have restricted the angle of incidence θ_0 here to $-\pi/2 < \theta_0 < \pi/2$.

The propagating part of the wave that is transmitted through this boundary is described by

$$E_{\mathrm{t}}(x, z) = \frac{1}{\pi\phi} \int_{-\pi/2}^{\theta_{\mathrm{c}}} t(\theta) e^{ik_x'(\theta)x} e^{ik_z'(\theta)z} e^{ink_0 d(\theta-\theta_0)^2/2} e^{-(\theta-\theta_0)^2/\phi^2} \mathrm{d}\theta, \tag{2.29}$$

where $t(\theta)$ is a Fresnel transmission coefficients $t_{\mathrm{TE}}(\theta)$ or $t_{\mathrm{TM}}(\theta)$, as defined by Eqs. (2.15) and (2.16), depending on the polarization of the light. The wavevectors k_x' and k_z' are defined by $k_x' = nk_0 \sin\theta$ and $k_z' = k_0\sqrt{1 - n^2\sin^2\theta}$. The evanescent part of the transmitted field is described by

$$E_{\mathrm{EW}}(x, z) = \frac{1}{\pi\phi} \int_{\theta_{\mathrm{c}}}^{\pi/2} t(\theta) e^{ik_x'(\theta)x} e^{-z/\xi(\theta)} e^{ink_0 d(\theta-\theta_0)^2/2} e^{-(\theta-\theta_0)^2/\phi^2} \mathrm{d}\theta, \tag{2.30}$$

where the decay length $\xi(\theta)$ is defined by Eq. (2.19).

In order to calculate the effective intensity of the evanescent field one needs to take care of the extra pre factors of Eqs. (2.22) and (2.23). This is done by replacing the Fresnel transmission coefficient $t(\theta)$ by the square root of the corresponding evanescent-wave transmissivity $\sqrt{T_{\text{EW}}(\theta)}$, as defined by Eqs. (2.24) and (2.25). The absolute value of the square of the resulting integral scales with the intensity. Due to the special normalization of Eq. (2.27), the EW intensity distribution is now given by

$$I_{\text{EW}}(x,z) = I_{\text{i}} \left| \frac{1}{\pi\phi} \int_{\theta_{\text{c}}}^{\pi/2} \sqrt{T_{\text{EW}}(\theta)} e^{ik_x(\theta)x} e^{-z/\xi(\theta)} e^{ink_0 d(\theta-\theta_0)^2/2} e^{-(\theta-\theta_0)^2/\phi^2} \mathrm{d}\theta \right|^2 ,$$

(2.31)

with I_{i} the maximum intensity of the incident beam at the boundary.

2.3 Atoms and their interaction with light

In this section we describe the interaction of atoms with monochromatic light. We will focus mainly on mechanical effects on the atom. In the first part we will describe the hypothetical situation of a two-level atom to demonstrate the two different forces acting on an atom. In the second part we will extend this to multi-level atoms and finally we will apply it to the case of ^{87}Rb atoms.

2.3.1 Two-level atoms

For a two-level atom with a resonance frequency ω_0 we denote the ground state by $|g\rangle$ and the excited state by $|e\rangle$. The excited state has a lifetime $\tau = 1/\Gamma$, where Γ is the the decay rate or the linewidth of the transition.

When this atom interacts with a light field with frequency ω and intensity I, two physically different contributions of the force acting on the atoms can be distinguished. A force associated with the scattering (absorption and spontaneous emission) of photons, and a force associated with the interaction of the electric field of the light with the electric dipole that is induced in the atom. A beautiful derivation of these two forces is shown in [51] section V.C.2. In the following discussion we will, however, follow a more intuitive approach.

Near resonance effects I - spontaneous light pressure force This effect is particularly important for relatively small detunings, $\delta = \omega - \omega_0$. The process of absorption of a photon from the light field and spontaneously emitting it in another mode is then the dominant process.

The atom receives a momentum kick of $\hbar\mathbf{k}$ for every absorbed photon. A subsequent stimulated emission process results in a momentum change $-\hbar\mathbf{k}_{\text{out}}$. Due to the random character of a spontaneous emission process, the momentum change due to this process averages out over many absorption-emission cycles and only results in heating. This yields a net momentum change of $\hbar\mathbf{k}$ per cycle. The average force

encountered by the atom, which is called the *spontaneous light pressure force*, is thus

$$\mathbf{F}_{\mathrm{sp}} = \hbar\mathbf{k}\Gamma', \tag{2.32}$$

with Γ' the scattering rate, which is the product of the excited state population and the decay rate Γ. For a constant intensity the scattering rate tends to a steady state value

$$\Gamma' = \frac{\Gamma}{2}\frac{s}{s+1}, \tag{2.33}$$

here s is the so called saturation parameter

$$s = \frac{1}{1 + \left(\frac{2\delta}{\Gamma}\right)^2}\frac{I}{I_0}, \tag{2.34}$$

with

$$I_0 = \hbar\Gamma\omega^3/12\pi c^2 \tag{2.35}$$

the saturation intensity of the transition.

Near resonance effects II - Doppler cooling   For a moving atom the effective detuning of the light beams depends on the velocity $\mathbf{v}$ of the atoms due to the Doppler shift $\delta_D = -\mathbf{k} \cdot \mathbf{v}$. For two counterpropagating laser beams, with wavevectors $\pm\mathbf{k}$ and equal detuning δ, the interaction of a moving atom with the beams is different due to the difference in Doppler shift. Naturally the direction of the radiation pressure is in opposite directions. The net force acting on the atom is now

$$\mathbf{F}_{\mathrm{D}} = (\mathbf{F}_{\mathrm{sp}})_{\delta\to\delta-\mathbf{k}\cdot\mathbf{v}} - (\mathbf{F}_{\mathrm{sp}})_{\delta\to\delta+\mathbf{k}\cdot\mathbf{v}}, \tag{2.36}$$

with $\mathbf{F}_{\mathrm{sp}}$ defined by Eq. (2.32)-(2.35). The subscripts $\delta \to \delta \pm \mathbf{k} \cdot \mathbf{v}$ denote that the Doppler shift needs to be incorporated in the detuning in Eq. (2.34). For small saturation, such that $\Gamma' \approx s\Gamma/2$ and $|\mathbf{v}| \ll |\delta|/k_0$ this force is approximated, to second order in $|\mathbf{v}|$, by

$$\mathbf{F}_{\mathrm{D}} = 8\hbar k_0^2 \frac{I}{I_0}\frac{\delta}{\Gamma}\frac{\mathbf{v}}{\left(1 + \left(\frac{2\delta}{\Gamma}\right)^2\right)^2} \approx -\beta\mathbf{v}. \tag{2.37}$$

For small red detunings $\delta \approx -\Gamma/2$ and small atomic velocities $|\mathbf{v}|$ this force is a substantial damping force resulting in cooling of the atom, which is called *Doppler cooling*. The lower bound of the temperature is determined by the random nature of the spontaneous emission process. This lowest reachable temperature is the Doppler temperature $T_{\mathrm{D}} = \hbar\Gamma/2k_{\mathrm{B}}$, with k_{B} Boltzmann's constant.

Far off-resonance effects - dipole force   For large detunings $|\delta| \gg \Gamma$, the off-resonant driving of the atom induces a dipole $\mathbf{d} = \alpha\mathbf{E}$ in the atom, with α the polarizability of the atom. When $|\delta| \gg \Omega_{\mathrm{R}}$, with $\Omega_{\mathrm{R}} = \mathbf{d} \cdot \widetilde{\mathbf{E}}/\hbar$ the Rabi frequency, and $\hbar$ Plank's constant, the spontaneous light pressure force is no longer

the dominant force that acts on the atom. The time-averaged potential energy of the induced dipole $\mathbf{d}$ in the applied field $\mathbf{E}$ is called the *light shift* and is given by

$$U_{\text{dip}} = -\frac{1}{2}\langle \mathbf{d} \cdot \widetilde{\mathbf{E}} \rangle = -\frac{1}{4}\alpha|\widetilde{\mathbf{E}}|^2 \approx \frac{\hbar s\delta}{2}, \tag{2.38}$$

where $\langle \cdot \rangle$ denotes taking the time average over an optical period, and $\widetilde{\mathbf{E}}$ is the electric field as defined in Eq. (2.1). When the transition is driven above (below) the resonance frequency ω, the polarizability α is negative (positive), and thus the resulting potential is repulsive (attractive). Such a light field with $\delta > 0$ ($\delta < 0$) is called blue detuned (red detuned). The *dipole force* acting on the atom is now given by $\mathbf{F}_{\text{dip}} = -\nabla U_{\text{dip}}$. The scattering rate in the limit of large detunings and low saturation is given by

$$\Gamma' = \frac{s\Gamma}{2}. \tag{2.39}$$

From the ratio of the scattering rate Γ' and the light shift U_{dip}

$$\frac{\hbar\Gamma'}{U_{\text{dip}}} = \frac{\Gamma}{\delta}, \tag{2.40}$$

it is clear that for a large detuning δ and a sufficiently large intensity, so that the light shift U_{dip} remains constant, the scattering rate becomes negligibly small, and the potential U_{dip} becomes conservative.

2.3.2 Multi-level atoms

The results of the previous section are generalized to the case of realistic multi-level atoms. First, the formalism which is used to describe these atoms and the transitions between different levels is explained. Subsequently, the results for small detunings are briefly described. The effects for large detunings will be treated somewhat more extensively because of their importance for the remainder of this thesis.

Formalism In realistic, multi-level atoms, transitions between different states have different probabilities or transition strengths. The transition strength of the transition between the initial state $|Fm_{\text{g}}\rangle$ and the final state $|F'm'_{\text{e}}\rangle$ is described by its dipole matrix element $\langle F'm'|\widehat{\mathbf{D}}|Fm\rangle$, with $\widehat{\mathbf{D}} = e\widehat{\mathbf{x}}$ the dipole operator. F and F' are the total angular momentum quantum numbers of this initial and final state respectively, and m and m' are the magnetic quantum numbers of the initial and final magnetic sub-states respectively. Using the Wigner-Eckart theorem [52, 53, 54], this element can be written as

$$\langle F'm'|\widehat{\mathbf{D}}|Fm\rangle = \langle F'\|\widehat{\mathbf{D}}\|F\rangle\langle Fm1q|F'm'\rangle, \tag{2.41}$$

where the first factor is the reduced dipole matrix element, which is independent of the level sub-structure and of the polarization of the light, and the second factor is a Clebsch-Gordan coefficient, which describes the coupling between the magnetic sub-levels for a particular polarization of the light.

It will turn out to be convenient to project the polarization $\boldsymbol{\epsilon} = \widetilde{\mathbf{E}}/|\widetilde{\mathbf{E}}|$ of the light on a coordinate system of spherical polarizations $\boldsymbol{\epsilon}_q$ with $q = -1, 0, +1$ denoting σ^-, π and σ^+-polarized light respectively, all with respect to a chosen quantization axis. The subscript q is the same that appears in the Clebsch-Gordan coefficient of Eq. (2.41).

We have to be aware of the fact that many textbooks on quantum theory of angular momentum [52, 53, 54] use an alternative definition of the reduced dipole matrix which is $\sqrt{2F'+1}$ times larger. One can distinguish between the two definitions by examining the notation of the Wigner-Eckart theorem. To reduce confusion, throughout this thesis we will denote this alternative definition with parentheses $(\cdot\|\cdot\|\cdot)$ instead of angular brackets $\langle\cdot\|\cdot\|\cdot\rangle$. This alternative definition is sometimes convenient since it satisfies $(F'\|\widehat{\mathbf{D}}\|F) = (F\|\widehat{\mathbf{D}}\|F')$ and it will therefore be used in the next chapter. Moreover the notation in most textbooks is chosen such that it most straightforwardly describes emission processes, which is convenient for spectroscopic purposes.

The reduced dipole matrix element can be further simplified by applying the expression [52, 53, 54]

$$\langle F'\|\widehat{\mathbf{D}}\|F\rangle = d_{FF'}\langle J'\|\widehat{\mathbf{D}}\|J\rangle, \tag{2.42}$$

where J and J' are total electronic angular momentum quantum numbers, and

$$d_{FF'} = (-1)^{F+J'+I+1}\sqrt{(2J'+1)(2F+1)} \left\{ \begin{array}{ccc} F & F' & 1 \\ J' & J & I \end{array} \right\}_{6j}. \tag{2.43}$$

Here $\{\stackrel{...}{...}\}_{6j}$ denotes the Racah 6j symbol, and I is the nuclear spin. The reduced dipole matrix for J can, analogously, be further simplified by applying

$$\langle J'\|\widehat{\mathbf{D}}\|J\rangle = d_{JJ'}\langle L'\|\widehat{\mathbf{D}}\|L\rangle, \tag{2.44}$$

where L and L' are orbital angular momentum quantum numbers, and

$$d_{JJ'} = (-1)^{J+L'+S+1}\sqrt{(2L'+1)(2J+1)} \left\{ \begin{array}{ccc} J & J' & 1 \\ L' & L & S \end{array} \right\}_{6j}, \tag{2.45}$$

with S the intrinsic electronic spin quantum number.

Special case - alkali atoms For the D_1 and D_2 lines of alkali atoms we will use subscripts g and e for the ground-state and excited-state properties, respectively. The factor $|d_{J_g J_e}| = 1$, since $L_g = 0$, $L_e = 1$, and $S = \frac{1}{2}$. For the transition from the $F_g = F_{g,max} = L_g + S + I = \frac{1}{2} + I$ ground-state hyperfine level to the $F_e = F_{e,max} = L_e + S + I = \frac{3}{2} + I$ excited state hyperfine level of the D_2 line, the value for $|d_{F_g F_e}| = 1$, for every integer and half-integer value of I. Furthermore, for every integer and half-integer value of F_g, the Clebsch-Gordan coefficient $\langle F_g, \pm m_g, 1, q = \pm 1|F_e = F_g + 1, m_e = \pm(m_g + 1)\rangle = 1$. By combining the above information with Eqs. (2.41)-(2.45) we can deduce

$$|\langle F_{e,max}, m_{F_e} = \pm F_{e,max}|\widehat{\mathbf{D}}|F_{g,max}, m_{F_g} = \pm F_{g,max}\rangle| = |\langle L_e = 1\|\widehat{\mathbf{D}}\|L_g = 0\rangle|.$$

Since this is a closed transition the value of this matrix element equals the value of the dipole moment D of a two-level transition

$$D = |\langle F_{e,max}, m_e = \pm F_{e,max} | \widehat{\mathbf{D}} | F_{g,max}, m_g = \pm F_{g,max} \rangle| = \sqrt{\frac{3\pi\varepsilon_0 c^3 \hbar \Gamma}{\omega_0^3}}. \qquad (2.46)$$

Using Eq. (2.46), Eqs. (2.41)-(2.45) can be simplified to

$$\langle F_g m_{F_g} | \widehat{\mathbf{D}} | F_e m_{F_e} \rangle = \langle F_e m_{F_e} | \widehat{\mathbf{D}} | F_g m_{F_g} \rangle = D d_{F_g F_e} \langle F_g m_g 1 q | F_e m_e \rangle. \qquad (2.47)$$

This expression is valid for all transitions of the alkali D lines.

Near resonance effects   Near-resonant phenomena like laser cooling in multi-level atoms results in effects like polarization-gradient cooling and velocity selective coherent population trapping (VSCPT). For a description of these effects we refer to [55]. The Doppler temperature T_D is no longer the lower bound for the obtainable temperatures. The new lower boundary for polarization-gradient cooling is the recoil temperature T_r which is the temperature associated with the kinetic energy due to the recoil of one photon, while with VSCPT even lower temperatures can be reached. In practice atomic density induced effects like photon re-absorption will also limit the achievable temperatures.

Far off-resonance effects   In order to calculate the light shift of a certain level $|Fm\rangle$, the contributions of the coupling to the various intermediate states $|F'm'\rangle$ to the polarizability must be taken into account. Furthermore due to the substructure of the state F, the polarizability α, introduced as a scalar for two-level atoms, has to be described by a tensor $\boldsymbol{\alpha}$. Its indices are the initial and final magnetic substates m and m'' and the polarizations q and q' of the absorbed and emitted photons, necessary to make the Raman transition.

In the case of low saturation and large detuning from resonance $|\delta_{FF'}| \gg \Gamma$, so that spontaneous emission processes can be neglected, we can derive an expression for the polarizability tensor, using time dependent perturbation theory

$$\boldsymbol{\alpha} = \sum_{F',m'} \frac{\langle Fm'' | \widehat{\mathbf{D}} | F'm' \rangle \langle F'm' | \widehat{\mathbf{D}} | Fm \rangle}{\hbar \delta_{FF'}}, \qquad (2.48)$$

where $\delta_{FF'}$ denotes the detuning of the light with respect to the transition frequency $\omega_{FF'}$ between the initial state $|F\rangle$ and the intermediate state $|F'\rangle$. We have assumed $\delta_{FF'} \ll \omega_{FF'}$, so that the rotating wave approximation can be applied. The light shift operator $\mathbf{U}_{dip}$ is written analogously to Eq. (2.38) as

$$\mathbf{U}_{dip} = -\frac{1}{2} \langle \mathbf{E}^* \cdot \boldsymbol{\alpha} \cdot \mathbf{E} \rangle = -\frac{1}{4} \widetilde{\mathbf{E}}^* \cdot \boldsymbol{\alpha} \cdot \widetilde{\mathbf{E}}, \qquad (2.49)$$

where the contractions are over the polarization states of the photons, and $\langle \cdot \rangle$ again denotes averaging over an optical period. $\mathbf{U}_{dip}$ is a tensor whose indices are the

initial and final magnetic substates m and m''. Its eigenvalues are the light shifts of the various magnetic sub-levels of state F.

When the frequency of the applied optical field is much closer to the D lines than to other transitions in the spectrum, only the coupling to the D lines needs to be considered. This significantly simplifies the calculation. Combining Eqs. (2.49) and (2.48), while substituting Eq. (2.47) yields

$$\mathbf{U}_{F_g} = \frac{\hbar\Gamma^2}{8} \frac{I}{I_0} \sum_{F_e, m_e} \frac{d_{F_g F_e}^2}{\delta_{F_g F_e}} \left(\boldsymbol{\epsilon}^\dagger \cdot \langle F_g m_g'' 1 q' | F_e m_e \rangle \langle F_g m_g 1 q | F_e m_e \rangle \cdot \boldsymbol{\epsilon} \right), \qquad (2.50)$$

where the intensity I, the saturation intensity I_0, and the dipole D are used, as defined in Eqs. (2.9), (2.35), and (2.47) respectively. Again the notation $\boldsymbol{\epsilon} = \widetilde{\mathbf{E}}/|\widetilde{\mathbf{E}}|$ is used for the polarization of light.

2.3.3 Rubidium

The element Rb has two naturally occurring isotopes. The ^{85}Rb isotope is a stable isotope with a natural abundance of 72.17% [56]. The ^{87}Rb isotope has a nuclear lifetime of 4.88×10^{10} yr [56], making it a stable isotope for all our purposes. It has a natural abundance of 27.83(2)% [56]. For atomic physics experiments aiming at quantum degeneracy ^{87}Rb is the favorite isotope due to its favorable collisional properties.

All experiments described in this thesis are performed with ^{87}Rb atoms. The useful transitions are the D_1 line around $\lambda_0 = 795.0$ nm and the D_2 line around $\lambda_0 = 780.2$ nm. The energy levels, including the hyperfine splittings of these transitions, are shown in Fig. 2.3. Fig. 2.4 shows the relative transition strengths $d_{F_g F_e}^2 \langle F_g m_g 1 q | F_e m_e \rangle^2$ between all the magnetic sub-levels of the D_1 and the D_2 lines. According to Eq. (2.46), the transition dipole moment D in Eq. (2.47) is $D = 2.534(3) \times 10^{-29}$ Cm.

In Table 2.1 some general information of Rb is presented. In many instances the closed $|2, \pm 2\rangle \rightarrow |3, \pm 3\rangle$ transition of the D_2 line can be considered as an effective two-level system. Some parameters associated with laser cooling are also given for this transition. An extensive overview of Rb parameters is presented by Steck [57].

2.4 Van der Waals interaction

The experiments described in this thesis will all involve atoms in close proximity of a dielectric surface. At these small distances the Van der Waals potential has to be taken into account. The Van der Waals potential for an atom in vacuum at a distance z from a flat medium with index of refraction n is given by

$$U_{\text{vdW}} = -\frac{n^2 - 1}{n^2 + 1} \frac{1}{48\pi\varepsilon_0} \frac{\mathcal{D}^2}{z^3}, \qquad (2.51)$$

which is derived in [58], Eq. (37). The factor $\mathcal{D}^2$ is the variance of the atomic electric dipole in the atomic state under consideration. Eq. (2.51) is only valid if

this state has no quadrupolar component. An expression for $\mathcal{D}^2$ is derived in [58] section III.A.3. By using this expression the quantum mechanical expression Eq. (2.51) approaches the common expression for the Van der Waals potential, which is given by

$$U_{\text{vdW}} = -\frac{3}{16}\frac{n^2-1}{n^2+1}\left(\frac{1}{k_0 z}\right)^3 \hbar\Gamma, \tag{2.52}$$

to approximately 10%. For k_0 and Γ the values of the dominant D_2 transition of Rb atoms should be used. The experiments in [59, 60] show that this is a good approximation.

general information on ^{87}Rb				
mass	m	[56]	86.90918	u
"			1.443 $\times 10^{-25}$	kg
natural abundance		[56]	27.83(2)	%
nuclear spin	I		3/2	
general parameters D_1 line $\quad 5s\,^2S_{1/2} \to 5p\,^2P_{1/2}$				
optical frequency	ω	[61]	377.1 $\times 2\pi$	THz
wavelength in vacuum	λ_0	$2\pi c/\omega$	795.0	nm
natural lifetime	τ	[63]	27.70(4)	ns
natural linewidth	$\Gamma/2\pi$	$1/\tau$	5.746(8)	MHz
saturation intensity	I_0	$\hbar\Gamma\omega^3/12\pi c^2$	14.9	μW/mm^2
$(J_{\text{g}}\|\widehat{\mathbf{D}}\|J_{\text{e}})$		[63]	3.587(3) $\times 10^{-29}$	Cm
general parameters D_2 line $\quad 5s\,^2S_{1/2} \to 5p\,^2P_{3/2}$				
optical frequency	ω	[62]	384.2 $\times 2\pi$	THz
wavelength in vacuum	λ_0	$2\pi c/\omega$	780.2	nm
natural lifetime	τ	[63]	26.24(4)	ns
natural linewidth	$\Gamma/2\pi$	$1/\tau$	6.065(9)	MHz
saturation intensity	I_0	$\hbar\Gamma\omega^3/12\pi c^2$	16.7	μW/mm^2
$(J_{\text{g}}\|\widehat{\mathbf{D}}\|J_{\text{e}})$		[63]	5.068(3) $\times 10^{-29}$	Cm
Dipole moment				
$\quad |2,\pm2\rangle \to |3,\pm3\rangle$	D	$\sqrt{3\pi\varepsilon_0 c^3\hbar\Gamma/\omega_0^3}$	2.534(3) $\times 10^{-29}$	Cm
laser cooling parameters D_2 line				
Doppler temperature	T_{D}	$\hbar\Gamma/2k_{\text{B}}$	146	μK
recoil temperature	T_{r}	$(\hbar k_0)^2/mk_{\text{B}}$	361	nK
recoil velocity	v_{r}	$\hbar k_0/m$	5.88	mm/s

Table 2.1: Some parameters of ^{87}Rb.
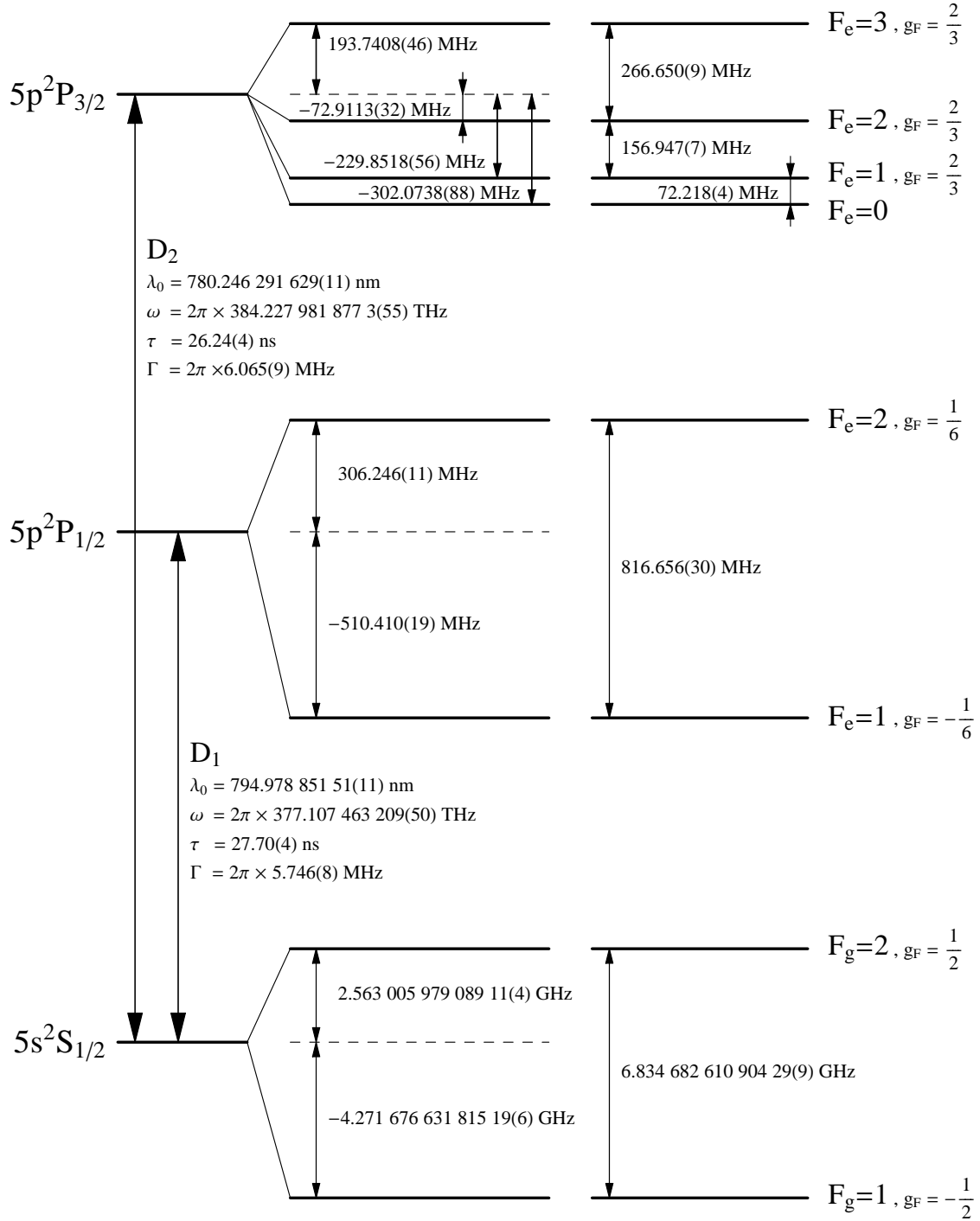
Figure 2.3: The hyperfine levels of the D_1 and D_2 line of ^{87}Rb. Indicated are the splittings between the several (hyper)fine-structure levels. The fine-structure splitting of the D_1 and D_2 lines is from [61] and [62] respectively. The corresponding wavelengths are calculated from these values using $\lambda_0 = 2\pi c/\omega$. The lifetimes τ of the $5p\,^2P_{1/2}$ and $5p\,^2P_{3/2}$ excited states are from [63], and the corresponding decay rates are calculated from these values by $\Gamma = 1/\tau$. The ground state hyperfine splittings are from [64] and the $5p\,^2P_{1/2}$ and $5p\,^2P_{3/2}$ excited state hyperfine splittings are from [65] and [62] respectively.
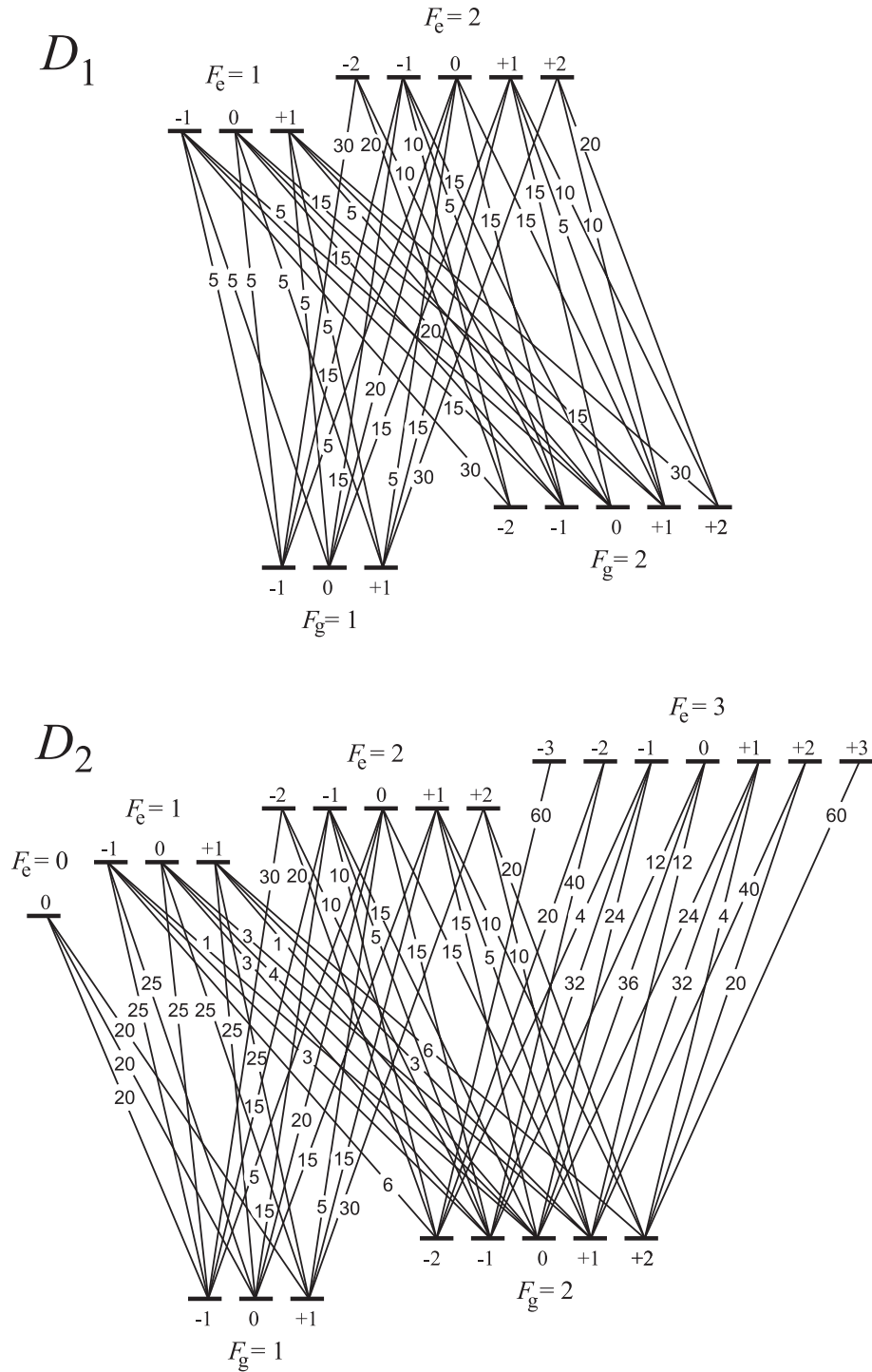
Figure 2.4: Relative transition strengths $60d_{F_gF_e}^2 \langle F_g m_{F_g} 1q | F_e m_{F_e} \rangle^2$ for transitions between all magnetic sub-levels of the D_1 and the D_2 lines.

3 Feasibility study for dipole traps at alternative wavelengths

We present a pre-study of alternatives for the CO_2 laser wavelength to produce a Bose-Einstein condensate of ^{87}Rb in a strongly focused dipole trap [40, 41, 66]. In these experiments the atoms are transferred from a magneto-optic trap to a far off-resonance dipole trap. Based on a calculation, we show that the light shift behavior of the ^{87}Rb $5s\,^2S_{1/2}$ ground state and $5p\,^2P_{3/2}$ excited state for optical frequencies corresponding to wavelengths larger than 1.6 μm is similar to their behavior at the CO_2 laser wavelength of 10.6 μm. In particular laser light around a wavelength of 2 μm has several practical advantages over a CO_2 laser. Sufficiently high power lasers recently became available at this wavelength.

3.1 Introduction

Recently there have been several experiments where Bose-Einstein condensation (BEC) was observed using all-optical techniques. The atoms are trapped in a far off-resonance dipole trap (FORT) or a quasi electro-static trap (QUEST) and a subsequent phase of forced evaporation results in phase-space densities larger than one. The difference between the two types of traps is somewhat arbitrary, since they are both far detuned dipole traps. A QUEST is by definition a dipole trap where the laser frequency is less then half the frequency of the first allowed electric dipole resonance [67]. Some of these experiments load a QUEST from atoms in a magneto-optic trap. BEC is then only achieved when the trap was created by a tightly focussed CO_2 laser. Equivalent approaches with neither Nd:YAG lasers, nor Ti:Sapphire lasers were successful.

In the first section of this chapter we will show that this is very likely due to the light shifts of the atomic levels in the field of the CO_2 laser. In the next section we will derive expressions that will enable us to calculate these light shifts for arbitrary atomic levels. Subsequently we will test the accuracy of these expressions by a comparison with experimental results for Rb. Finally we will use them to find other wavelengths that give rise to similar light shifts as a CO_2 laser.

3.2 Earlier QUEST experiments

Since the first results in laser cooling and trapping people have attempted to reach Bose-Einstein condenstation (BEC) using these, all optical, techniques. Presently, quantum degenerate samples of atoms have been created by all optical means, for several atomic species ^{87}Rb [40, 41, 66], ^{174}Yb [68], ^{133}Cs [43, 69]. Also a degenerate Fermi gas of ^{6}Li atoms has been created in an all-optical way [70]. However, no dissipative laser-cooling techniques were used, instead the atoms are trapped in a (quasi) conservative FORT or QUEST trap. The subsequent process of forced evaporation, similar to what is used in conventional, magnetically confined BEC experiments [33, 34] resulted in a sufficient increase of phase-space density to reach the BEC threshold.

The general loading procedure is similar for virtually all experiments. In the first stage several million atoms are collected and pre-cooled in a magneto-optic trap (MOT). In the next stage the detuning of the cooling lasers is increased to $\approx -20\Gamma$ and the repumper power is significantly reduced, thus creating a so called temporal dark-MOT. During this phase atoms can be collected in a state that is decoupled from the cooling process. In this state atoms can be collected in the potential minimum of the QUEST at higher densities than achievable with straightforward laser cooling. Adams *et al.* [71] first presented this technique to achieve high densities in a FORT. Kuppens *et al.* [72] present a thorough investigation of the loading process of a FORT. However they focus on traps with a detuning of a few nanometers and therefore disregard effects of the excited-state light shift.

All BEC experiments that use the above described loading scheme report a

remarkably high density immediately after loading the QUEST. Several explanations have been suggested. They do not exclude each other and more processes may play a role. Barrett *et al.* [40] propose a local dark-MOT; the light shift due to the strongly focussed, crossed CO_2 beams causes the repumper to be locally off resonant. For a crossed-beam geometry there seems to be consensus that these high densities are likely due to elastic atom-atom collisions from atoms that are trapped in either of the two beams and one of the two ending up in the potential well of the crossed region. This process is similar to the loading of the "dimple trap" [73]. This line of thought is confirmed by [74] where several istopes of Yb atoms are first loaded from a MOT in a single-beam FORT and subsequently a second FORT is switched on after the MOT is switched off. The fraction of atoms in the crossed region is observed to increase significantly with time for the bosonic isotopes, while for the fermionic isotopes this increase is much smaller.

Similar compression effects, although in a completely different geometry, have been observed in the Cs experiments [43, 69]. In Ref. [69] the atoms are pre-cooled to a high phase-space density and subsequently transferred to a large volume, shallow crossed CO_2 QUEST. Switching on a tightly focused YAG laser results in trapping of a substantial fraction ($\approx 15\%$) in the YAG FORT while the phase-space density is increased by an order of magnitude. In Ref. [43] atoms are trapped near a dielectric surface in a gravito-optical surface trap (GOST). Adding a strongly focused YAG beam yielded a 300 times density increase [44].

A comparison of single-beam and crossed-beam BEC experiments, performed by Cennini *et al.* [41], does however not show a remarkable difference in results. The density after transfer to the QUEST and thermalization of the sample shows an even higher density in the single-beam experiment than in the crossed-beam experiment. However, also the temperature is higher in the single-beam case, resulting in a lower phase-space density.

In the case of loading a QUEST directly from a MOT other processes must play a role. The density increase observed in experiments where CO_2 lasers were employed was not observed in experiments where the trap was created by a YAG laser. Experiments by Adams *et al.* [71] illustrate this point. In e.g. [75], where a CO_2 QUEST was used, this density increase was observed although in their case it was probably limited by the small number of atoms in their MOT and the relatively large CO_2 beam waist.

Cennini *et al.* [66] propose another explanation for the difference between the loading of YAG and CO_2 traps from a MOT. They note that although the light shift due to a YAG laser is attractive for ground-state Rb atoms, it is repulsive for the excited state used in laser cooling. This has two consequences. Firstly the atoms are pushed out of the trapping region when they are in the excited state. Since the near-resonant laser-cooling beams are still on, the excited state is macroscopically populated even though the repumper intensity is decreased at the end of the FORT loading process. Secondly the light shifts of the ground and excited states increase the energy difference between these two states. This results in a larger detuning of the cooling lasers, and thus less efficient laser cooling in the FORT trapping region. In the case of a CO_2 trap both these effects work constructively. The light

		Adams *et al.* [71]				Friebel *et al.* [75]			
element		^{23}Na				^{85}Rb			
trap type		crossed YAG				standing-wave CO_2			
MOT/molasses									
MOT	δ_{MOT}					-24	MHz	-4.0	Γ
dark-MOT	δ_{dMOT}					-108	MHz	-18.0	Γ
# atoms in MOT	N_{MOT}						10^6		
dipole trap parameters									
power per beam	P		4	W			10	W	
trap frequencies	$\omega/2\pi$						$(0.72, 0.72, 15)$	kHz	
beam waist	w		15	μm			≈ 100	μm	
FORT level shifts									
$^2S_{1/2}$ shift	U_0	-9	MHz			-8	MHz	-1.3	Γ
$^2P_{3/2}$ shift		$\approx +9$	MHz			-20	MHz	-3.3	Γ
differential shift		$\approx +18$	MHz			-12	MHz	-2.0	Γ
FORT info									
# trapped atoms	N_{FORT}								
temperature	T_{FORT}		140	μK					
density	n_{FORT}		$4^{+6}_{-2} \times 10^{12}$	cm^{-3}			3.1×10^{13}	cm^{-3}	
phase-space dens.	PSD								

		Barrett *et al.* [40]				Cennini *et al.* [41, 66]			
element		^{87}Rb				^{87}Rb			
trap type		crossed CO_2				single-beam CO_2			
MOT/molasses									
MOT	δ_{MOT}	-15	MHz	-2.5	Γ	-18	MHz	-3.0	Γ
dark-MOT	δ_{dMOT}	-140	MHz	-23.3	Γ	-160	MHz	-26.7	Γ
# atoms in MOT	N_{MOT}		$3. \times 10^7$				$6. \times 10^7$		
dipole trap parameters									
power per beam	P		12	W			28	W	
trap frequencies	$\omega/2\pi$		1.5	kHz			$(4.8, 4.8, 0.35)$	kHz	
beam waist	w		≈ 50	μm			27	μm	
FORT level shifts									
$^2S_{1/2}$ shift	U_0	-9.3	MHz	-1.5	Γ	-35	MHz	-5.8	Γ
$^2P_{3/2}$ shift		-25.1	MHz	-4.2	Γ	-95	MHz	-15.8	Γ
differential shift		-15.8	MHz	-2.6	Γ	-60	MHz	-10.0	Γ
FORT info									
# trapped atoms	N_{FORT}		6.7×10^5						
temperature	T_{FORT}		38	μK			140	μK	
density	n_{FORT}		$2. \times 10^{14}$	cm^{-3}			1.2×10^{13}	cm^{-3}	
phase-space dens.	PSD		$\frac{1}{200}/3$				$1.2 \times 10^{-4}/3$		

Table 3.1: A comparison of some experiments where a FORT is loaded directly from a MOT. The achieved densities, temperatures and phase-space densities in the FORT are given for a sample in thermal equilibrium. They should be compared with typical values for a MOT. Note that the FORT level shifts are significant with respect to the applied detunings of the MOT laser.

shifts of atomic levels due to the CO_2 laser light can be approximated by the DC polarizabilities of these levels. The excited-state light shift is 2.7 times larger than the ground-state light shift. The excited-state atoms are therefore even more deeply trapped than the ground-state atoms. Furthermore the energy difference between the ground state and the excited state becomes smaller which results in more efficient laser cooling in the QUEST trapping region.

The reported Cs experiments are not sensitive for the excited-state light shifts, since the atoms are transferred from a conservative trap to a FORT. The excited state is not populated in this scenario and high densities can be realized even using a YAG laser.

Table 3.1 shows a comparison of four experiments where a FORT or QUEST is loaded directly from a MOT. The achieved densities, temperatures and phase-space densities in the trap are quoted values after the sample has reached thermal equilibrium. These values should be compared with values for a MOT, where the density is typically $\sim 10^{11}$ cm^{-3} and the phase-space density is typically $\sim 10^{-6}$. Note that the level shifts are significant with respect to the applied detunings of the MOT laser. During the MOT phase the cooling laser will be even blue detuned in the center of the QUEST. In order to be able to load a deep QUEST it is clearly important to use a sufficiently large detuning of the cooling laser during the dark-MOT phase.

3.3   Dipole polarizability tensor

In order to calculate the light shift of a particular level for a particular choice of the optical frequency we need to know its polarizability at this frequency. Experimentally little is known about Rb polarizabilities. Most experiments have been performed using static electric fields, determining values for the DC polarizabilities. The Rb (phase-space) density increase has so far been reported in experiments using CO_2 lasers. Their frequency is so low that the polarizabilities at this wavelength are well approximated by the (experimentally determined) DC polarizabilities. When we are looking for similar effects for other, higher frequencies of the light we need to rely on calculations.

The first part of this section describes how the level shifts can be calculated using known values of the polarizability. The next part focusses on deriving general equations to calculate the dipole polarizability tensor. Finally some approximations are performed to achieve equations that are practically usable.

3.3.1   Light shift

Similar to Eq. (2.49) the light shift of a certain atomic level can be calculated by

$$\mathbf{U}_{\text{dip}} = -\frac{1}{2}\langle \widetilde{\mathbf{E}}^{\dagger} \cdot \mathbf{d} \rangle = -\frac{1}{4}\widetilde{\mathbf{E}}^{\dagger} \cdot \boldsymbol{\alpha} \cdot \widetilde{\mathbf{E}}. \tag{3.1}$$

The indices of the tensor $\mathbf{U}$ are the initial and final magnetic sub-states of this atomic level. The eigenvalues of $\mathbf{U}$ are the light shifts of the various magnetic sub-

levels. The last part of Eq. (3.1) is valid when the induced dipole $\mathbf{d}$ is proportional to the applied electric field $\mathbf{E}$. Moments with even powers of $\mathbf{E}$ are zero, because the relation $\mathbf{d}(\mathbf{E}) = -\mathbf{d}(-\mathbf{E})$ is not fulfilled. This relation should be fulfilled in the case of atoms, since these are symmetrical. For non-symmetrical particles, such as molecules, even powers of $\mathbf{E}$ can appear. Higher moments with odd powers of $|\mathbf{E}|$ are only significant for very high laser powers (non-linear optics). The brackets $\langle \cdot \rangle$ denote averaging over a period of the optical field. Bonin and Kadar-Kallen [76, 77] present a general description to calculate $\mathbf{d}$, although they do not always give a complete derivation of their equations or references thereof.

3.3.2 Dipole polarizability tensor

Contrary to the treatment of the polarizability tensor $\boldsymbol{\alpha}$ in chapter 2, we can now not limit ourselves to the case where the detunings of the applied fields with respect to the transition frequencies are small, so that the rotating wave approximation can no longer be applied. For $|\delta| \gg \Gamma$ and low saturation (so that spontaneous emission processes can be neglected) the polarizability tensor becomes

$$\boldsymbol{\alpha} = \underset{F'm'}{\mathbf{S}} \left(\frac{\langle Fm''|\widehat{\mathbf{D}}|F'm'\rangle\langle F'm'|\widehat{\mathbf{D}}|Fm\rangle}{\hbar\left(\omega_{FF'} - \omega\right)} + \frac{\langle Fm''|\widehat{\mathbf{D}}^{\dagger}|F'm'\rangle\langle F'm'|\widehat{\mathbf{D}}^{\dagger}|Fm\rangle}{\hbar\left(\omega_{FF'} + \omega\right)} \right).$$
(3.2)

It has the same indices as the polarizability tensor derived in chapter 2: the initial and final magnetic substates m and m'' and the polarizations q and q' of the absorbed and emitted photons, necessary to make this Raman transition. The symbol $\mathbf{S}$ denotes summation over discrete indices and integration over continuum states, and $\widehat{\mathbf{D}}$ denotes the dipole operator. The frequency difference between the states $|F\rangle$ and $|F'\rangle$ is $\omega_{FF'}$, and ω is the frequency of the driving field.

It is customary in the literature [76, 77] to expand the polarizability tensor as follows

$$\widehat{\boldsymbol{\alpha}}_{ij} = \alpha_0\widehat{\boldsymbol{\delta}}_{ij} - \alpha_1(\widehat{\mathbf{F}}_i\widehat{\mathbf{F}}_j - \widehat{\mathbf{F}}_j\widehat{\mathbf{F}}_i) + \alpha_2\frac{\frac{3}{2}(\widehat{\mathbf{F}}_i\widehat{\mathbf{F}}_j + \widehat{\mathbf{F}}_j\widehat{\mathbf{F}}_i) - F(F+1)\widehat{\boldsymbol{\delta}}_{ij}}{F(2F-1)},$$
(3.3)

with i, j denoting cartesian coordinates, $\widehat{\boldsymbol{\delta}}_{ij}$ the identity operator, and $\widehat{\mathbf{F}}_i$ the angular momentum operator. It is written as an operator, but squeezed between an initial state $|Fm\rangle$ and a final state $|Fm''\rangle$, it is equal to Eq. (3.2). The scalar polarizability α_0 describes e.g. the index of refraction of a vapor of atoms with randomly oriented spin directions. The vector polarizability α_1 can give a contribution for states with $F \geq \frac{1}{2}$, and describes phenomena like paramagnetic Faraday rotation of plane polarized light by spin polarized atomic vapors. The tensor polarizability α_2 can give a contribution for states with $F \geq 1$, and describes e.g. birefringence of a vapor of spin-aligned atoms.

The frequency-dependent scalar, vector, and tensor polarizabilities are defined

by

$$\alpha_0 = \frac{2}{3\hbar(2F'+1)} \underset{F'}{\mathbf{S}} \frac{\phi_0(F,F')\omega_{FF'}}{\omega_{FF'}^2 - \omega^2}(F'\|\widehat{\mathbf{D}}\|F)^2,$$

$$\alpha_1 = \frac{1}{\hbar(2F'+1)} \underset{F'}{\mathbf{S}} \frac{\phi_1(F,F')\omega}{\omega_{FF'}^2 - \omega^2}(F'\|\widehat{\mathbf{D}}\|F)^2, \tag{3.4}$$

$$\alpha_2 = \frac{2}{3\hbar(2F'+1)} \underset{F'}{\mathbf{S}} \frac{\phi_2(F,F')\omega_{FF'}}{\omega_{FF'}^2 - \omega^2}(F'\|\widehat{\mathbf{D}}\|F)^2.$$

A difference in frequency dependence occurs because the scalar and tensor polarizabilities are the symmetric part of the polarizability tensor $(\boldsymbol{\alpha} + \boldsymbol{\alpha}^\dagger)/2$, while the vector polarizability is the anti-symmetric part $(\boldsymbol{\alpha} - \boldsymbol{\alpha}^\dagger)/2$. Since α_1 is proportional to ω whereas α_0 and α_2 are proportional to $\omega_{FF'}$, the vector polarizability will become less important with respect to the other contributions for larger wavelengths of the driving field. For DC fields it is equal to zero.

The factor $(F'\|\widehat{\mathbf{D}}\|F)$ denotes the reduced dipole matrix element as defined in the previous chapter. Because it is more convenient in this case and more general in the literature the alternative definition of the reduced dipole matrix elements mentioned in section 2.3.2 will be used in this chapter. The distinction between the two definitions is maintained by using a notation with parentheses $(\cdot\|\cdot\|\cdot)$ instead of the notation with angular brackets $\langle\cdot\|\cdot\|\cdot\rangle$ which was used in the previous chapter. The reduced matrix elements for the hyperfine structure levels can be simplified using a transformation similar to Eqs. (2.42) and (2.43)

$$(F'\|\widehat{\mathbf{D}}\|F)^2 = (2F'+2)(2F+1) \left\{ \begin{matrix} F & F' & 1 \\ J' & J & I \end{matrix} \right\}_{6j}^2 (J'\|\widehat{\mathbf{D}}\|J)^2. \tag{3.5}$$

The factors $\phi_0(F,F')$, $\phi_1(F,F')$, and $\phi_2(F,F')$ are given by

$$\phi_0(F,F') = \delta_{F',F-1} + \delta_{F',F} + \delta_{F',F+1}, \tag{3.6}$$

$$\phi_1(F,F') = -\frac{1}{F}\delta_{F',F-1} - \frac{1}{F(F+1)}\delta_{F',F} + \frac{1}{F+1}\delta_{F',F+1},$$

$$\phi_2(F,F') = -\delta_{F',F-1} + \frac{2F-1}{F+1}\delta_{F',F} - \frac{F(2F-1)}{(F+1)(2F+3)}\delta_{F',F+1},$$

where δ_{mn} represents the Kronecker delta. For DC fields a thorough derivation of the scalar and tensor polarizability pre-factors is presented in [78, 79].

As will be obvious in the next section, it is sometimes convenient to work with oscillator strengths instead of dipole matrix elements. The dimensionless oscillator strength $f_{FF'}$ is defined by

$$f_{FF'} = \frac{2m_{\mathrm{e}}}{3\hbar e^2} \frac{\omega_{FF'}}{2F'+1} |(F'\|\widehat{\mathbf{D}}\|F)|^2. \tag{3.7}$$

It will be especially useful to express the scalar polarizability in terms of the oscillator strength

$$\alpha_0 = \frac{e^2}{m_{\mathrm{e}}} \underset{F'}{\mathbf{S}} \frac{\phi_0(F,F')f_{FF'}}{\omega_{FF'}^2 - \omega^2}. \tag{3.8}$$

3.3.3   Approximations of polarizability tensor

During the loading of the QUEST trap also the MOT lasers and the quadrupole magnetic field are present. These might influence the effectiveness of the QUEST trap. If we compare the QUEST light shifts mentioned in Table 3.1 with the Zeeman shift of a typical MOT magnetic field gradient of 10 G/cm over a typical trap width, we see that the former is much larger than the latter. The presence of the MOT magnetic field thus doesn't influence the QUEST trap in the parameter range that we consider. The presence of the MOT beams mainly result in the destruction of the spin alignment of the atoms due to scattering. However, the typical scattering rate of 100 kHz is very low compared to the frequency with which an atomic dipole aligns with the applied electric field. We therefore conclude that even in the presence of a MOT, the description of the light shift in a QUEST trap as derived in this section is valid.

For linearly polarized light only the $\widehat{\alpha}_{zz}$ component of the polarizability tensor needs to be considered. Furthermore if the quantization axis of the atom is taken parallel to this polarization, the off-diagonal elements $\langle Fm''|\widehat{\alpha}_{zz}|Fm\rangle$ are zero. Therefore $\langle Fm|\widehat{\alpha}_{zz}|Fm\rangle$ are the eigenvalues of the $\widehat{\alpha}_{zz}$ operator. Eqs. (3.3), (3.4), and (3.6) then reduce to

$$\alpha_{zz} = \langle Fm|\widehat{\alpha}_{zz}|Fm\rangle = \alpha_0 + \alpha_2 \frac{3m^2 - F(F+1)}{F(2F-1)}. \tag{3.9}$$

This is an expression that is generally found throughout the literature [80, 81]. From this expression we can understand the pre-factor of the tensor polarizability term. It is chosen such that in this particular approximation of the polarizability it becomes equal to 1 for states with $m = F$.

3.4   Specific situation for rubidium

3.4.1   Discussion of unit systems

The S.I. unit of polarizability is $\mathrm{Cm^2/V}$. The equations presented in section 3.3 also require S.I. units. In the literature however, experimental values are often specified in cgs units of $\mathrm{cm^3}$ or $\mathrm{\AA^3} = 10^{-24}\ \mathrm{cm^3}$, whereas theoretical values tend to be given in a_0^3, with a_0 the Bohr radius. Values can be converted between these unit systems by the following relations.

$$\begin{aligned}
\alpha[\mathrm{cm^3}] = & \quad 10^6 a_0^3 \alpha[a_0^3] \quad = 1.48184 \times 10^{-25} \alpha[a_0^3], \\
\alpha[\mathrm{Cm^2/V}] = & \ 4\pi 10^{-6}\varepsilon_0 \alpha[\mathrm{cm^3}] = 1.11265 \times 10^{-16} \alpha[\mathrm{cm^3}], \\
\alpha[\mathrm{Cm^2/V}] = & \quad 4\pi\varepsilon_0 a_0^3 \alpha[a_0^3] \quad = 1.64878 \times 10^{-41} \alpha[a_0^3].
\end{aligned} \tag{3.10}$$

The S.I. unit $\mathrm{Cm^2/V}$ is equivalent to $\mathrm{J/(V/m)^2}$ from which is clear that it can be convenient to express the polarizability as α/h, which has a unit $\mathrm{Hz/(V/m)^2}$ and gives rather straightforwardly the level shift for a given electric field. The S.I. unit for a dipole $\mathbf{d}$ or a reduced dipole matrix element is Cm.

Rb transition	$(n'J'\|\widehat{\mathbf{D}}\|nJ)$ (ea_0)		$f_{JJ'}$	λ_0
	calculated	experimental	(10^{-3})	(nm)
$5s\,{}^2S_{1/2} \to 5p\,{}^2P_{1/2}$	4.221	4.231(3)	341.8(5)	794.979
$5s\,{}^2S_{1/2} \to 5p\,{}^2P_{3/2}$	5.956	5.977(4)	694.9(5)	780.242
$5s\,{}^2S_{1/2} \to 6p\,{}^2P_{1/2}$	0.333		3.99	421.672
$5s\,{}^2S_{1/2} \to 6p\,{}^2P_{3/2}$	0.541		10.6	420.298
$5s\,{}^2S_{1/2} \to 7p\,{}^2P_{1/2}$	0.115		0.559	359.259
$5s\,{}^2S_{1/2} \to 7p\,{}^2P_{3/2}$	0.202		1.73	358.807
$5s\,{}^2S_{1/2} \to 8p\,{}^2P_{1/2}$	0.059		0.158	335.178
$5s\,{}^2S_{1/2} \to 8p\,{}^2P_{3/2}$	0.111		0.558	334.968
$5p\,{}^2P_{1/2} \to 5s\,{}^2S_{1/2}$	4.221	4.231(3)	$-341.8(5)$	794.979
$5p\,{}^2P_{1/2} \to 6s\,{}^2S_{1/2}$	4.119		0.1945	1323.879
$5p\,{}^2P_{1/2} \to 7s\,{}^2S_{1/2}$	0.954		19.0	728.2003
$5p\,{}^2P_{1/2} \to 8s\,{}^2S_{1/2}$	0.504		6.35	607.2436
$5p\,{}^2P_{1/2} \to 4d\,{}^2D_{3/2}$	7.847		633.3	1475.644
$5p\,{}^2P_{1/2} \to 5d\,{}^2D_{3/2}$	1.616		52.01	762.1030
$5p\,{}^2P_{1/2} \to 6d\,{}^2D_{3/2}$	1.180		34.04	620.8026
$5p\,{}^2P_{3/2} \to 5s\,{}^2S_{1/2}$	5.956	5.977(4)	$-347.5(5)$	780.242
$5p\,{}^2P_{3/2} \to 6s\,{}^2S_{1/2}$	6.013		200.8	1366.875
$5p\,{}^2P_{3/2} \to 7s\,{}^2S_{1/2}$	1.352		18.72	741.0214
$5p\,{}^2P_{3/2} \to 8s\,{}^2S_{1/2}$	0.710		6.21	616.1331
$5p\,{}^2P_{3/2} \to 4d\,{}^2D_{3/2}$	3.540		62.19	1529.261
$5p\,{}^2P_{3/2} \to 4d\,{}^2D_{5/2}$	10.634		561.12	1529.366
$5p\,{}^2P_{3/2} \to 5d\,{}^2D_{3/2}$	0.787		6.06	776.1571
$5p\,{}^2P_{3/2} \to 5d\,{}^2D_{5/2}$	2.334		53.28	775.9786
$5p\,{}^2P_{3/2} \to 6d\,{}^2D_{3/2}$	0.558		3.75	630.0966
$5p\,{}^2P_{3/2} \to 6d\,{}^2D_{5/2}$	1.658		33.11	630.0067

Table 3.2: Data of some relevant transitions. Reduced dipole matrix elements in atomic units as calculated by Safronova *et al.* [82, 83]. The experimental matrix elements of the D_1 and the D_2 lines are from [63]. The values can be converted to S.I. units by multiplication by $ea_0 = 8.47836 \times 10^{-30}$ Cm. The oscillator strengths $f_{JJ'}$ of these transitions are calculated from the experimental reduced dipole matrix elements whenever available and from the calculated elements otherwise. The wavelengths λ_0 of the transitions are from [84]

For the reduced dipole matrix elements of the transitions in Rb mainly theoretical values are reported. They are specified in atomic units. These can be converted to S.I. units by

$$\mathbf{d}[\text{Cm}] = ea_0\mathbf{d}[ea_0] = 8.47835 \times 10^{-30}\mathbf{d}[ea_0]. \tag{3.11}$$

3.4.2 Dipole matrix elements and transition energies

In order to calculate polarizabilities we need values for the reduced dipole matrix elements of the transitions in Rb and values for the energy differences between particular levels. Only for the $5s\,{}^2S_{1/2} \to 5p\,{}^2P_{1/2}$ and $5s\,{}^2S_{1/2} \to 5p\,{}^2P_{3/2}$ transitions
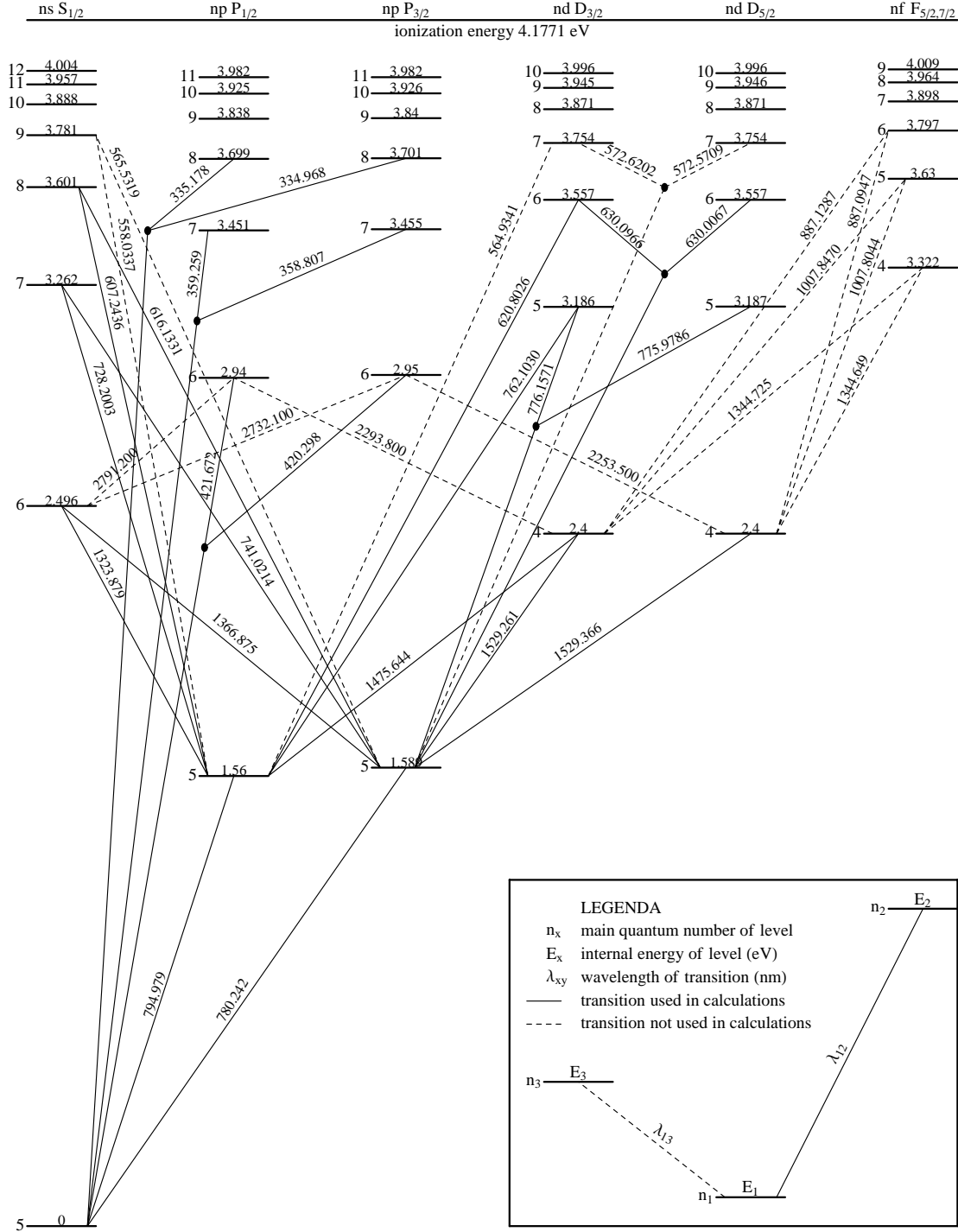
Figure 3.1: Grotrian diagram of the spectrum of Rb. The wavelength values are from [84] and are assigned to a particular transition by comparison with the less accurate data from [85]. The ionization energy is also from [84].

experimental values are known [63]. In this paper a measurement of the line strength $\mathcal{S}$ of the $5s \rightarrow 5p$ transition is presented. The value of $\mathcal{S}$ can be converted to a reduced dipole matrix element using the relation $(L_{5\mathrm{p}}\|\widehat{\mathbf{D}}\|L_{5\mathrm{s}}) = \sqrt{\mathcal{S}_{5s\rightarrow 5p}/(2S+1)}$, [52]. By means of Eqs. (2.44) and (2.45) the reduced dipole matrix elements of the D_1 and the D_2 lines can be derived, which results in 4.231(3) ea_0 and 5.977(4) ea_0 respectively. For several other transitions Safronova *et al.* have calculated values [82, 83]. For convenience, the values which will be used to calculate the polarizability are given in Table 3.2. Values for the energy differences between two levels are derived from wavelength data taken from [84]. The wavelengths in this reference are assigned to a particular transition by comparison with the less accurate data from [85]. These data are shown in a Grotrian diagram in Fig. 3.1. Only the transitions which are shown in solid lines are used in the calculations, limited by the availability of known reduced dipole matrix elements. Transitions indicated with dashed lines are not used in the calculations.

For an effective one electron system, the sum rule

$$\sum_{J'} f_{JJ'} = 1 \tag{3.12}$$

applies for the oscillator strength as defined by Eq. (3.7). With this rule we can check whether the important transitions from a certain initial state are taken into account. In order to calculate the light shift of the $5s\,{}^2S_{1/2}$ ground state, sufficient levels are taken into account, since the oscillator strengths of this level, shown in table 3.2, indeed add up to approximately one. For the $5p\,{}^2P_{1/2}$ and $5p\,{}^2P_{3/2}$ excited states the oscillator strengths add up to 0.597 and 0.600 respectively. It seems that many important transitions are lacking. Although these are all highly excited and continuum states, and we thus expect their influence on the polarizabilities in the infrared range we are interested in to be limited, we will try incorporate this missing oscillator strength.

Since we are interested in a wavelength range that is far detuned with respect from the missing transitions, it is reasonable to introduce a fictitious extra level at the ionization energy. We will take the oscillator strength of the transition between this extra level and either of the $5p\,{}^2P_{1/2}$ and $5p\,{}^2P_{3/2}$ states equal to the lacking oscillator strength f_c. We can not attribute sub-structure to this extra level, so we will only determine the contribution of this fictitious level to the scalar polarizability. Analogous to Eq. (3.8) this contribution consists of the addition of an extra term

$$\alpha_\mathrm{c} = \frac{e^2}{m_\mathrm{e}}\frac{f_\mathrm{c}}{\omega_\infty^2 - \omega^2}, \tag{3.13}$$

with $\hbar\omega_\infty$ is the ionization energy of either of the $5p\,{}^2P_{1/2}$ or $5p\,{}^2P_{3/2}$ states.

Apart from the contribution of the valence electron, there is a contribution from the core (non-valence electrons). Also these electrons are coupled to excited states and give a contribution to the polarizability. Johnson *et al.* [86] calculate this contribution to the scalar polarizability to be 9.3 $a_0^3 = 1.5 \times 10^{-40}$ Cm^2/V. Since these are deeply-bound electrons, we assume it to be independent of the frequency

of the light, an assumption also made by Safronova *et al.* [83]. They also estimate the contribution of the not-incorporated levels and the continuum to the $5s\,^2S_{1/2}$ DC scalar polarizability to be $< 1‰$.

3.4.3   Comparison with experimental polarizability values

In the literature experimental and theoretical values of the scalar polarizability α_0 and the tensor polarizability α_2 are given for some Rb levels for DC electric fields. A summary of these values, converted to S.I. values, is shown in Table 3.3.

In order to test the accuracy of our calculations and of our method to take the missing oscillator strength into account, we have attempted to reproduce these experimental polarizabilities. Fine-structure polarizabilities can be calculated by replacing all F and F' by J and J' respectively in Eqs. (3.3)-(3.9); Eq. (3.5) does not apply. The theoretical reduced dipole matrix elements of Table 3.2 have been used, except for the D_1 and the D_2 lines for which the experimental values were used. The results of these calculations are presented in the last two columns of Table 3.3. The core polarizability which is discussed in section 3.4.2 has been incorporated in the calculation of α_0. It is obvious that our calculations without the correction term α_c yield systematically lower results while the experimental values are reproduced well when the correction term α_c is added to the polarizability.

Due to the limited number of (especially short wavelength) transitions which are taken into account in the calculations we expect a breakdown of the calculations for the $5s\,^2S_{1/2}$ state below 400 nm, and for the $5p\,^2P_{1/2}$ and $5p\,^2P_{3/2}$ states below 700 nm. For wavelengths above 1 μm, however, we do not expect problems.

3.5   Alternative QUEST wavelengths

Using Eqs. (3.9) and (3.4)-(3.6) and the reduced dipole matrix elements from Table 3.2 the entire spectra of the polarizabilities α of the $5s\,^2S_{1/2}$, $F = 1, 2$ states and the $5p\,^2P_{3/2}$, $F = 3$ state have been calculated for wavelengths λ_0 of 700 nm and

level & frequency	experimental polarizability values		calculated polarizability	
	10^{-39} Cm^2/V	ref.	without α_c 10^{-39} Cm^2/V	with α_c 10^{-39} Cm^2/V
$\alpha_0(5s\,^2S_{1/2})$ (DC)	5.3 (1)	[87]	5.25	5.25
$\alpha_0(5s\,^2S_{1/2})$ (1064 nm)	12.7 (1.0)	[76]	11.34	11.34
$\alpha_0(5p\,^2P_{1/2})$ (DC)	13.4 (1)	[88]	12.40	13.11
$\alpha_0(5p\,^2P_{3/2})$ (DC)	14.13 (17)	[81]	13.39	14.12
$\alpha_2(5p\,^2P_{3/2})$ (DC)	-2.69 (6)	[81]	-2.6	-2.6

Table 3.3: Experimental DC values of polarizabilities of some Rb levels including references. All values have been converted to S.I. units. The calculated values are shown without and with the correction term α_c.

higher. The correction term α_c has been taken into account in the calculations of the latter spectrum. The results are shown in Figs. 3.2(a) and (b). The tails at the long wavelength side gradually tend to the DC polarizability values. The solid lines are the scalar polarizabilities. For the $5s\,^2S_{1/2}$ ground state, the polarizability is equal for both hyperfine levels and the tensor polarizability vanishes.

Examining the spectra with the criterion that both the ground and excited-state polarizabilities must be positive, so that both states are in an attractive potential gives two wavelength regions for which this criterium is fulfilled. The first is between the excited-state resonance with the $6s\,^2S_{1/2}$ state at 1366 nm and the zero crossing at approximately 1400 nm. The second is for wavelengths larger than that of the excited-state resonance with the $4d\,^2D_{3/2,5/2}$ states at 1529 nm.

The first region is a rather narrow window where the excited-state polarizability depends strongly on the wavelength. Using a tunable laser in this wavelength region would thus allow us to change the local laser-cooling efficiency in the QUEST region, while keeping the QUEST trap depth, the $5s\,^2S_{1/2}$ polarizability constant. There are,
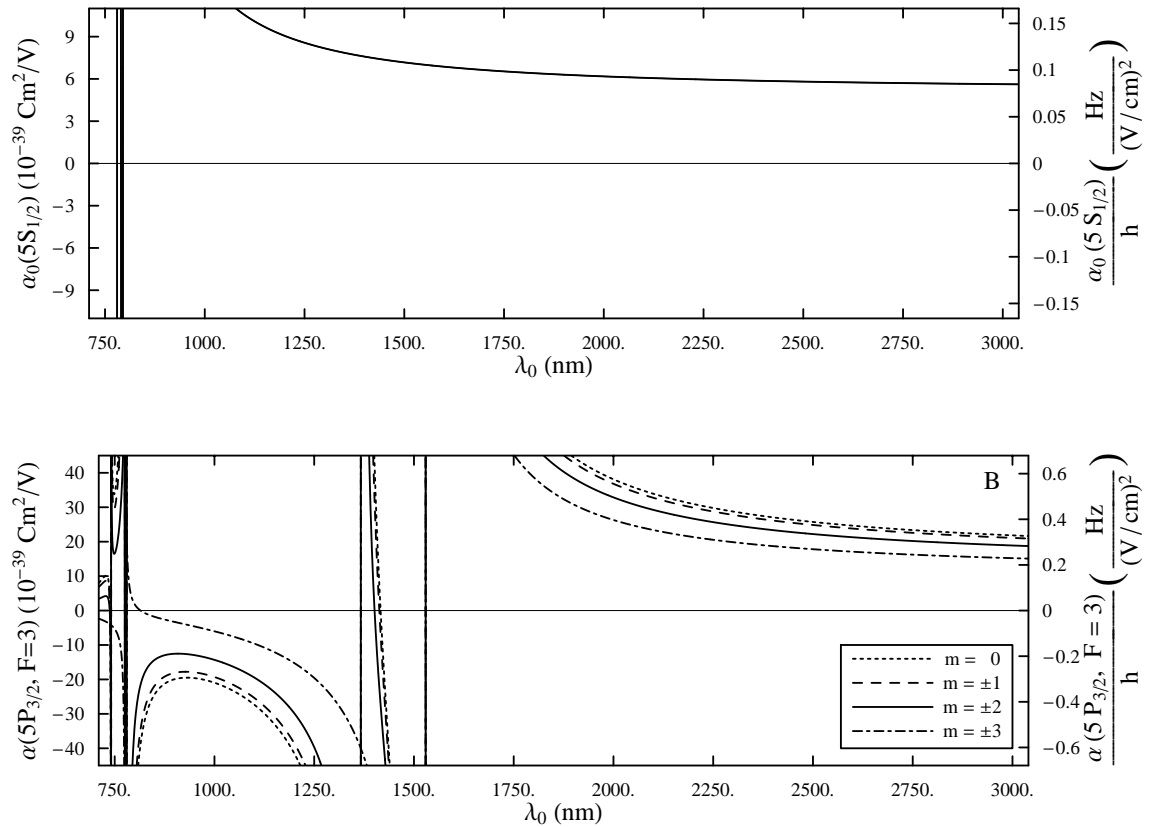

Figure 3.2: Polarizability plots for (a) the $5s\,^2S_{1/2}$, $F = 1, 2$ states and (b) the magnetic sub-states of the $5p\,^2P_{3/2}$ $F = 3$ state of ^{87}Rb, for a linearly polarized light field. On the large wavelength side the curves gradually tend to their DC values. The $5p\,^2P_{3/2}$ scalar polarizability overlaps with the $m = 2$ curve.
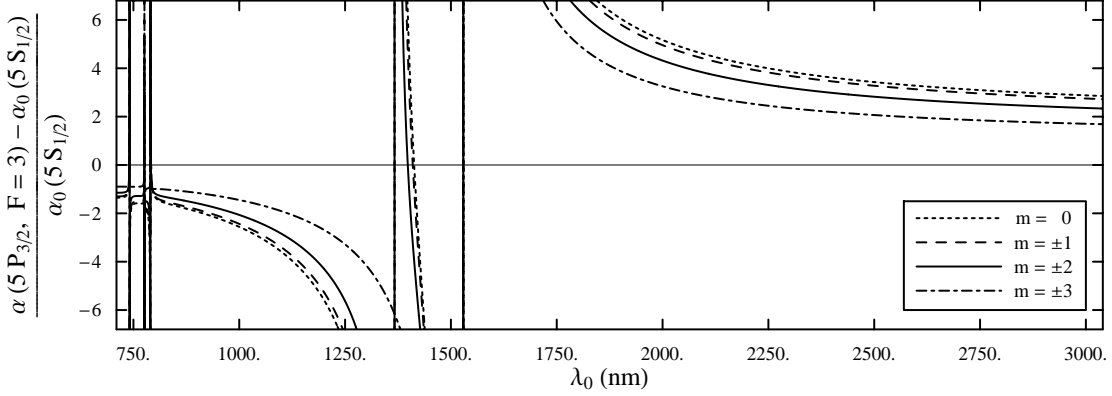
Figure 3.3: The difference in polarizability between the ground-state and excited-state sub-state relative to the ground-state polarizability versus wavelength λ_0. This graph is useful to determine the differential light shift for a given value of the FORT trap depth.

however, no lasers available in this wavelength region with sufficient power.

In the second wavelength region, lasers have recently become available that are suitable for these purposes. There are e.g. erbium and thulium fiber lasers, which operate between 1530 to 1620 nm and 1750 to 2200 nm respectively. Both are available up to 150 W CW output power in a single spatial mode, $M^2 < 1.1$. The linewidth of these lasers is however rather large, specified to be smaller than 1.0 nm, which corresponds to a coherence length of a few millimeters. These wavelengths have some favorable properties compared to the CO_2 laser wavelength of 10.6 μm from an experimentalist point of view. Most standard optical materials, such as BK7, flint glasses, and quartz (fused silica), are still transparent for these wavelengths. So no special vacuum windows are needed, and even a quartz cell can be used to perform the experiment, which enables one to keep the lenses outside the vacuum. Furthermore, it is easier to create small foci at a wavelength of 2 μm. A disadvantage of these wavelengths is the presence of a minor absorption peak of water around a wavelength of 2000 nm. This will, however, pose no serious limitations. For wavelengths that are too close to the 1529 nm resonance the excited-state light shift becomes very large, which would require an uncomfortably large detuning of the cooling lasers in order to keep them red detuned from the cooling transition.

Fig. 3.3 shows the difference in polarizability for the ground state and the magnetic sub-states of the excited state relative to the ground-state polarizability. This graph is very useful to determine the differential light shift between the excited and the ground state for a given QUEST trap depth. The long wavelength tail gradually decreases to the DC value of 1.68 for the $5p\,^2P_{3/2}$ scalar polarizability (which overlaps with the $m = \pm 2$ curve) or to 1.19 for the $5p\,^2P_{3/2}$ $F = \pm m = 3$ magnetic sub-state.

At a wavelength of 2 μm the polarizability of the $5s\,^2S_{1/2}$ state is 6.18×10^{-39} Cm^2/V. The scalar polarizability of the $5p\,^2P_{3/2}$ state is 3.28×10^{-38} Cm^2/V, while the total polarizability of the $F = \pm m = 3$ magnetic sub-state is 2.63×10^{-38} Cm^2/V. This leads to values of the relative polarizability difference of 4.32 and 3.26

respectively. For a moderate trap depth of 10 MHz as in the experiment by Barrett *et al.* [40], the differential light shift of the MOT cooling transition is 33 MHz. For tightly focussed QUEST beams with very deep trap depth of 30 MHz, so that the parameters of Cennini *et al.* [41, 66] are approached, the differential light shift of the MOT cooling transition will be 98 MHz. The detuning of the cooling lasers during the dark-MOT phase should be considerably larger than these values.

3.6 Conclusions

A wavelength of 2 μm is very promising for creating a QUEST. We predict that a 2 μm laser will show similar behavior as a CO_2 laser when it is used as a far off-resonance dipole trap for Rb. Both wavelengths create a confining potential for both the ground and the excited state of the $5s\,{}^2S_{1/2} \rightarrow 5p\,{}^2P_{3/2}$ transition, which is used for laser cooling.

A QUEST at 2 μm has some experimental advantages over a CO_2 laser QUEST. No special vacuum windows are needed and the experiment can even be performed in a quartz cell, which makes it possible to put the lenses outside the vacuum. Furthermore it is easier to create small foci at a wavelength of 2 μm. A slight disadvantage is that a larger detuning of the laser-cooling light is needed during the dark-MOT phase, in order to prevent the laser-cooling beams to be effectively blue detuned in the QUEST trap center. This is because the differential light shift for a given trap depth for a 2 μm laser is 2.68 times larger than the DC differential light shift.

4 Experimental setup

We discuss the several components of our experimental setup. The preparation of the laser beams with different frequencies is discussed and experimental parameters are presented. It is explained how these beams are used in the experiments. A very accurate method to determine the critical angle of a laser beam is presented. The vacuum system is discussed extensively insofar it has been altered with respect to previous descriptions of the setup [89, 90]. This concerns an alternative prism geometry, a quartz cell to provide optical access for the numerous laser beams used in the experiments, and the use of a dispenser that is used as the Rb source.

4.1 Laser park

This section discusses the laser setup that is used in the experiments described in this thesis. Several laser frequencies are necessary in the experiments. An overview of these is shown in Fig. 4.1. The purpose of these lasers will be explained in the following sub-sections. Fig. 4.2 schematically shows the setup of the lasers that are used near an atomic resonance.

4.1.1 Frequency locked diode lasers: master and repumper

There are two diode lasers locked to a ^{87}Rb spectral feature. One to the $F = 2 \rightarrow F' = (1, 3)$ cross-over of the D_2 line, and the other to the $F = 1 \rightarrow F' = 2$ transition of the D_1 line. Both lasers are 50 mW diode lasers with grating feedback [91, 92] in Littrow configuration [93]. A small fraction of the available optical power is used to obtain a Doppler-free saturation spectroscopy signal.

In order to frequency lock these laser diodes to a spectral feature a small RF signal is added to the laser current, which results in frequency sidebands on the laser light. A dispersive spectroscopy signal is obtained by mixing the spectroscopy signal with the RF oscillator [94, 95]. The resulting signal is used as feedback to the laser current in order to compensate for fast fluctuations. Furthermore it is integrated and sent to the piezo on which the grating is mounted, in order to compensate for long term drift.

The laser that is locked to the D_2 line is called the *master* laser, and is used as a frequency reference for two laser diodes that will be injection locked. These will be discussed in the next two sub-sections. The laser that is locked to the D_1 line is called the *repumper*, and is used to prevent atoms from ending up in the $F = 1$ ground state during the MOT and molasses stages of the experiment. Later in an experimental run it can also be used to pump all atoms to the $F = 2$ state by pulsing it on for a short time. A total power of 8 mW was obtained behind a single-mode (SM) optical fiber. It can be switched on and off within 100 μs by a mechanical shutter (*Vincent Associates, Uniblitz*, LS2T2), which is placed in the focus of a 1:1 telescope, in order to reduce the switching time.

4.1.2 MOT/molasses

Some light of the master laser is frequency shifted using a double-pass AOM setup. The frequency shifted light is injected into a the *MOT/molasses* laser diode through the unused output port of the second polarizing beam splitter (PBS) of the optical isolator behind this diode laser. We adjust the AOM frequency such that the injection locked laser diode operates at an optical frequency suitable for magneto-optic trapping ($\delta \approx -1.5\,\Gamma$ with respect to the $F = 2 \rightarrow F' = 3$ transition of the D_2 line) or for polarization-gradient cooling ($\delta \approx -10\,\Gamma$ with respect to the same transition). The final power of the beam can be reduced by the combination of an electro-optic modulator with a PBS. This combination has an extinction ratio of $\sim 10^{-3}$. To fully extinguish the beam a mechanical shutter is used. Just as mentioned before, it
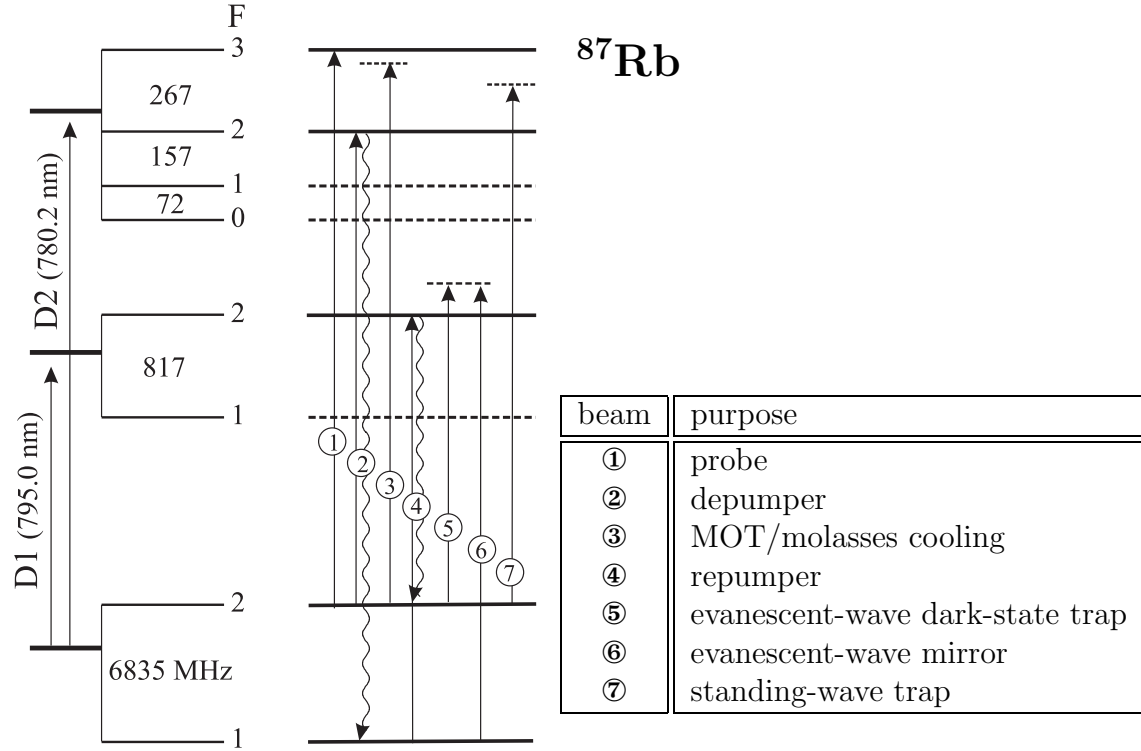
Figure 4.1: Overview of the laser frequencies used in the experiment.

is placed in the focus of a 1:1 telescope in order to reduce the switching time. The beam is finally injected into a SM optical fiber.

Initially we used a 50 mW laser diode [89]. This concerns the experiments described in chapter 6. Typically 100 μW of frequency shifted light was necessary for injection locking. A maximum power of 17 mW was realised behind the SM fiber. The fiber output was collimated to a waist of 4 mm. The beam is split in 3 parts. The 6 MOT beams were created by retro reflecting the original 3 beams. A disadvantage of this setup is that there is a power imbalance between the retro-reflected beams, both by the reflections from the glass cell surfaces and the absorption of the cloud of cold atoms, but it is very economical in terms of laser power.

In later experiments (chapter 7) the 50 mW diode was replaced by a 150 mW diode (*Semiconductor Laser International corporation*, SLI-CW-9mm-C1-783-0.15s-PD). Although this device was specified as SM, all tested specimen were multi mode, both spectrally and spatially. The spectral multi-mode behavior was removed by injection locking it with $\sim$ 3 mW of frequency shifted light from the master laser. The spatial multi-mode character limited the incoupling efficiency of the polarization maintaining (PM) fiber to $\sim$ 45%, which corresponds to $\sim$ 40 mW behind the fiber. This is sufficient to create 6 independent beams with a waist of 4.5 mm. This way the power imbalance between the beams is solved.

The MOT is loaded from the background ^{87}Rb pressure for 3 s. During the loading stage two coils in anti-Helmholtz configuration produce a magnetic field gradient of approximately 10 G/cm. The 6 MOT beams are circularly polarized, the beams that propagate perpendicular to the coil axis are orthogonally polarized
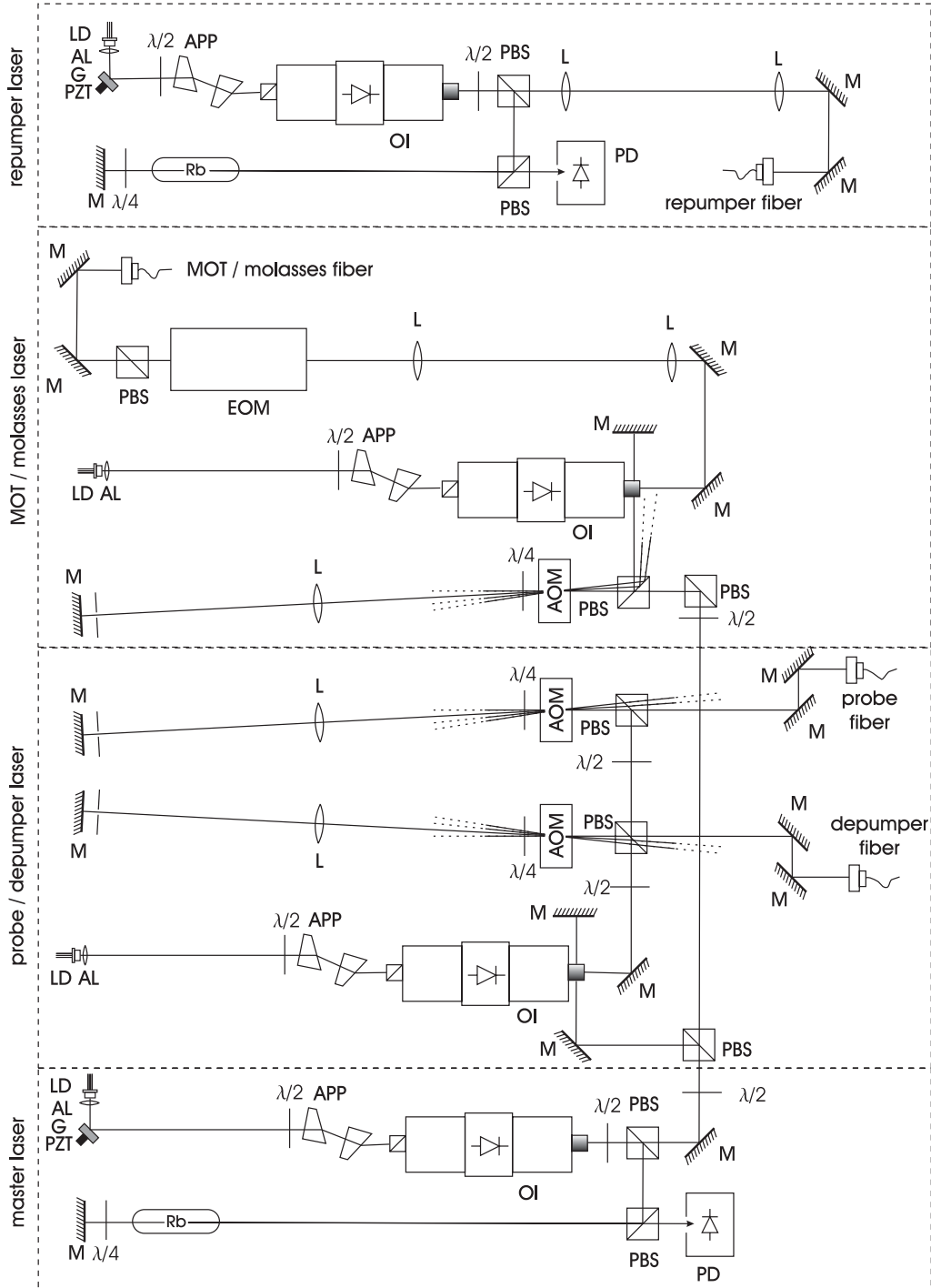
Figure 4.2: Schematic overview of the optical setup of the laser sections that operate near an atomic resonance, as discussed in the text. AL: aspheric lens, AOM: acousto-optic modulator, APP: anamorphic prism pair, BAL: broad area laser, BS: beam splitter, CL: cylinder lens, EOM: Electro-optic modulator, G: grating, $\lambda/2$: half-wave plate, $\lambda/4$: quarter-wave plate, L: lens, LD: laserdiode, M: mirror, OI: optical isolator, P: periscope, PBS: polarizing beam splitter, PD: photodiode, PZT: piezo transducer, Rb: cell with rubidium vapor.

from the beams that propagate parallel to the coil axis. The repumper light is overlapped with 2 of the 3 sets of counterpropagating MOT beams. When the MOT is saturated, the temperature of the trapped cloud of atoms is further decreased by a short period of 3 ms polarization-gradient cooling. During this stage the magnetic field coils are switched off, the detuning of the MOT light is increased to $\delta \approx -10\ \Gamma$ with respect to the $F = 2 \rightarrow F' = 3$ transition of the D_2 line and the power of the beams is decreased to approximately half the initial power by the EOM and PBS combination.

Typically 2×10^7 atoms were trapped and cooled to $T \approx 5\ \mu$K. In order to reach these low temperatures it proved very important to cancel all stray magnetic fields in the trapping region. This was done by three pairs of Helmholtz coils. After the molasses stage all light beams are switched off and the atoms fall ballistically towards the prism that is mounted inside the vacuum under the trapping region.

4.1.3 Probe and depumper

The *probe/depumper* laser diode is injection locked directly with light from the master laser. Its light is split in two beams and each is frequency shifted by a double-pass AOM setup and subsequently coupled into a SM fiber.

One of the beams is frequency shifted to the $F = 2 \rightarrow F' = 2$ transition of the D_2 line and is called the *depumper*. It will be totally internally reflected from one of the 45° surfaces of the prism that is mounted inside our vacuum system. The two prism configurations that are used are best visible in Figs. 4.5 and 4.7. This way the depumper beam will propagate vertically upwards, along the trajectory of cold atoms falling towards the surface. A short pulse of ~ 1 ms duration and a power of $100\ \mu$W is sufficient to pump all atoms to the $F = 1$ ground state by a spontaneous Raman process.

The second beam is frequency shifted close to the $F = 2 \rightarrow F' = 3$ transition of the D_2 line and will be called the *probe*. It is used for all probing purposes in the experiment: e.g. the evanescent-wave probing technique that will be discussed in chapter 6, but also for absorption imaging [89, 90, 96] in order to characterize the cloud of falling atoms.

4.1.4 Non-resonant lasers

Several higher power lasers are used in the experiments. These lasers are not frequency locked, since their detuning from an atomic resonance is relatively large and their frequency drift is sufficiently slow to be able to compensate manually.

We use a tapered amplifier system (*Toptica*, TA100) that is used to create a repulsive EW potential to load a standing-wave (SW) dipole trap in experiments described in chapter 6. The tapered amplifier gives powers up to 300 mW behind an optical isolator, but due to a bad spatial profile only approximately 100 mW is transferred through a SM optical fiber. In these experiments it is blue detuned by 0.2-1 GHz with respect to the $F = 1 \rightarrow F' = 2$ transition of the D_1 line.

The SW laser is a Ti:sapphire laser (*Coherent*, MBR-110) that is pumped by a 10 W Verdi laser (*Coherent*). This system gives up to 1.4 W of optical power near the D_2 line and is red detuned by 85 GHz in these experiments. In the experiments described in chapter 7 this Ti:sapphire laser is used for the EW dark-state trap, where it is tuned close to the D_1 line. This wavelength is closer to the optimum wavelength of the mirror set we use, which results in a power up to 1.8 W.

4.2   Evanescent wave alignment procedure

In order to accurately adjust the decay length of an evanescent wave, the angle of incidence of the incident beam must be carefully controlled. This is especially important for angles of incidence close to the critical angle, since the dependence of the decay length on the angle of incidence is very steep as is obvious from Eq. (2.19).

The setup with which we control the angle of incidence is depicted in Fig. 4.3. Two lenses L1 and L2, both with focal distance f, are separated by a distance $2f$. Also the distance from lens L2 to the top surface of prism P is $2f$. The lens L2 images the beam at the position of L1 on the prism surface. If the height of lens L1 is changed, the angle of incidence of the beam is changed, but its position on the prism surface remains unaltered.

The angle of incidence θ_i as a function of the lens displacement d is given by

$$\theta_i(d) = \frac{\pi}{4} + \arcsin\left(\frac{1}{n}\sin\left(\theta_0 - \arctan\frac{d-d_0}{f}\right)\right), \qquad (4.1)$$

with n the index of refraction of the prism and θ_0 an angle to compensate for the angle of mirror M. The term d_0 is the lens position for which $\theta_i(d_0) = \theta_c$.

In order to calibrate the lens position d_0, we need to describe the incident beam as a diffraction limited beam, as described in section 2.2. The transmitted power, light coupling out of the prism at grazing angles, is compared with a calculation based on Eqs. (2.29) and (4.1) for different positions of the micrometer on which
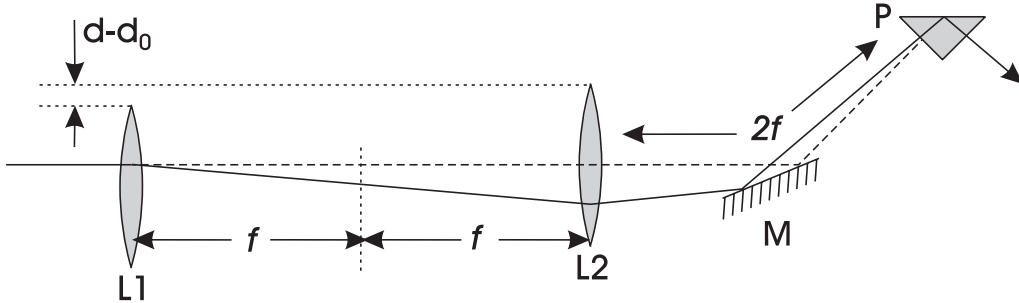

Figure 4.3: The setup used to control the angle of incidence. The distance between lenses L1 and L2 and between lens L2 and the top surface of the prism P is $2f$, with f the focal distance of the lenses. Lens L2 images the position L1 on the prism surface. If the height of lens L1 is changed, the angle of incidence of the beam is changed, but its position on the prism surface remains unaltered.
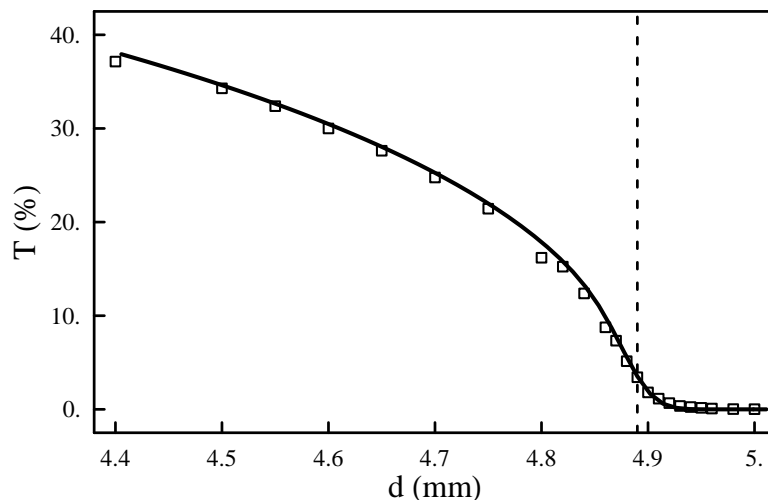
Figure 4.4: Measured ($\square$) and calculated (line) transmission versus the vertical position of the first lens as shown in Fig. 4.3 for a TE polarized beam with a waist $w = 500$ μm and lens focal distance $f = 80$ mm. The calculation is based on Eqs. (2.29) and (4.1). The angle of incidence θ_i of the beam is equal to the critical angle θ_c for a lens position of $d_0 = 4.89$ mm.

lens L1 is mounted. The result for a TE polarized beam with a waist $w = 500$ μm and lens focal distance $f = 80$ mm is shown in Fig. 4.4. From this it is clear that in this case $d_0 = 4.89$ mm. Note that only d_0 has been optimized and that no vertical scaling is applied. This method is very sensitive to alignment errors. If one of the lenses is not positioned accurately, or a lens is tilted, the shape of the graph is compressed or stretched in the horizontal direction.

The accuracy with which the lens height d can be adjusted is approximately 5 μm. The accuracy with which the lens position d_0 can be determined from the fit, as shown in Fig. 4.4 is approximately 10 μm. Combining this with Eq. (4.1), leads to a maximum value for the accuracy of the angle of 120 μrad. This is below the divergence angle of 500 μrad of a diffraction limited beam with an experimentally realistic diameter of 0.5 mm.

4.3 Vacuum setup

The experiments described in this thesis have been performed in two similar vacuum setups. The experiments described in chapter 6 are performed in a setup described extensively in [89]. Therefore this setup will be only briefly discussed in this section. The experiments described in chapter 7 are performed in a modified version of this setup. This setup will be discussed in more detail.

4.3.1 Setup for EW absorption experiments (chapter 6)

The main part of the vacuum setup is an uncoated glass vacuum cell with outside dimensions $42 \times 42 \times 130$ mm^3 and a wall thickness of 4 mm. It is glued to a stain-
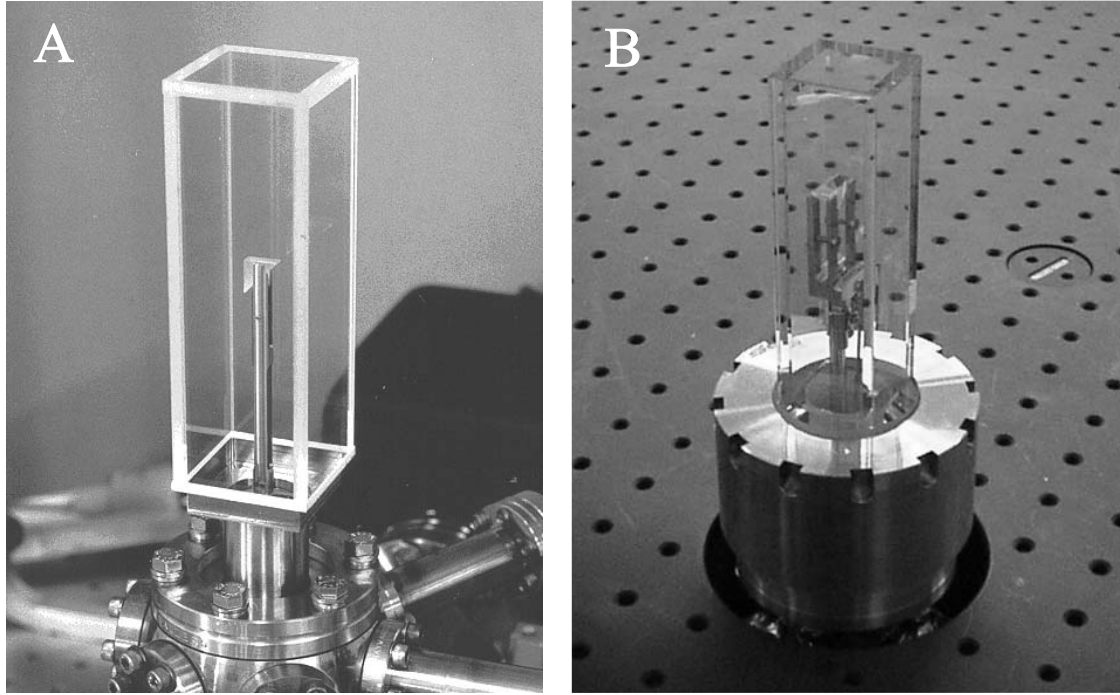
Figure 4.5: Cuvet and prism of the setup used in (a) chapter 6 and (b) chapter 7.

less steel platform, using low vapor pressure epoxy resin (*Varian*, TorrSeal). This platform is connected to a CF40 flange. This glued connection limits the bakeout temperature of the system to approximately 115 °C, which subsequently limits the achievable pressure in the system. This configuration provides us with excellent optical access for the numerous laser beams that are used in the experiments.

Inside this cuvet an uncoated BK7 glass prism, with dimensions $10 \times 10 \times 4$ mm^3 (*Melles Griot*, 01PRB009, cut in half) is mounted. Fig. 4.5(a) shows a picture of this prism mounted in the glass cell. The surface flatness is specified to be better then $\lambda/8$ at a wavelength of 632.8 nm, with a surface quality of 20-10 scratch-dig. The 45° face of this prism is used as the entry face for the beams that will create the evanescent fields, as discussed in section 4.2.

During the experiments a low pressure of Rb atoms is maintained in the cell. In order to get the Rb vapor into the system, a small oven containing a Rb reservoir is heated. This oven can be sealed off from the main vacuum by means of an UHV valve when the Rb pressure in the cell is sufficiently high. The vacuum is maintained by a continuously pumping ion pump with a pumping speed of 15 l/s (N$_2$). This creates a background pressure of 10^{-9} mbar. In order to prevent the Rb from being pumped away too quickly during the experiments, the cell is differentially pumped through an aperture with a diameter of 1.5 mm. This allowed for experiment runs up to several hours without a noticeable decrease of the Rb pressure.

4.3.2 Setup for EW trapping experiments (chapter 7)

The experiments described in chapter 7 are performed in a modified/ improved setup. An outline of this vacuum system is presented. The elements that are altered with respect to the setup described in [89] are discussed in more detail.

General vacuum setup   Drawings of the setup are shown in Fig. 4.6(a). The central part of the vacuum system is the "5-cross", all major components are connected to this cross. On the top port a hexagonal section (*Kimball physics*, spherical hexagon, MCF275-SH206C-B) and a cell, to provide optical access for the experiments, are mounted. The four side flanges of the "5-cross" will be discussed counter clockwise. One of the side ports is used for roughing the system. A turbo-molecular pump can be connected to this port in order to pump down from atmospheric pressure. It is usually sealed off by a UHV valve (*Granville Phillips*, gold seal type 204), so that the turbo-molecular pump can be detached from the system. To the second flange an ion pump (*Varian*, VacIon Plus20 StarCell with ferrite magnets, 15 l/s N_2) is connected. A "T-cross" is placed in between the "5-cross" and the ion pump to reduce the ion pumps magnetic field in the cell region. The ion pump can be sealed off by a gate valve (*VAT*, series 010 mini UHV gate valve DN40, manual actuator) so that the ion pump is not exposed to atmospheric pressure when the system is vented. The third flange on the "T-cross" is used for an ion gauge (*Varian*, Bayard-Alpert type UHV-24p). The third flange of the "5-cross" is closed with a blind flange, to be used in the future to connect a titanium sublimation pump. The last port is used for electric feedthroughs. Two 100 W halogen lamps are connected to this using wires of OFHC copper. They are carefully positioned in the centers of the "5-cross" and the "T-cross", as shown in the photograph in Fig. 4.6(c). There is also an electric feedthrough in the hexagonal section. A 100 W halogen lamp positioned in the center of the hexagon is connected to it. These lamps are used for baking the system from inside, instead of wrapping heater tapes around the setup.

Cell   The glass cell is replaced by a rectangular quartz cell (*Optiglass*, custom made) with outside dimensions $30 \times 30 \times 120$ mm^3 and a wall thickness of 4 mm. A "wide angle" anti-reflection coating for 780 nm is applied to the outside surfaces. It is shown in Fig. 4.5(b). An UHV vacuum tight connection between the cell and the stainless steel of the rest of the vacuum was obtained using a Helicoflex Δ gasket (*Le Carbonne-Lorraine*, type HNV200Δ (DN25), spring Nimonic 90, lining aluminium/Inconel600). This connection and a successful test are extensively described in [89]. The quartz cell is mounted on two rings of increasing diameter of the same material. The bottom surface of the lowest ring is polished. This construction is connected to a specially prepared stainless steel CF40 flange with a polished top surface and fine thread of 1.2 mm/turn on its outer surface. A Helicoflex Δ gasket is placed between the two polished surfaces. The system is subsequently compressed with a single compression nut screwed on the threads on the flange. This connection allowed for much higher baking temperatures than using the previously used glued cell. Pressures below 10^{-10} mbar are realized in this system.
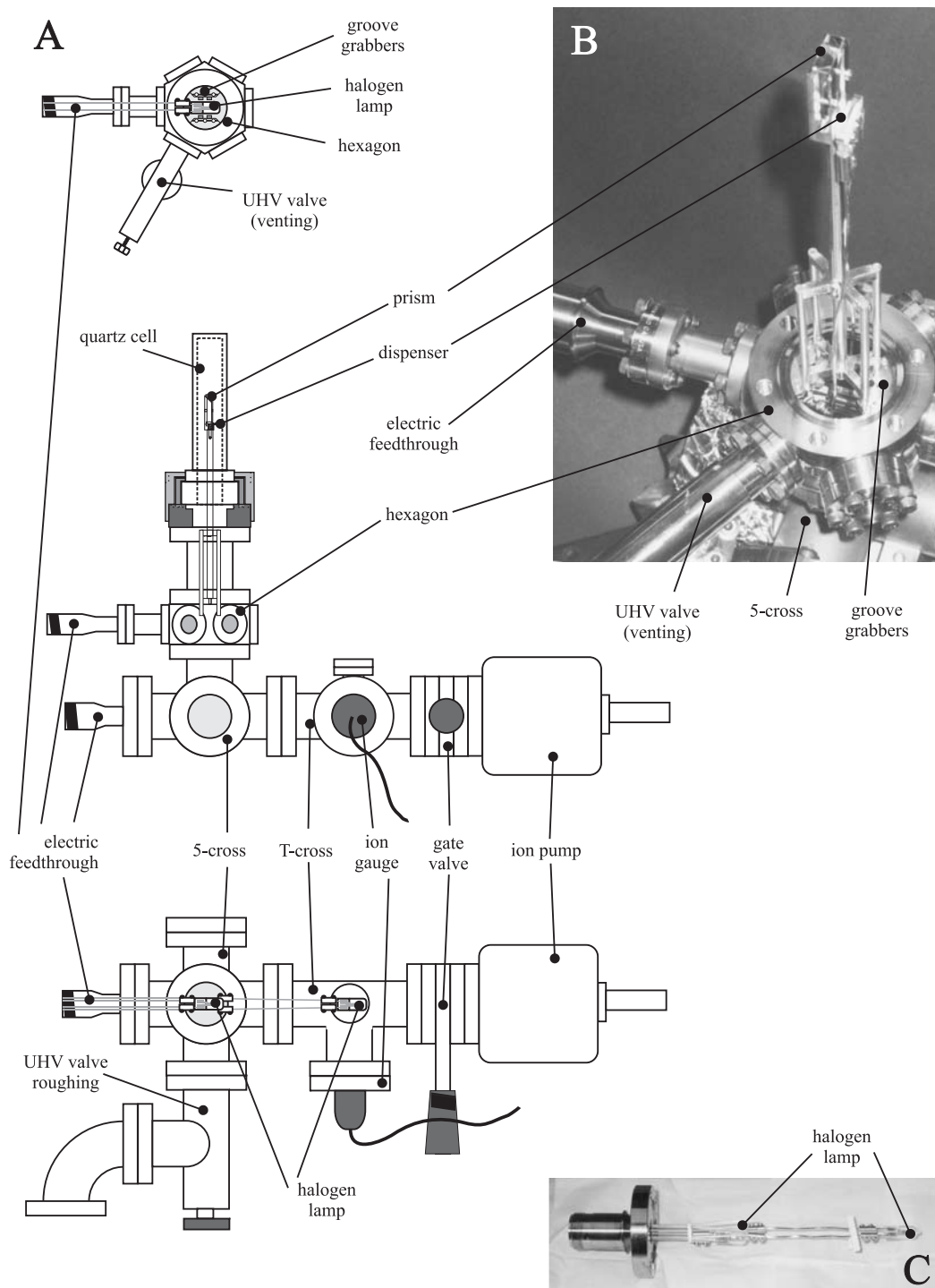
Figure 4.6: (a) Drawings of the vacuum setup; from top to bottom: top view of the hexagonal section, side view of the entire setup, top view of the bottom section around the "5-cross". (b) Photograph of the hexagonal section. It is visible how the dispenser is mounted against the prism mount and how this mount is itself mounted in the hexagonal section using "groove grabbers". (c) Photograph of the electric feedthrough in the "5-cross" on which two halogen lamps are mounted.
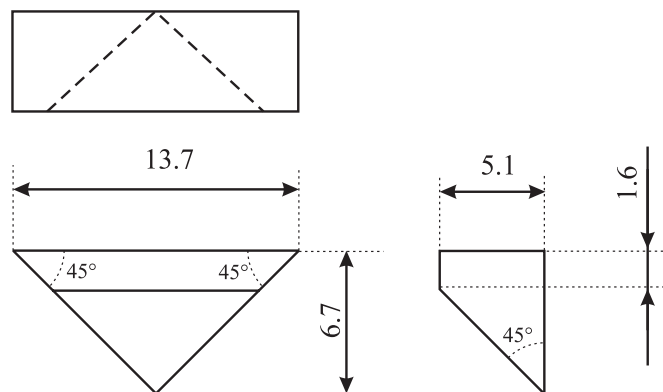
Figure 4.7: Top, front and side view of the prism used in the experiments described in chapter 7.

Prism The second major change is the geometry of the prism. Top and side views of this prism are shown in Fig. 4.7 and a photograph can be seen in Fig. 4.5(b). Although the shape of this structure does not resemble the geometrical shape of a prism, it will be called a prism throughout this chapter and chapter 7. It is effectively a pyramid that is cut in half and put upside down. The result is that it has three entrance faces at 45° with respect to the top surface, through which beams can enter that will totally internally reflect from the top surface and thus create evanescent waves "propagating" in different directions. The remaining entrance face, which is at 90° with respect to the top surface, can be used for a beam that will be internally reflected from the opposing 45° surface, which results in a beam propagating upwards through the top surface of the prism. The prism is created from the same basic rectangular prism (*Melles Griot*, 01PRB009) as the prism discussed in section 4.3.1. It is cut in half and an extra 45° face is grinded on one of the non-optical surfaces. Both the new 45° surface and the opposing 90° surface are subsequently polished. The resulting flatness of these surfaces is estimated to be λ. The prism is clamped at its four corners. Using a construction with several rods the prism is mounted using "groove grabbers" (*Kimball physics*, split axial clamping groove grabbers, MCF275-GG-CS03-A) in the hexagonal section. This is visible in the photograph in Fig. 4.6(b).

Dispenser The Rb oven is replaced by a Rb dispenser (*SAES getters*, RB/NF/ 3.4/12 FT 10+10). This is a small metal container that contains a mixture of rubidium chromates (Rb_2CrO_4) with a reducing agent. The narrow exit slit of the dispenser is partially obstructed by a metal wire to shield the escape of loose particles. By (resistively) heating it, the reduction reaction is initiated above a threshold temperature of about $\sim$400°C and the rubidium will be released. Dispensers were first mentioned as an atom source for laser-cooling experiments in [97]. A description of how to handle these dispensers more sophisticatedly in atomic physics experiments is discussed in [98]. Recently a method was described to reduce the background pressure while operating a dispenser by collecting the atoms that are too hot to be trapped on a thermo-electrically cooled copper plate [99].

We have mounted the dispenser in a small tray made of a ceramic material (MACOR, Al_2O_3), that is screwed against the prism mount. This is visible in the photograph of Fig. 4.6(b). The MOT loading region is blocked from the line of sight of the dispenser by the prism, so that hot atoms emerging from it do not collide with atoms trapped in the MOT. The dispenser is electrically connected to the electric feedthrough in the hexagonal section using OFHC copper wires. During the three seconds MOT loading process, a current of $\sim$6 A is run through the dispenser for the first two seconds. According to [98] the dispenser cools mainly by thermal radiation. During the short time that the current is switched off the temperature will not decrease significantly, so that the temperature will tend to a constant value, which results in a constant input rate of Rb atoms. During the experiments the pressure increased up to 5×10^{-10} mbar measured on the ion gauge. We switch the dispenser current off in order to get rid of the magnetic fields due to this current. This spurious magnetic field is especially important during the polarization-gradient cooling stage and the actual experiments.

5 Power-efficient frequency switching of a locked laser

We demonstrate a new and efficient laser-locking technique that enables making large frequency jumps while keeping the laser in lock. A diode laser is locked at a variable offset from a Doppler-free spectral feature of rubidium vapor. This is done by frequency shifting the laser before sending the light to a spectroscopy cell with an acousto-optic modulator (AOM). The frequency of the locked laser is switched quasi-instantaneously over much more than the width of the spectral features, i.e. the usual locking range. This is done by simultaneously switching the AOM frequency and applying feedforward to the laser current. The advantage of our technique is that power loss and beam walk caused by the AOM do not affect the main output beam, but only the small fraction of light used for the spectroscopy. The transient excursions of the laser frequency are only a few MHz and last approximately 0.2 ms, limited by the bandwidth of our locking electronics. We present equations that describe the transient behavior of the error signal and the laser frequency quantitatively. They are in good agreement with the measurements. The technique should be applicable to other types of lasers.*

5.1 Introduction

For the purpose of nowadays ubiquitous laser-cooling experiments [1, 3, 4] lasers are routinely locked to a Doppler-free absorption feature of an atomic transition. In a typical experimental time sequence one would first accumulate atoms into a magneto-optical trap (MOT) followed by a phase of e.g. polarization-gradient cooling. Both phases require different detunings of the laser light. The required switching of the frequency has been solved in several ways. However the existing solutions have some disadvantages, especially in terms of efficiency of laser power.

An existing and straightforward method is to lock the laser to a fixed detuning away from resonance and shift the laser frequency towards resonance by a variable amount, using an acousto-optic modulator (AOM). Usually the AOM is used in double-pass configuration to cancel beam walk associated with frequency shifting, resulting in a limited efficiency, typically lower than 65%. Moreover the beam walk compensation is imperfect.

Both the loss of laser power and the residual beam walk can be a problem when the light is used directly in an experiment, or when high-power multi-mode amplifier lasers are used, such as a broad-area laser (BAL) [101, 102] or a semiconductor tapered-amplifier laser (TA) [103]. With more seeding power such amplifiers perform better in terms of spectral purity and output power. Moreover they impose strict requirements on the beam pointing stability of the injection beam. The latter problem could be solved by first amplifying the light before frequency shifting it, providing the amplifier with sufficient power and a stably aligned injection beam. However power loss and beam walk now occur in the amplified beam.

Another solution is to injection lock [104, 105, 106] a second single-mode diode laser with the frequency shifted light, since this puts less stringent requirements on injection power and beam pointing stability. This injection-locked diode laser can subsequently be used to seed a BAL or TA laser [102]. A drawback is that this solution requires a significant amount of extra equipment. Furthermore, it is not possible to implement this solution in commercial BAL or TA systems without making major adjustments to the system, because the master laser is integrated in the system.

In this paper we demonstrate our method which is both efficient in its use of laser power and rigorously eliminates the beam walk due to the AOM frequency switching. We lock our laser using Doppler-free saturation spectroscopy in a vapor cell of rubidium. The laser is frequency shifted by an AOM before sending it through the spectroscopy cell. Thus, instead of shifting a fixed-frequency laser by a variable amount, we lock the laser at a variable frequency. This is only possible if the laser can follow the change in lock point associated with a change in the AOM frequency. This is a problem if the frequency jump is larger than the locking range set by the width of the Doppler-free features in the spectrum. We solved this by providing the laser with a feedforward signal, causing the laser to jump to within the locking range of the shifted lock point. We analyze the transient behavior of the laser frequency when making these jumps.
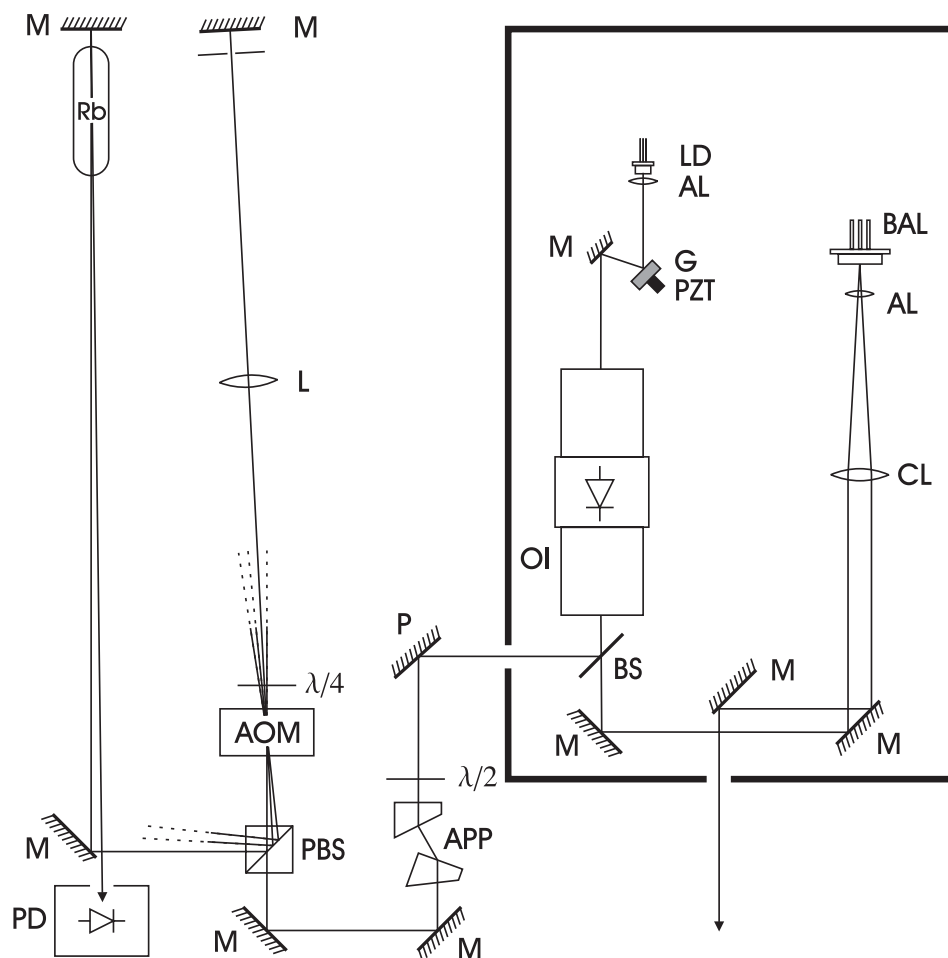
Figure 5.1: Schematic representation of the spectroscopy setup. The spectroscopy beam is sent through a double pass AOM setup to a saturated absorption section. This allows locking of the laser to an arbitrary frequency in the vicinity of an atomic transition. AL: aspheric lens, AOM: acousto-optic modulator, APP: anamorphic prism pair, BAL: broad area laser, BS: beam splitter, CL: cylinder lens, G: grating, L: lens, LD: laserdiode, M: mirror, OI: optical isolator, P: periscope, PBS: polarizing beam splitter, PD: photodiode, PZT: piezo transducer, Rb: cell with rubidium vapor.

5.2   Experimental implementation

In our experiment we work with ^{87}Rb which has a natural linewidth of $\Gamma/2\pi = 6$ MHz on the $5S_{1/2} \rightarrow 5P_{3/2}$ resonance line (D_2, 780 nm). The laser detunings needed for the MOT and the molasses phase are -1.5Γ and -10Γ with respect to the $F = 2 \rightarrow F' = 3$ component of the D_2 line. In view of the frequency range of our AOM we lock the spectroscopy beam to the $F = 2 \rightarrow F' = (1,3)$ cross-over. The detunings with respect to this transition are 203 MHz and 152 MHz, respectively. The desired frequency jump of ~ 50 MHz is thus much larger than the locking range of about $\Gamma/2\pi$.

We use a commercial laser system (*Toptica*, PDL100) consisting of an extended cavity diode laser [91, 92] in Littrow configuration [93], which injection locks a BAL.
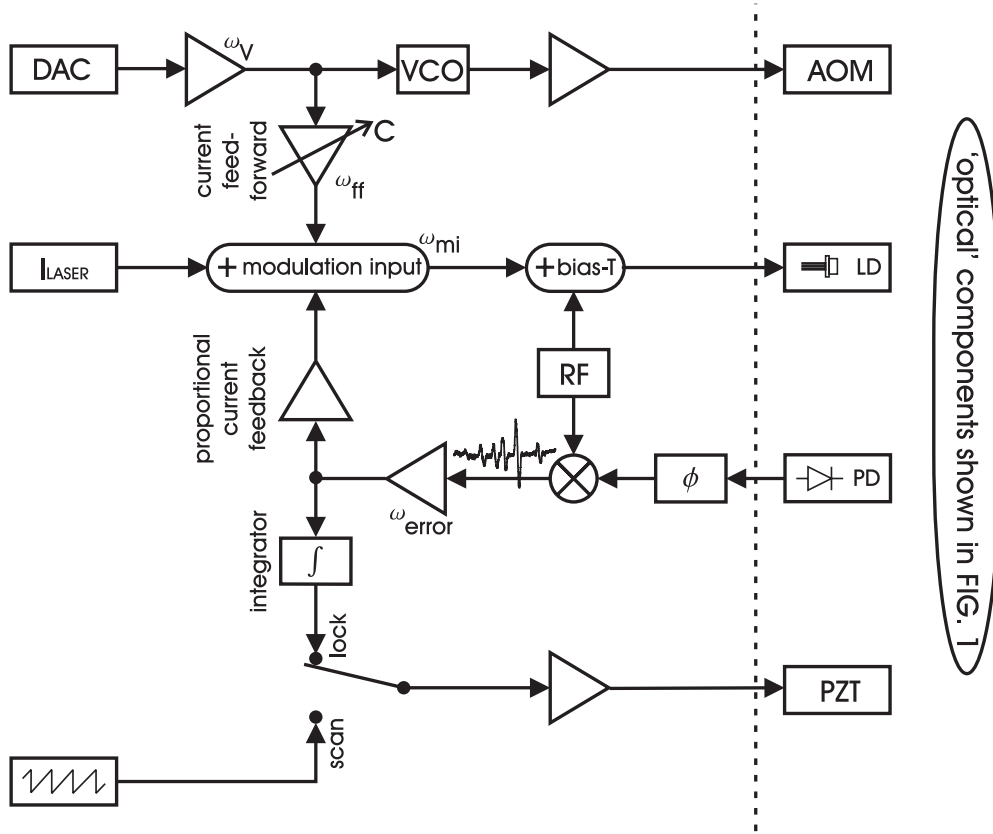
Figure 5.2: Schematic representation of the locking electronics. We employ FM spectroscopy to obtain a dispersive signal. This signal is used for integrational feedback to the PZT, and for proportional feedback to the laser current. The AOM frequency is generated by a VCO. The voltage driving the VCO is amplified and used as feedforward to the laser current in order to compensate the spectroscopy frequency for the frequency change of the AOM. On the left side of the dashed line the locking electronics is shown, on the right side the 'optical' components that can also be found in Fig. 5.1 are visible.

The grating of the extended cavity is mounted on a piezo stack (PZT) in order to scan the frequency. The setup is shown in Fig. 5.1. Behind the 60 dB optical isolator, 35 mW of power is left. The beam splitter reflects 10% to the spectroscopy setup. The spectroscopy beam first passes an anamorphic prism pair to circularize the elliptic beam shape. It then goes to a double pass AOM setup and finally to a Doppler-free spectroscopy section.

Fig. 5.2 shows a schematic representation of the electronics to lock the laser frequency. We employ FM spectroscopy [94, 95] to lock the laser. A small modulation with a radio frequency (RF) of 33 MHz is added to the laser current by means of a bias-T. The photodiode signal of the Doppler-free spectroscopy is phase shifted and mixed with the RF frequency resulting in a dispersive error signal, which is amplified with a measured bandwidth $\omega_{\mathrm{error}}/2\pi \approx 20$ kHz. This signal is integrated and sent to the PZT in order to lock the laser to a spectral feature. Proportional current feedback is also applied to suppress fast fluctuations of the laser frequency. The AOM frequency is generated by a voltage controlled oscillator (VCO). The voltage

driving the VCO is generated by a 12 bit digital to analog convertor (DAC), which is subsequently converted to the correct voltage range. This last step has a measured bandwidth $\omega_V/2\pi = 2.6$ kHz.

Fig. 5.3(a) shows FM spectra measured by scanning the PZT for two AOM detunings δ_{AOM}, which are close to the frequencies used in a typical lasercooling experiment: $\delta_0/2\pi = -186.2$ MHz and $(\delta_0 + \delta_1)/2\pi = -137.4$ MHz. The jump in frequency is clearly larger than the half-width of the dispersive features, so that the locking electronics will not be able to keep the laser locked to the same line when this frequency jump is made. When this shift is compensated by applying a feedforward jump to the laser current the spectroscopy beam will not change frequency and the laser will stay locked. Experimentally this is done by attenuating the voltage driving the VCO (measured bandwidth of the attenuator $\omega_{ff}/2\pi = 125$ kHz) and feeding this as feedforward to the modulation input of the current controller, which has a specified bandwidth $\omega_{mi}/2\pi = 100$ kHz. Ideally the frequency change due to feedforward δ_{ff} and the AOM detuning δ_{AOM} should cancel. In reality the two frequencies are only approximately equal:

$$\delta_{ff} = -C\delta_{AOM}, \tag{5.1}$$

with $C \approx 1$. The parameter C is coarsely adjusted to 1 by optimizing the overlap of the two spectra. The accuracy is limited by the noise on the curves. Spectra with C adjusted to 1 by this method are shown in Fig. 5.3(b). When using the feedforward on the laser current, we observe that the laser remains locked while jumping. In the next section the transient behavior of the error signal will be discussed. A more accurate method to optimize C will be demonstrated in section 5.4.

5.3   Analysis of transient behavior

In this section an equation will be derived describing the transient behavior of the error signal. When the laser is locked to a dispersive spectral feature and the frequency excursions are small with respect to the width of this feature, the error signal $e(t)$ can be approximated by

$$e(t) = A(\omega_S(t) - \omega_R), \tag{5.2}$$

with A the slope of the dispersive signal of the reference feature at frequency ω_R, which is equal to the $F = 2 \rightarrow F' = (1, 3)$ cross-over frequency in our experiment. The frequency $\omega_S(t)$ of the light in the spectroscopy section is given by

$$\omega_S(t) = \omega_L(t) + \delta_{AOM}(t), \tag{5.3}$$

where $\omega_L(t)$ is the laser frequency and $\delta_{AOM}(t)$ is the shift in the double-pass AOM section. In our experiment this is a step function

$$\delta_{AOM}(t) = \delta_0 + \delta_1 u(t), \tag{5.4}$$

with $\delta_0/2\pi = -186.2$ MHz, $\delta_1/2\pi = 48.8$ MHz and $u(t)$ the unit step function, so that the laser changes frequency at $t = 0$. Including all feedback and feedforward terms the laser frequency $\omega_{\mathrm{L}}(t)$ is given by

$$\omega_{\mathrm{L}}(t) = \omega_0 + \varphi e(t) + \alpha \int_{-\infty}^{t} e(\tau)\mathrm{d}\tau + \delta_{\mathrm{ff}}(t). \tag{5.5}$$

Here ω_0 is the frequency of the laser when it is not locked or any other electronic feedback is applied, the second term represents proportional current feedback. The third term is the integrational feedback to the PZT controlled grating. The last term is the feedforward to the laser current, which should instantaneously compensate the detuning jump by the AOM, as defined in Eq. (5.1).

When the laser is locked at $t = 0$, before the frequency jump, several terms cancel:

$$\omega_{\mathrm{L}}(0_-) = \omega_0 + \varphi e(0_-) + \alpha \int_{-\infty}^{0} e(\tau)\mathrm{d}\tau - C\delta_0 = \omega_{\mathrm{R}} - \delta_0. \tag{5.6}$$

Combining Eqs. (5.1)-(5.6) yields:

$$e(t) = A\left(\varphi e(t) + \alpha \int_{0}^{t} e(\tau)\mathrm{d}\tau + (1-C)\delta_1 u(t)\right) \tag{5.7}$$

from which the error function $e(t)$ after the frequency jump can be solved. As discussed in the previous section, several of the components have a limited bandwidth, which can be easily incorporated in the Laplace transform of Eq. (5.7), yielding

$$E(s) = \tau_{\mathrm{error}}(s)A \times \left[\left(\tau_{\mathrm{mi}}(s)\varphi + \frac{\alpha}{s}\right)E(s) + \tau_{\mathrm{V}}(s)\left(1 - \tau_{\mathrm{mi}}(s)\tau_{\mathrm{ff}}(s)C\right)\frac{\delta_1}{s}\right], \quad (5.8)$$

with $E(s)$ the Laplace transform of $e(t)$ and $\tau_{\mathrm{x}}(s) = 1/(1 + s/\omega_{\mathrm{x}})$ for x $\in$ {error, V, ff, mi} a (dimensionless) transfer function that describes the bandwidth of various components of the setup as shown in Fig. 5.2. Only the most limiting bandwidths are taken into account. The closed loop transfer function can be derived by solving $E(s)$ from Eq. (5.8). Subsequently the error function $e(t)$ can be derived from $E(s)$ by an inverse Laplace transformation. Although the solution $e(t)$ is analytical, it is not printed here, because it is too lengthy.

The frequency of the laser $\omega_{\mathrm{L}}(t)$ can be derived from the error function by combining the Laplace transforms of Eqs. (5.2), (5.3) and (5.4) and incorporating the bandwidth transfer functions $\tau_{\mathrm{x}}(s)$ as discussed previously. This yields for the laser frequency

$$\omega_{\mathrm{L}}(t) = \mathcal{L}^{-1}\left(\frac{E(s)}{\tau_{\mathrm{error}}(s)A} - \tau_{\mathrm{V}}(s)\frac{\delta_1}{s}\right) + \omega_{\mathrm{R}} - \delta_0, \tag{5.9}$$

where $\mathcal{L}^{-1}(\cdot)$ denotes an inverse Laplace transformation and the solution of Eq. (5.8) for $E(s)$ should be used for $E(s)$. Also Eq. (5.9) yields an analytical but lengthy solution, and is therefore not printed here. In the next section we will compare the calculated transients with the measured ones.
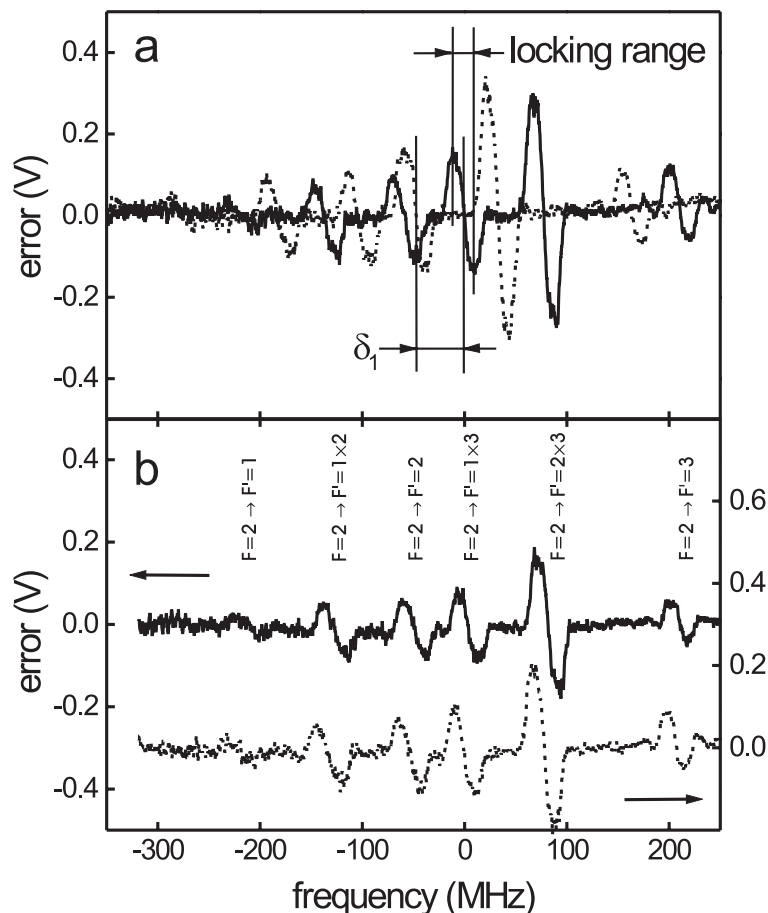
Figure 5.3: FM spectra, measured by scanning the PZT, for two different AOM detunings (a) without and (b) with current feedforward. It is clear that the frequency jump δ_1 is larger than the locking range, the width of the dispersive features. The laser will thus not stay locked to the $F = 2 \rightarrow F' = (1,3)$ cross-over when the AOM frequency is changed without current feedforward. Note that the curves in (b) have been displaced vertically relative to each other.

5.4 Comparison with experimental data

To lock the laser while the AOM frequency is switching, first the parameter C is coarsely adjusted by overlapping the spectra as described in section 5.2 (see also Fig. 5.3(b)). We then lock the laser to the desired zero crossing of the error signal by closing the feedback loop. While the laser is locked, the current feedback parameter φ is increased in order to decrease excursions of the error signal. The optimal value of φ is just below the value where the error signal starts to oscillate, in order to be as close as possible to critical damping. The top curve in Fig. 5.4(a) shows an error signal when the laser has been locked by this procedure and the frequency of the laser is changed from MOT to molasses frequency at $t = 0$. The error
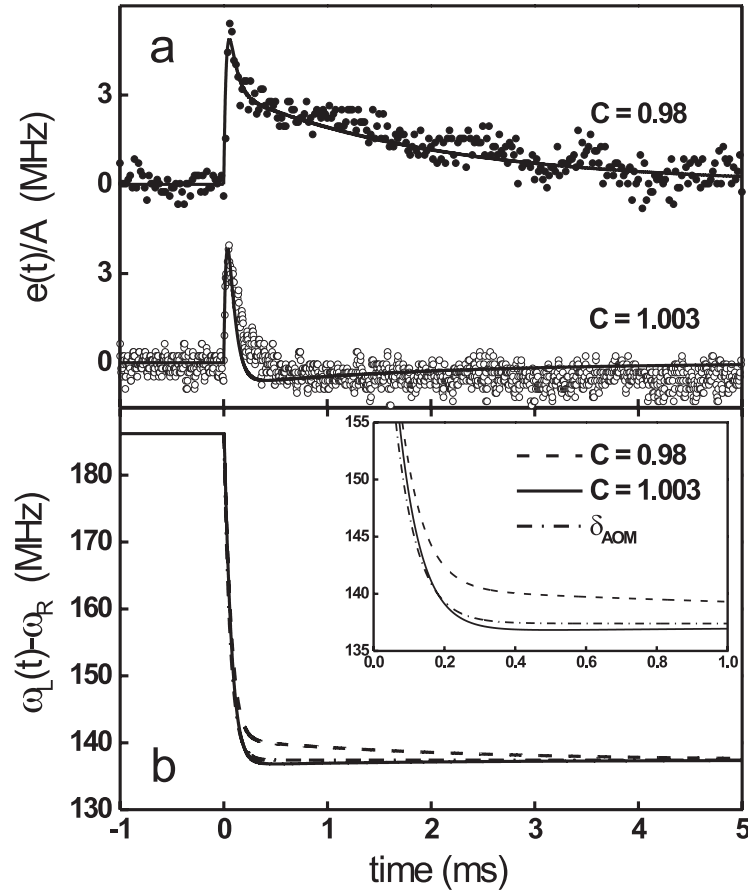
Figure 5.4: (a) Error signals versus time. At $t = 0$ the AOM and diode laser are switched from MOT detuning to molasses detuning. The top curve shows the error signal and a fit when the feedforward compensates 98% of the applied AOM shift, the bottom curve when the feedforward is 100.3% of the applied AOM shift. The solid line is the prediction of Eq. (5.8). (b) Laser frequency versus time for the above mentioned cases of current feedforward (solid and dashed), calculated using Eq. (5.9), and the frequency shift of the AOM (dash-dot), which is limited by the bandwidth of the step function ω_V. The inset shows the development of the laser frequency during the first millisecond in more detail.

signal is converted to a frequency by dividing it by the slope A of the dispersive signal. From this graph it is clear that in steady state the excursions of the laser frequency are approximately 1 MHz. One recognizes a fast increase of detuning due to the frequency shift of the AOM, followed by a decrease of frequency shift, because the current feedforward starts to compensate the AOM frequency shift. The current feedforward is slower than the AOM shift due to the bandwidths ω_{ff} and ω_{mi}. Finally a long tail due to the slow integrational feedback that removes the last amounts of the error signal is visible. It is clear that the current feedforward does not completely cancel the AOM detuning, resulting in a finite error signal that is

cancelled by the slow integrational feedback. By minimizing the amplitude of the error signal while the laser is locked and the AOM detuning is jumping, C can be optimized to a few permille. A curve with C optimized by using this method is shown in the bottom graph of Fig. 5.4(a). In order to determine values for C for both curves, fits to the data using the error signal $e(t)$ derived from Eq. (5.8) were performed. The results are shown as solid lines in Fig. 5.4(a). The bandwidths ω_x and the frequency δ_1 are kept constant to their measured or specified values. The slope of the dispersive signal A, the integrational feedback parameter α and the current feedback parameter φ are equal for the two curves. Their values are however not accurately known since they include e.g. the frequency response to the piezo voltage and the laser current. By repeating the fit procedure on both curves while iteratively varying A, α and φ, these values were optimized. Values for C are determined to be 0.98(1) and 1.003(5) after optimizing using the spectra and error signals respectively. It is clear that with the first method it is not possible to accurately get C equal to 1, while with the second method this is possible. For both cases the amplitude of the frequency excursion is smaller than Γ. We have successfully tested the technique for frequencies near the extrema of the bandwidth of the AOM. This range thus appears to be the limiting factor. The extent to which C has to be optimized when the frequency jump is changed depends on the linearity of the response of the VCO (AOM frequency) and the laser current on the applied voltage. In practice we had to finetune C slightly when the frequency jump was changed.

Fig. 5.4(b) shows the frequencies of the laser, calculated using Eq. (5.9) for the same parameters as for the two curves in Fig. 5.4(a). The frequency shift of only the AOM is also shown. From Fig. 5.4 it is clear that the error caused by the extra feedback loop is not severe for our application.

The main limiting parameters are the bandwidths ω_mi and ω_ff in the current feedforward path, which are not present in the electrical path to the AOM. In theory the amplitude of the frequency excursion can be decreased to 0 by better matching the bandwidths of the two paths, so that the detunings due the AOM and the current feedforward path always cancel. It would, of course, be more elegant if the bandwidth ω_V were larger, resulting in a shorter step-up time. However one should be careful with the bandwidths of the current feedforward path and the AOM path, since for constant but unequal bandwidths of these paths the amplitude of the frequency excursions will increase with ω_V.

5.5   Conclusions and outlook

We have demonstrated a new technique for locking a narrow linewidth laser to an arbitrary frequency in the vicinity of a spectral feature not by frequency shifting the output beam, but by frequency shifting the spectroscopy beam. By simultaneously switching the AOM frequency and the laser current it is possible to change the frequency of the laser by more than the locking range, while keeping it locked. Whereas the frequency shifting range in our experiment was limited by the frequency

range of the AOM, it should be possible to make even larger jumps by jumping to a different lock point. The transient frequency excursion was smaller than 5 MHz, less than the linewidth of the ^{87}Rb D_2 transition. The transient time was approximately 0.2 ms. The amplitude of the excursions was limited by the matching of the bandwidths of the electronics in the feedforward path and the AOM path. The duration of the transient was limited by the small bandwidth ω_V of the voltage driving the VCO and the current feedforward. The demonstrated technique is not restricted to diode lasers but should be applicable also to other types of laser, e.g. dye or Ti:Sapphire lasers.

---

* The technique described in this chapter has not been used in the experiments described in this thesis. However, it is presently being used to lock a Toptica TA100 tapered amplifier system, which is used as the MOT/molasses laser in the setup used for the experiments described in this thesis, and a Tiger laser from Sacher Lasertechnik in another setup in the group.

6 Cold trapped atoms detected with evanescent waves

We demonstrate the *in situ* detection of cold ^{87}Rb atoms near a dielectric surface using the absorption of a weak, resonant evanescent wave. We have used this technique in time of flight experiments determining the density of atoms falling on the surface. A quantitative understanding of the measured curve was obtained using a detailed calculation of the evanescent intensity distribution. We have also used it to detect atoms trapped near the surface in a standing-wave optical dipole potential. This trap was loaded by inelastic bouncing on a strong, repulsive evanescent potential. We estimate that we trap 1.5×10^4 atoms at a density 100 times higher than the falling atoms.

6.1   Introduction

Recently there has been increased interest in cold atoms trapped near a surface. For example magnetic fields of micro-electronic structures are used to trap and guide atoms near the surface of so called atom chips [107, 108, 109]. In 2001 Bose-Einstein condensation was realized on such a chip [38, 39]. Other examples are experiments aiming to increase the phase-space density and create a quasi 2D gas of atoms using inelastic reflections from an evanescent-wave (EW) atomic mirror [11, 20, 21].

These experiments pose new challenges for in situ detection, in particular if the atoms are within the order of an optical wavelength from the surface. In this case absorption of EWs is advantageous, since only atoms that are within a few wavelengths from the surface are probed. Aspect *et al.* have proposed the non-destructive detection of atoms close to a surface by detecting a phase change of a far detuned EW [14]. However this effect is very small and has not been observed so far. In this letter we demonstrate experimentally the absorption of resonant evanescent waves as a novel diagnostic tool to study cold atoms near a dielectric surface. Using a weak, resonant EW, we have studied a sample of cold atoms falling onto the surface as well as atoms trapped close to the surface.

EW absorption has previously been used for spectroscopy on hot and dense atomic vapors to experimentally investigate EW properties such as the Goos-Hänchen shift [110, 111].

6.2   Evanescent wave calculations

An evanescent wave appears when a light wave undergoes total internal reflection at the surface of a dielectric with index of refraction n. For a plane incident wave the optical field on the vacuum side of the surface decays exponentially $\sim \exp(-z/\xi)$ with z the direction perpendicular to the surface, $\xi(\theta) = \frac{\lambda}{2\pi}(n^2 \sin^2 \theta - 1)^{-1/2}$ the decay length, n the index of refraction of the substrate and θ the angle of incidence. For a low density of resonant absorbers near the surface, the scattering rate in the low saturation limit is proportional to the square of the field: $\sim \exp(-2z/\xi)$. If the density of absorbers is uniform, this gives rise to a total rate of scattered photons proportional to ξ. The scattered photons are missing from the reflected beam, which is therefore attenuated. If the angle of incidence approaches the critical angle $\theta_c = \arcsin(n^{-1})$, the value of ξ diverges, so the absorption becomes large. The absorption is however less height selective in this limit.

For a Gaussian beam with an angle of incidence $\theta_0 \gg \theta_c + \phi$ with θ_c the critical angle and ϕ the divergence of the beam, the electric field is similar to the field of a plane wave. For Gaussian beams with θ_0 closer to θ_c, the evanescent field does not decay as a simple exponential. We can describe the incident field as a superposition of plane wave Fourier components with various θ. Each component contributes an evanescent-field component with decay length $\xi(\theta)$ and an amplitude proportional to the complex Fresnel transmission coefficient $t(\theta)$. Because both $\xi(\theta)$ and $t(\theta)$ vary strongly around θ_c, the evanescent-wave contributions of these
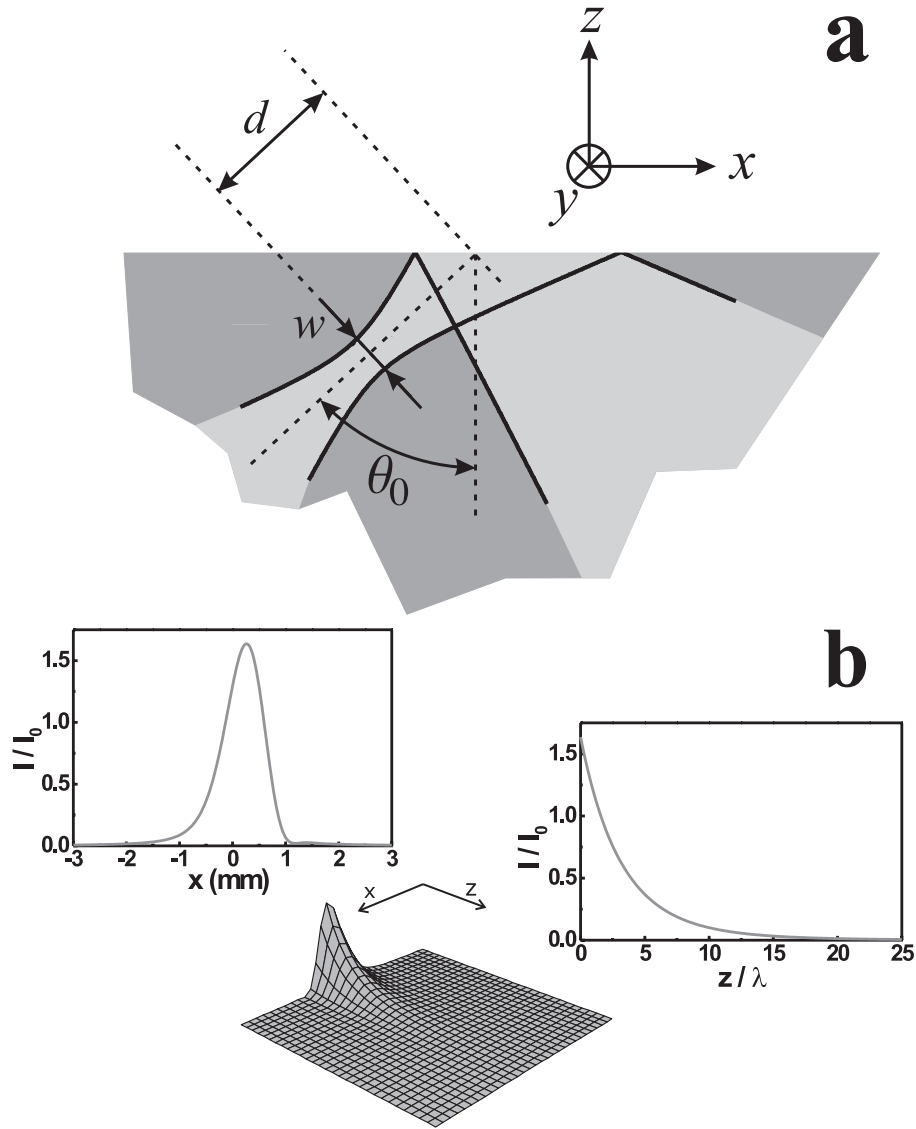
Figure 6.1: (a) Overview of the geometry and notations for the evanescent-wave calculations near the critical angle. The incident beam has a waist w and angle of incidence θ_0. The waist is at a distance d from the surface. (b) Intensity distribution of the evanescent wave for realistic experimental parameters $w = 330~\mu$m, $(\theta_0 - \theta_c) = 133~\mu$rad and $d = 680$ mm. Transverse x distribution at the prism surface, z distribution at the x coordinate where the intensity at the surface is highest.

incident plane wave components add up to a non-exponentially decaying field. In addition the transverse beam profile is modified to a non-Gaussian shape. In the reflected beam one of the effects is the well known Goos-Hänchen shift [112]. Other phenomena like non-specular reflection, shift of focus point and change of beam waist have been predicted [113]. They all result from combining a finite size beam with angle dependence of the transmission coefficient $t(\theta)$. Recently, it has been proposed to measure a Goos-Hänchen shift also in the evanescent wave using a

scanning tunnelling optical microscope (STOM) [114].

In the following calculations we will coherently add plane wave components with propagation vectors in the plane of incidence. The transverse distribution has been assumed Gaussian with the same radius as the incident beam at the surface. This approach is valid, since the transverse components of the propagation vector change the angle of incidence only in second order.

The evanescent field has been calculated by evaluating the following expression

$$E(x,z) = \frac{1}{\sqrt{\pi}\phi} \int_{\theta_c}^{\pi/2} t_{s,p}(\theta)p(\theta)e^{ik_x(\theta)x}e^{-z/\xi(\theta)}e^{ink_0d(\theta-\theta_0)^2/2}e^{-(\theta-\theta_0)^2/\phi^2}\,\mathrm{d}\theta, \qquad (6.1)$$

with $k_x(\theta) = nk_0\sin\theta$ the wavevector along the prism surface, $k_0 = 2\pi/\lambda$ and θ_0 is the angle of incidence. The first two exponents are the field distributions parallel and perpendicular to the surface, respectively. The third exponent takes into account that the waist of the incident beam is at a distance d from the surface. The fourth exponent is the distribution over angles of incidence for a Gaussian beam, with $\phi = 2/(nk_0w)$ the $1/e$ half width of the angle distribution of the field of a Gaussian beam with waist w. The factor $t_{s,p}(\theta)$ is the Fresnel transmission coefficient for transmission of a s or p polarized plane wave with angle of incidence θ from the dielectric into vacuum. They are given by $t_s(\theta) = 2n\cos\theta/(n\cos\theta + i\sqrt{n^2\sin^2\theta - 1})$ and $t_p(\theta) = 2n\cos\theta/(\cos\theta + in\sqrt{n^2\sin^2\theta - 1})$ respectively. Finally $p(\theta)$ is a normalization factor that is equal to 1 for s polarized incident light and $\sqrt{2n^2\sin^2\theta - 1}$ for p polarized light. The integration is carried out over the range of angles of incidence that generate an evanescent wave, from the critical angle θ_c to $\pi/2$. The normalization is chosen such that $|E|^2 = 1$ in the waist of the *incident* beam. The geometry of the problem and some of the parameters are displayed in Fig. 6.1(a). The effective evanescent intensity is given by

$$I(x,y,z) = \frac{1}{n}I_0\frac{w}{w_p}|E(x,z)|^2e^{-2y^2/w_p^2}, \qquad (6.2)$$

where I_0 is the intensity of the incident beam in the waist of the incident beam. The Gaussian determines the distribution in the y direction with w_p the transverse $1/e^2$ intensity radius at the prism surface. The fraction w/w_p corrects for the transverse divergence of the incident beam. This approach is possible since $|E|^2 = 1$ in the waist of the incident beam. Fig. 6.1(b) shows a calculation of the EW intensity distribution for realistic experimental parameters $(\theta_0 - \theta_c) = 133$ μrad, $w = 330$ μm and $d = 680$ mm. This distribution is used to calculate the absorption via the integrated scattering rate.

6.3   Time of flight experiments

In a first experiment we use evanescent-wave absorption to detect a cloud of cold atoms falling on a glass surface. Our setup consists of a right angle, uncoated, BK7

prism, mounted inside a vacuum cell with a background Rb pressure of $10^{-7} - 10^{-8}$ mbar. About 2×10^7 ^{87}Rb atoms are captured from the background gas in a magneto optical trap (MOT), located 7 mm above the prism surface and are subsequently cooled to 4.5 μK in optical molasses. They are released in the $F = 2$ hyperfine ground state and fall towards the prism due to gravity. Inside the prism a weak, resonant, p polarized probe beam undergoes total internal reflection. Its angle of incidence was determined with 100 μrad accuracy by a method that will be discussed later. The probe beam has a waist of 330 μm ($1/e^2$ radius) resulting in a divergence of 500 μrad inside the prism. At the prism surface it has a waist ($1/e^2$ intensity radius) of (470 ± 20) μm. The total power of the incident beam is $P_{\text{in}} = 2.2$ μW.

We measure the absorption in the reflected wave on a photodiode which is amplified by a factor 10^6 by a fast, low noise current amplifier (*Femto*, HCA-1M-1M). A typical absorption trace is shown in the inset of Fig. 6.1(a). The maximum absorption of time traces for different values of the angle of incidence are plotted in Fig. 6.2(a). From this graph it is clear that the absorption is highest for angles of incidence very close to the critical angle. In order to analyze these results we consider the atomic density to be uniform perpendicular to the surface, since the penetration of the EW (< 10 μm) is much smaller than the size of the cloud (~ 1 mm). It is crucial to take the finite probe beam diameter into account. This leads to a finite range of angles of incidence so that the EW is no longer exponential as described above. We define an effective decay length $\tilde{\xi}$ by $\tilde{\xi}/2 = \sqrt{\langle z^2 \rangle - \langle z \rangle^2}$ where the distribution function is the normalized intensity distribution $I(x_0, 0, z)/\int_0^\infty I(x_0, 0, z)\mathrm{d}z$ at the transverse position x_0 where the intensity at the surface is maximum. For a plane incident wave $\tilde{\xi} = \xi$. In Fig. 6.2(b) the solid squares represent the same absorption data as shown in Fig. 6.2(a), but plotted versus $\tilde{\xi}$. Absorption increases with $\tilde{\xi}$, but decreases beyond a value $\tilde{\xi} \approx 12\lambda$. This decrease for larger $\tilde{\xi}$ occurs because the amplitude of the EW quickly drops for angles of incidence θ_0 smaller than θ_c.

We compare our data to the absorption as calculated using two different approaches. The first method is to calculate the scattering of evanescent photons by the atoms near the surface, where we assume that the transmission coefficients are not changed by the atoms. The scattered power is calculated as

$$\frac{1}{2}\hbar\omega\Gamma \int_{\text{EW}} \rho(\mathbf{x}) \frac{s(\mathbf{x})}{s(\mathbf{x}) + 1}\mathrm{d}^3 x,$$

where $s(\mathbf{x}) = \frac{7}{15}I(\mathbf{x})/I_{\text{sat}}$ is the local saturation parameter, I_{sat} is the saturation intensity 1.6 mW/cm^2, $I(\mathbf{x})$ is the local evanescent intensity, given by Eq. (6.2), $\rho(\mathbf{x})$ is the local density, $\hbar\omega$ is the energy of a photon and $\Gamma = 2\pi \times 6$ MHz is the natural linewidth. The factor $\frac{7}{15}$ appears because linearly polarized light is used. The integration is over the entire volume of the evanescent wave. Because the absorption is so low, Beer's law remains in its linear regime. Obviously saturation effects are taken into account. We also account for the Van der Waals potential, which leads to a decrease in the atomic density close to the surface. Finally also the transverse density distribution of the atomic cloud is taken into account. Neglecting these last three effects would increase the calculated absorption by approximately 20%. The open circles in Fig. 6.2(b) are the results of this calculation for a density
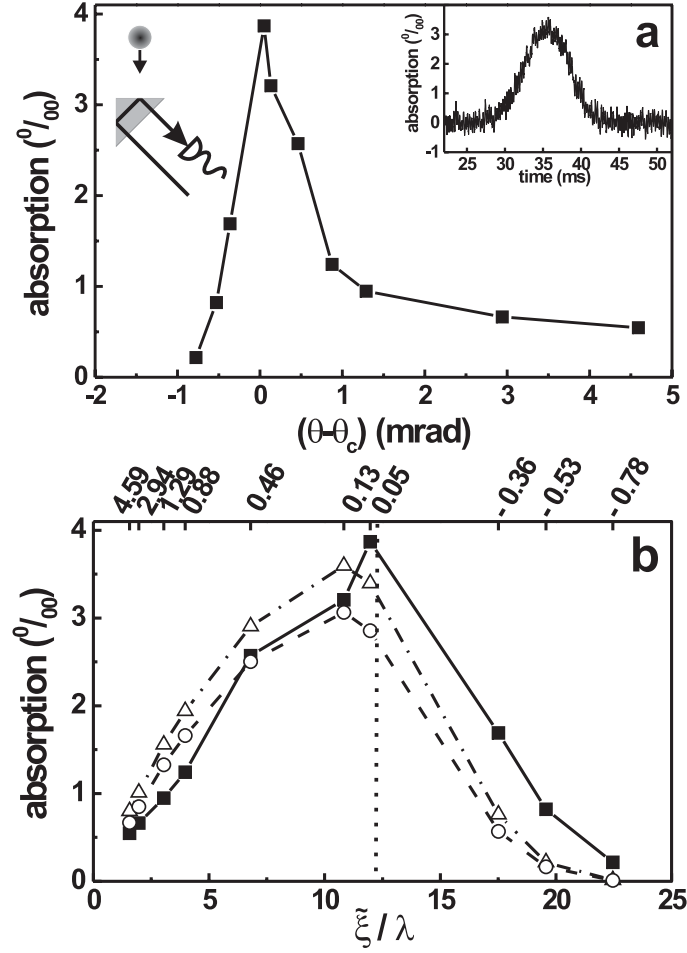
Figure 6.2: (a) measured absorption by a cloud of cold atoms falling onto a dielectric surface as a function of the angle of incidence of the evanescent probe beam. The inset shows a typical time of flight signal, measured with an angle of incidence of $(\theta_0 - \theta_c) = 130 \ \mu$rad. (b) same data as shown in (a), but versus effective decay length $\tilde{\xi}$. Also the results of the calculations based on a density of $1.2 \times 10^9 \ cm^{-3}$ are shown. ■ measured data, ○ calculated absorption on the basis of scattering, △ calculations using complex index of refraction. The vertical dotted line corresponds to the critical angle.

near the prism of $1.2 \times 10^9 \ cm^{-3}$.

For another measurement (not shown) with an angle of incidence $(\theta_0 - \theta_c) = 130$ μrad and an evanescent probe power of 2.9 μW, the measured maximum absorption of $(0.23 \pm 0.01)\%$ resulted in a calculated density of $(1.3 \pm 0.4) \times 10^9 \ cm^{-3}$. This value agrees very well with the density of $(1.3 \pm 0.2) \times 10^9 \ cm^{-3}$ derived from conventional absorption images with a CCD camera.

Close to a dielectric surface the radiative properties of atoms are altered [58]. The natural linewidth of a two-level atom can be up to 2.3 times larger than the natural linewidth in free space. However, including this effect in the calculations

only increased the calculated absorption by about 2%, which is well within the measurement uncertainty. By decreasing both the probe intensity and the decay length this effect should start to play a role.

As a cross check, the second method determines the absorption by describing the atomic cloud by a complex index of refraction $n = 1 + i\frac{\sigma_0\rho\lambda}{4\pi}$, with $\sigma_0 = \frac{7}{15}\frac{3\lambda^2}{2\pi}$ the resonant cross-section for linearly polarized light and ρ the density at the prism surface. Using this index of refraction to calculate the reflected intensity also yields the absorption. The reflected field is determined by evaluating

$$E(x, z) = \frac{1}{\sqrt{\pi}\phi} \int\limits_0^{\pi/2} r_p(\theta, n) e^{ik_x(\theta)x} e^{-ik_z(\theta)z} e^{ink_0 d(\theta-\theta_0)^2/2} e^{-(\theta-\theta_0)^2/\phi^2} \mathrm{d}\theta, \qquad (6.3)$$

with $k_z(\theta) = nk_0\cos\theta$ the wavevector perpendicular to the surface and $r_p(\theta) = (\cos\theta - n\sqrt{1 - n^2\sin^2\theta})/(\cos\theta + n\sqrt{1 - n^2\sin^2\theta})$ is the Fresnel coefficient for reflection for p polarized light. The same normalization as for Eq. (6.1) was used. The reflected intensity is given by $I(x, z) = I_0|E(x, z)|^2$. Saturation effects are not included. Since finally only the total absorbed power is important, it is not necessary to incorporate the transverse distribution in these calculations. The open triangles in Fig. 6.2(b) show the results of these calculations for various angles of incidence. The absorption for a maximum density near the prism surface of 1.2×10^9 cm^{-3} calculated with the complex index of refraction is slightly higher than the absorption calculated from the scattering of evanescent photons, mainly because saturation effects were neglected.

6.4   Trapping

In a second experiment we used evanescent waves to detect atoms trapped close to the surface in a standing light field. We load and trap the atoms using the scheme as described in previous work [20]. Cold atoms are prepared as in the time of flight experiment. During their fall the atoms are optically pumped to the $F = 1$ hyperfine ground state. On the vacuum side of the prism surface a repulsive EW potential is created by total internal reflection of a 90 mW, TM polarized laser beam with a waist of 500 μm and blue detuned by 0.2-1 GHz with respect to the $F = 1 \leftrightarrow F' = 2$ transition of the D_1 line. This potential acts as a mirror for atoms. The decay length of the EW can be controlled by changing the angle of incidence of the laser beam [115]. By scattering EW photons, the atoms can make a spontaneous Raman transition to the $F = 2$ hyperfine ground state, for which the repulsive EW potential is lower. This results in a virtually complete loss of their gravitationally acquired kinetic energy [46].

The trapping laser is a linearly polarized, 1.3 W laser beam, red detuned by about 85 GHz with respect to the D_2 line. It is reflected from the vacuum side of the uncoated prism surface, creating a standing wave (SW) with a visibility of 0.38. The angle of incidence is nearly normal, 25 mrad. The spot size at the prism surface is 380 μm $\times$ 440 μm ($1/e^2$ radii). For atoms in the $F = 1$ hyperfine ground state
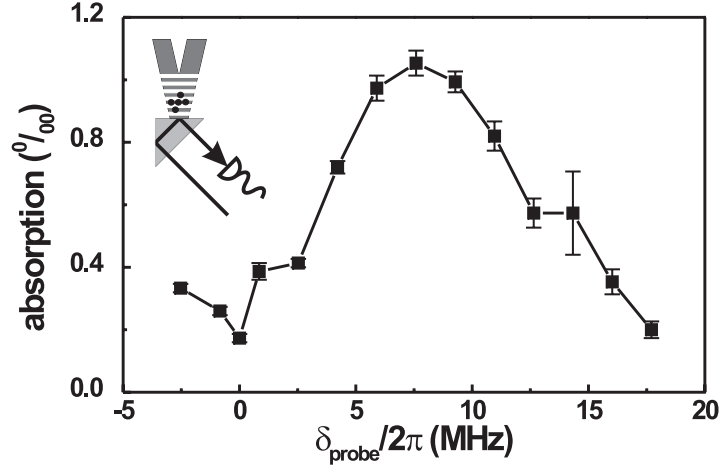
Figure 6.3: Measurement of atoms trapped in a standing wave, detected using evanescent probing. The absorption for different probe detunings shows that the atoms are distributed over several light shifts. We determine that 1.8×10^3 atoms are initially trapped.

the EW potential is dominant, whereas for the $F = 2$ hyperfine ground state the SW potential is dominant. Atoms that are Raman transferred to $F = 2$ near their motional turning point can be trapped in the SW potential. Only a few potential minima will be occupied due to the highly localized optical scattering of the EW. When the atoms fall towards the prism both the EW and the SW are off. Both are turned on 1 ms before the maximum atom density reaches the prism surface. In order to decrease the scattering rate, the EW is switched off after 2 ms, after which the loading of the SW trap stops.

The EW probe beam is aligned by overlapping it with the EW bouncer beam, whose angle can be set with an accuracy of 25 μrad. The overlap could be checked over a distance of 1.5 m, resulting in an uncertainty in the angle of 100 μrad. During the trapping experiments the probe angle of incidence was kept constant at $(\theta_0 - \theta_c) = 130$ μrad and the power of the probe beam is $P_{\rm in} = 2.2$ μW. At the prism surface it had a waist ($1/e^2$ intensity radius) of (770 ± 10) μm. The probe was resonant for atoms in the $F = 2$ hyperfine ground state and was turned on at least 14 ms after shutting the EW bouncer beam in order to be certain that no falling atoms were present and only trapped atoms would be probed.

Since the trap is red detuned, the atoms will be trapped in the intensity maxima. In the center of the trap the scattering rate in these maxima is calculated to be 7 ms^{-1} and the ground-state light shift is $\delta_{\rm LS}/2\pi = -15.4$ MHz. The trap depth here is only 8.6 MHz since the fringe visibility of the standing wave is 0.38. The trap frequency is 359 kHz, which results in approximately 24 bound levels. The resonance frequency of trapped atoms is blue shifted by $-2\delta_{\rm LS}$, due to the light shift of the excited state.

Fig. 6.3 shows the absorption of an evanescent probe beam by atoms trapped in

the standing wave. The evanescent-wave bouncer is blue detuned by 550 MHz and has a decay length $\xi = 1.15\ \lambda$. The evanescent probing technique was used to optimize the trap loading by varying the bouncer detuning. The maximum absorption is observed for a detuning of the EW probe of 8 MHz. The measured linewidth is larger than the 6 MHz atomic linewidth, probably due to inhomogeneous broadening. There are two contributions to the broadening. Firstly, since the trap laser has a Gaussian profile the atoms encounter a spatially varying light shift. Secondly atoms in higher excited vibrational states will encounter a smaller light shift. It is not possible to reliably retrieve these detailed distributions from our measured curve. It is however possible to make a good estimate of the total number of trapped atoms. The relative absorption curve in Fig. 6.3 is, for low saturation, described by

$$
\frac{-\delta P}{P} \;=\; \frac{\hbar\omega\Gamma}{P_{\mathrm{in}}} \int \int \frac{s(\mathbf{x})}{2}\,\frac{\tilde{\rho}(\mathbf{x},\Delta)}{1+4\left(\frac{\delta-\Delta}{\Gamma}\right)^2}\;\mathrm{d}^3\mathbf{x}\,\mathrm{d}\Delta,
\tag{6.4}
$$

which is similar to the scattering analysis of the falling atoms, but inhomogeneously broadened by means of the convolution with the Lorentz function. The factor P_{in} is the power of the incident probe beam and $\tilde{\rho}(\mathbf{x},\Delta)$ is the distribution of atoms in the $F = 2$ hyperfine ground state over spatial coordinates and light shifts. By integrating Eq. (6.4) over the detuning δ (the area under the curve of Fig. 6.3), the integration of the Lorentzian over δ yields $\pi\Gamma/2$. The integration over Δ, for which the integrand is now only $\tilde{\rho}(\mathbf{x},\Delta)$, yields the density of atoms $\rho(\mathbf{x})$.

From comparing the kinetic energy of the falling atoms in $F = 1$ to the trap depth when the atoms are pumped to $F = 2$, it follows that mainly the third and fourth potential minima will be populated. An underestimate of the number of atoms can be obtained by assuming the probe intensity constant over the trap region (which is valid if the evanescent probe size is much larger than the trap size) and all atoms are in the third minimum. Eq. (6.4) then reduces to $(\pi\hbar\omega\Gamma^2 s_3)/4P_{\mathrm{in}})N$, with N the total number of trapped atoms and where s_3 denotes the saturation parameter in the third potential minimum. From this a number of trapped atoms in the $F = 2$ hyperfine ground state of 3.0×10^3 can be calculated after 14 ms of trapping. The total number of trapped atoms will be 4.5×10^3 because the steady state $F = 1$ ground state population will be 0.5 times the $F = 2$ population due to scattering by the standing wave with the present detuning. The populations of the magnetic sub-levels of one hyperfine ground state are equal to within 1%. By comparison with previous measurements we deduce a life time of 14.3 ms. An extrapolation results in about 1.2×10^4 trapped atoms at $t = 0$. The assumption that the evanescent probe size is much larger than the trap size is not completely valid. Taking the correct radii into account leads to a 22% increase, thus 1.5×10^4 trapped atoms. Assuming the transverse trap distribution equal to the trapping laser, the vertical trap radius to be $\lambda/4$ and the atoms to be distributed mainly over two potential minima, the density becomes 1.2×10^{11} cm^{-3}, which is about 100 times higher than the density of the atoms falling onto the prism.

6.5   Conclusions and outlook

We have shown that the absorption of a weak, resonant evanescent wave can be used to selectively detect cold atoms near ($\sim \lambda$) a dielectric surface. A model treating the absorption by scattering evanescent photons was suitable to describe the absorption. When calculating the evanescent intensity distribution, the Gaussian character of the incident beam had to be taken into account in order to quantitatively understand the absorption for angles of incidence very close to the critical angle.

By detecting cold atoms falling onto the dielectric surface for different angles of incidence of the probe beam we have verified our quantitative description of the dependence of the absorption on the angle of incidence of the probe beam. By detecting cold atoms trapped in standing wave potential minima close to the surface we have determined that we have trapped more than 1.5×10^4 atoms initially. This results in an increase of the density of two orders of magnitude with respect to the approaching atoms.

The technique can be extended to using a CCD camera so that a transverse distribution of the atoms can be measured. By performing measurements for different angles of incidence of the probe beam, it should be possible to obtain information about the distribution of atoms perpendicular to the surface.

7 Analysis of an evanescent-wave dark-state trap

We present an implementation of an evanescent-wave dark-state trap. Various different geometries are discussed. In order to find a suitable set of experimental parameters, we have performed a numerical analysis of the loading procedure of the trap, in order to optimize the trapping fraction and the trap life time.

Within the experimentally accessible region of parameters, we found an optimum trapping fraction of 10% for atoms that fall onto a trap region. The trap depth for this result was 57 μK. A factor 130 density increase and a factor 75 phase space density increase are predicted with respect to values in a magneto-optic trap.

The main limitation of the dark-state trap is its sensitivity for photon scattering. An atom that scatters a photon almost certainly results in loss of the atom from the trap, since it will end up in an untrapped state. For atoms in the vibrational ground state this leads to an expected life time of 600 ms. However, for samples with realistic temperatures, the expected life time is decreased to few times 10 ms.

7.1   Low dimensional trapping

Ever since the experimental realization of Bose-Einstein condensation (BEC) [24, 25], and the Nobel prize for this achievement [33, 34], new quantum degenerate systems have been pursued. BEC has since then been realized for many atomic species [116], almost all alkali atoms, metastable noble gas atoms (He*), and rare earth atoms (Yb). Quantum degenerate Fermi gases have been realized [117, 118] and are presently at the threshold of the BCS regime [119], and there is strong evidence that this threshold has been crossed [120]. Furthermore condensates of molecules have been observed [35, 36, 37]. There are efforts for alternative, possibly easier, methods to reach BEC. Atoms are trapped in far off-resonant light field (QUESTS) instead of magnetic traps [40, 41]. Furthermore there is a trend to miniaturize the magnetic traps to current carrying wires mounted on a chip [38, 39], or using permanent magnetic thin films [121, 122]. There is still much interest in reaching the BEC threshold by means of dissipative optical laser-cooling techniques. The most promising results so far are for Cs [5] where a phase-space density (PSD) of 1/30 has been realized using Raman sideband cooling and Sr, where a sample of 4×10^4 atoms has been cooled to a PSD of 1/10 using Doppler cooling while the atoms where trapped in a FORT [6]. Still all realizations of BEC so far involve evaporative cooling.

Low dimensional quantum degenerate systems of bosons have very different quantum statistical properties than their 3D equivalents. In 2D a condensate only exists for $T = 0$, in 1D a condensate is absent at any temperature. The presence of a trapping potential, however, changes this situation. For a thorough analysis of such systems we refer to Petrov *et al.* [123, 124]. There are regions in parameter space, sufficiently low temperature T and large enough particle number N, for which a 2D condensate is formed. Only recently cold atom experiments have entered these regimes in 2D [43, 125] and 1D [125, 126]. For slightly higher temperature quasi-condensates are formed, where the phase coherence does not extend over the entire sample and "islands" of constant phase are present. For the 1D case, for very small N and T, the gas becomes a so called Tonks-Girardeau gas. The mutual repulsion between the bosons dominates the system, which prevents them to occupy the same position in space. This resembles fermionic behavior. A Tonks-Girardeau gas was recently realized by Paredes *et al.* [127].

For creating atom traps with lower dimensionality, evanescent waves have always received a lot of attention, either as the loading mechanism of a standing-wave (SW) trap, so that by scattering EW photons only one (or very few) fringes of the SW are loaded [15, 21, 22], or as the trapping potential itself. Examples of this are the gravito-optical surface trap (GOST) [11, 128, 129], or the red and blue detuned double EW trap (DEWT) [12], with which tighter confinement in the strongly confined direction can be realized. Rychtarik *et al.* [43] have created a two-dimensional BEC of Cs atoms, by trapping thermal atoms in a GOST, increasing the density using a dimple potential [44], and a subsequent evaporative cooling stage. Colombe *et al.* [42] are working towards loading a DEWT surface trap from a 3D ^{87}Rb BEC trapped in a magnetic trap. Hammes *et al.* [13] have already successfully
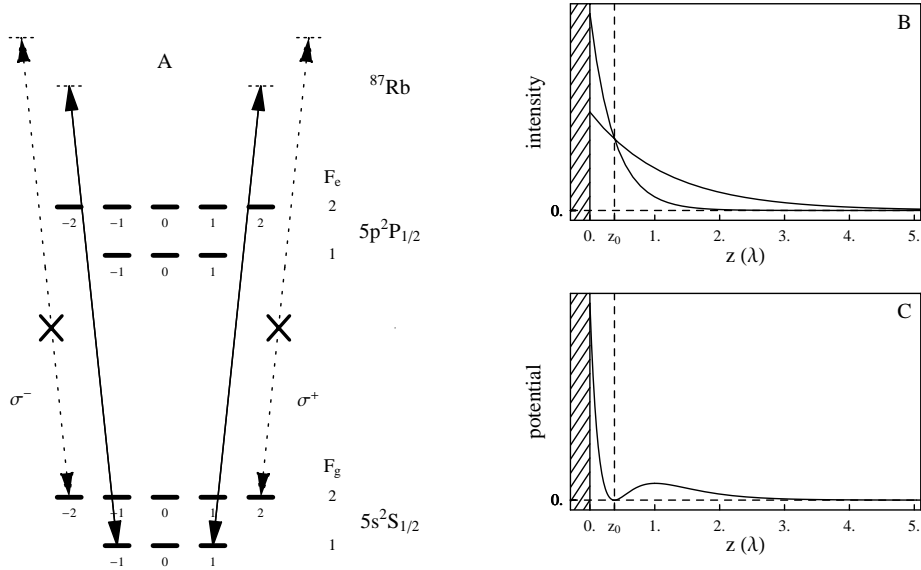
Figure 7.1: (a) Atoms in the $|F, m\rangle = |2, \pm 2\rangle$ ground state are decoupled from $\sigma^{\pm}$ polarized light (near) resonant with the D_1 line. A localized region of this polarization, blue detuned from the D_1 line is a confining potential for atoms in these states. (b) Two evanescent waves with different decay lengths have an equal intensity at a height z_0 above the surface. (c) When these evanescent waves have orthogonal polarizations, there are planes perpendicular to the surface where the phase difference between these two evanescent fields is $\pi/2$. The intersections of these vertical planes with the horizontal plane at height z_0 are lines of circular polarization, at which atoms can be confined.

demonstrated loading a DEWT trap from a GOST trap combined with a dimple potential, and trapped 20 000 Cs atoms at a temperature of 100 nK.

This chapter focuses on a combination of several of the above mentioned interests: a low-dimensional quantum degenerate system, created by dissipative optical techniques. It was proposed by Spreeuw *et al.* [20] and is an extension of [22], to make the latter proposal applicable to Rb atoms. The loading scheme is similar to the scheme described in the previous chapter and [15]. A sample of ^{87}Rb atoms in the $F = 1$ ground state is dropped on an evanescent-wave mirror [60] and is pumped to $F = 2$ by a spontaneous Raman process, during the reflection. This pumping is also performed by an evanescent field, which makes the pumping process highly localized. The pump field could be the same EW field that also creates the EW mirror, as in the previous chapter, but it could also be an extra, independent field. In [20] is shown that this process can increase the phase-space density up to three orders of magnitude compared with the MOT.

In the experiment described in the previous chapter, the atoms were trapped in a red detuned standing-wave dipole trap after this pumping process, similar to the experiment performed by Gauck *et al.* [21], where Ar* atoms were used. These Ar* atoms have a disadvantage in that they are in a metastable state, so that they will suffer from Penning ionization. The advantage of Ar* atoms is that the states before and after the pumping process are well separated by 42 THz, so that they can be

addressed independently. This is not possible for ^{87}Rb atoms, since the ground-state hyperfine splitting is only 6.8 GHz. This small splitting limits the SW detuning to small red detunings with respect to the $F = 2$ state, so that the $F = 1$ potential is not too strongly corrugated. Consequently, this small detuning led to a limited trap life time due to scattering of SW photons. An alternative could be the use of a blue detuned SW dipole trap. The atoms will then be trapped in the intensity minima, which results in a lower scattering rate. However, our loading scheme is not compatible with this option, since the atoms will be repelled by the blue detuned beams before they reach the trap region.

Spreeuw *et al.* [20] propose to trap atoms in a state that is locally decoupled from the light field. The only scattering that remains is due to the oscillation of the trapped particles into regions where they do interact with the light field. More specifically, ^{87}Rb atoms in the $|F = \pm m = 2\rangle$ ground-level sub-states are decoupled from a $\sigma^{\pm}$ polarized light field that is blue detuned from the D_1 line, as is shown in Fig. 7.1(a). By creating localized regions of blue detuned, circularly polarized light, atoms in the $|F = \pm m = 2\rangle$ sub-states will be repelled if they move out of these regions, they will thus be contained at these sites. These polarization structures are interference patterns of two orthogonally polarized evanescent waves. The same fields also act as the repulsive potential for atoms in the $F = 1$ state. A combination of a propagating or standing wave with an evanescent wave could lead to appropriate interference patterns, but atoms approaching the surface will be repelled by these non-evanescent fields.

The remainder of this chapter deals with the details of this trapping scheme. First the possible geometries and their implications will be discussed. Subsequently the "optimum" experimental parameters are determined from a numerical analysis in order to maximize the pumping to the trapped state, the life time and the trapping fraction. Some considerations are made about detecting the trapped atoms. Finally, the experimental issues that prevented us from performing the experiment will be discussed. We will end with conclusions.

7.2   Experimental configuration

The first part of this section deals with some initial choices for the EW dark-state trapping geometry. We will discuss several experimentally possible trapping geometries and the choice for a certain geometry will be explained. In the last part we will describe how this particular geometry is implemented experimentally. The fine tuning of the experimental parameters for this specific case will be dealt with in more detail in sections 7.3 and 7.4.

7.2.1   Double EW trapping geometries

In order to obtain a dark trap based on two evanescent waves, as described in section 7.1, the polarizations of the two evanescent fields should be orthogonal in order to avoid intensity fluctuations over the trap region. Furthermore the angles of incidence

$\theta_{1,2}$ of the two beams should be different, since this leads to different decay lengths $\xi_{1,2} = \kappa_{1,2}^{-1}$, with

$$\kappa_{1,2} = k_0\sqrt{n^2\sin^2\theta_{1,2} - 1}, \tag{7.1}$$

and different components of the $\mathbf{k}_\parallel$ vector along the surface

$$\left|\mathbf{k}_{\parallel;1,2}\right| = k_0 n \sin\theta_{1,2}, \tag{7.2}$$

as already discussed in section 2.1.3. In these equations $k_0 = 2\pi/\lambda_0$ is the free space wavevector, with λ_0 the wavelength of the light, and n is the refractive index of the dielectric. The different $\mathbf{k}_\parallel$ lead to a spatially varying phase difference between the two polarizations along the surface. There will be planes, perpendicular to the average $\mathbf{k}_\parallel$ vector and perpendicular to the surface, where the phase difference between the polarizations is $\pm\pi/2$, as e.g. shown in Fig. 7.2(b, d, f). The different decay lengths, together with appropriately chosen intensities of the two beams leads to equal intensities of the two polarizations at a certain distance z_0 from the surface, as shown in Fig. 7.1(b). We will preferably work with angles as close as possible to the critical angle, because, according to Eqs. (2.24) and (2.25), this leads to maximum evanescent-field amplitudes. The intersections of the horizontal plane at height z_0 and the vertical planes where the phase difference between the two EW components is $\pm\pi/2$, are lines of circular polarization, leading to a confining potential for the $|Fm\rangle = |2, \pm 2\rangle$ state, as shown in Fig. 7.1(c). In reality the Van der Waals coupling with the dielectric surface changes the potential.

When the angle between planes in which the incident beams propagate is changed the main change is the spacing between the lines of circular polarization. The following three cases are the most straightforward for our prism geometry, which is discussed in section 4.3.2:

(a) counterpropagating beams as shown in Fig. 7.2(a, d). The spacing between two lines of equal circular polarization is $2\pi/(k_{\parallel;1} + k_{\parallel;2}) \lesssim \lambda/2$. The spacing between two lines of opposite circular polarization is half this value. The polarizations of the input beams can be one TE and one TM polarized beam. Although a TM polarized input beam results in general in an elliptically polarized EW, this polarization is still orthogonal to the polarization of the TE polarized EW.

(b) planes of incidence at 90° as shown in Fig. 7.2(b, e). The spacing between two lines of equal circular polarization is $2\pi/(k_{\parallel;1}^2 + k_{\parallel;2}^2)^{1/2} \lesssim \lambda/\sqrt{2}$. The simplest option is for the two polarizations to be TE polarized. A combination of a TE and TM polarized input beam or two TM polarized input beams does not result in orthogonally polarized EWs.

(c) copropagating beams as shown in Fig. 7.2(c, f). The spacing between two lines of equal circular polarization is $\left|2\pi/(k_{\parallel;1} - k_{\parallel;2})\right| \gg \lambda$. The same remarks about the polarizations as for the counterpropagating beams apply.
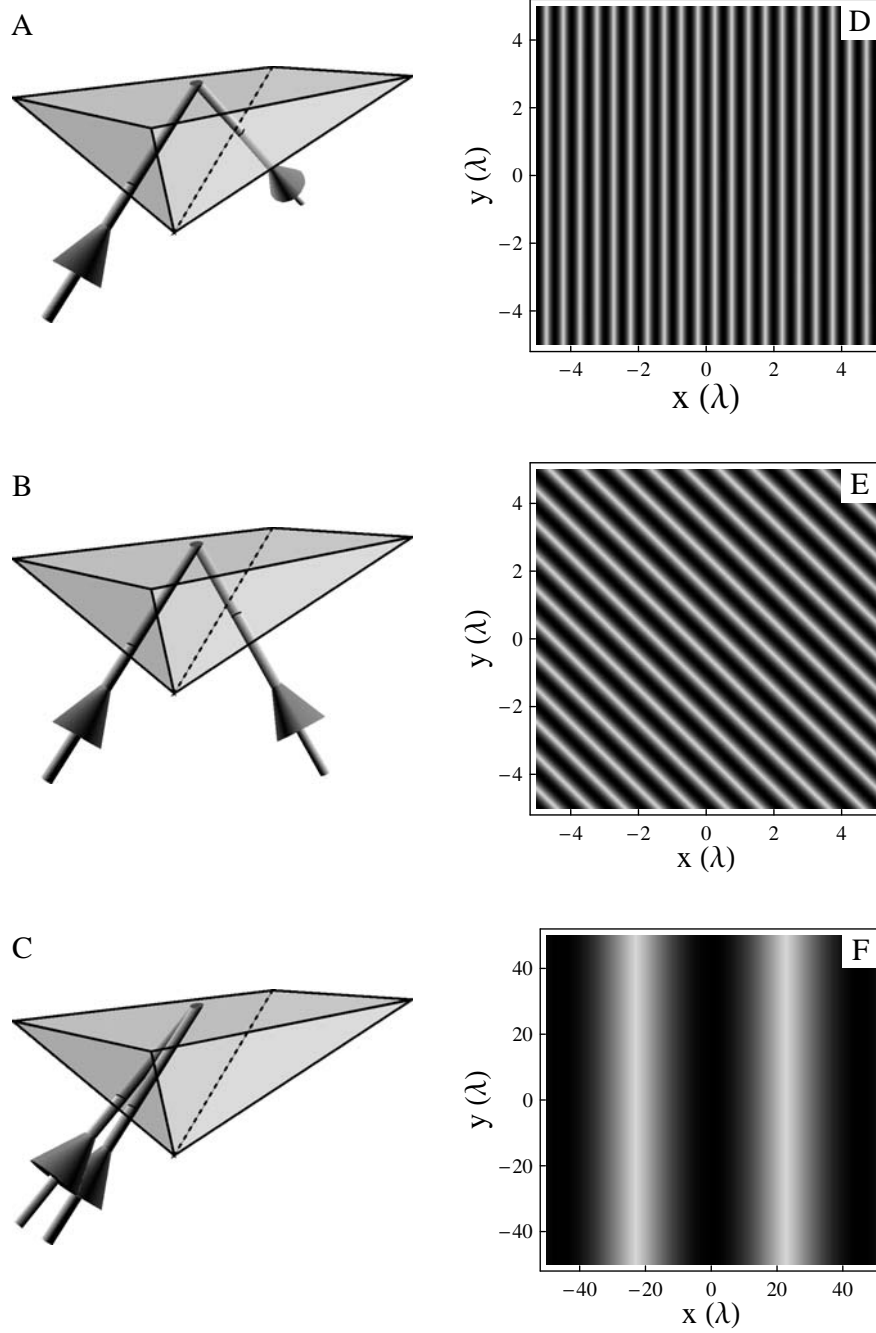
Figure 7.2: Schematic representation of (a) counterpropagating, (b) perpendicularly incident, and (c) copropagating beams. When the polarizations of the evanescent waves formed by these beams are perpendicular they form a phase pattern parallel to the surface with a periodicity of respectively (d) $\lesssim \lambda/2$, (e) $\lesssim \lambda/\sqrt{2}$, and (f) $\gg \lambda$ (notice the different scale). Figures (d), (e) and (f) are calculated using angles of incidence of $\theta_c + 2$ mrad and $\theta_c + 20$ mrad. Black and white lines indicate a phase difference of $\pm\pi/2$.

When atoms are trapped on these lines, they can be used as an atomic grating with an adjustable periodicity. This can e.g. be realized by changing the angles of incidence, which causes a slight variation of the periodicity, or by only loading one polarization set of the $\pm\pi/2$ polarized lines or both, which causes the periodicity to change a factor 2. The counterpropagating geometry is a candidate for a trap in which a Tonk's gas could be realized, due to its extremely elongated symmetry. Since initially our aim is to test these type of traps we have chosen the scheme with copropagating beams, since this is experimentally the easiest method to implement, as will be discussed in section 7.2.2. Moreover its scattering rate is lowest as will be discussed in section 7.4.2. The quantization axis in this geometry is roughly parallel to the $\mathbf{k}_\parallel$ vectors. It is slightly titled in the plane parallel to the surface, with the tilt depending on the angle of incidence of the TM polarized beam as discussed in section 2.1.5. For an angle of incidence of 20 mrad, this tilt angle is 12° as can be seen in Fig. 2.2.

7.2.2   Optical setup

For the EWs we use a Ti:Sapphire laser (*Coherent*, MBR-110) which is pumped by a 10 W Verdi laser (*Coherent*). It can produce up to 1.8 W at wavelengths close to the D_1 line. Due to losses in the optics, this leads to typically 1 W of power inside the vacuum. The frequency of the Ti:Sapphire laser is monitored with a Burleigh WA1500 wavemeter. The setup for the EWs is shown in Fig. 7.3: the two polarizations are separated using a polarizing beam splitter PBS1 and are recombined on a second polarizing beam splitter PBS2. The angles of incidence are independently adjusted with telescope setups such as described in section 4.2. The first lenses L1 and L1' (focal distance 80 mm) of these telescopes are between the two beam splitters. The two telescopes share the second lens L2, which is behind PBS2. Next the two beams are reflected towards the prism P using an elliptical silver mirror SM. By using this interferometer like setup the overlap of the two beams can be checked outside the vacuum. Before the first beam splitter PBS1, the power distribution between the two polarizations is adjusted with an electro-optic modulator and the beam is shaped with two achromat lenses. They are positioned such that the focus is on the first lenses L1 and L1' and it will thus be imaged on the prism surface. In the focus of this beam-shaping telescope a shutter is placed.

7.3   Pump field optimization

The transfer of atoms from the $F = 1$ ground state to the trappable $F = 2$ state is due to scattering photons either from the repelling EW or from a resonant EW that can be switched off after the trap is loaded. The first option requires a relatively low detuning of the trap and repellent fields, which results in a high scattering rate. Therefore we use an extra pumping field. Moreover this relaxes the criteria for the parameters of the trapping fields.

This section deals with optimizing the experimental parameters of the Raman
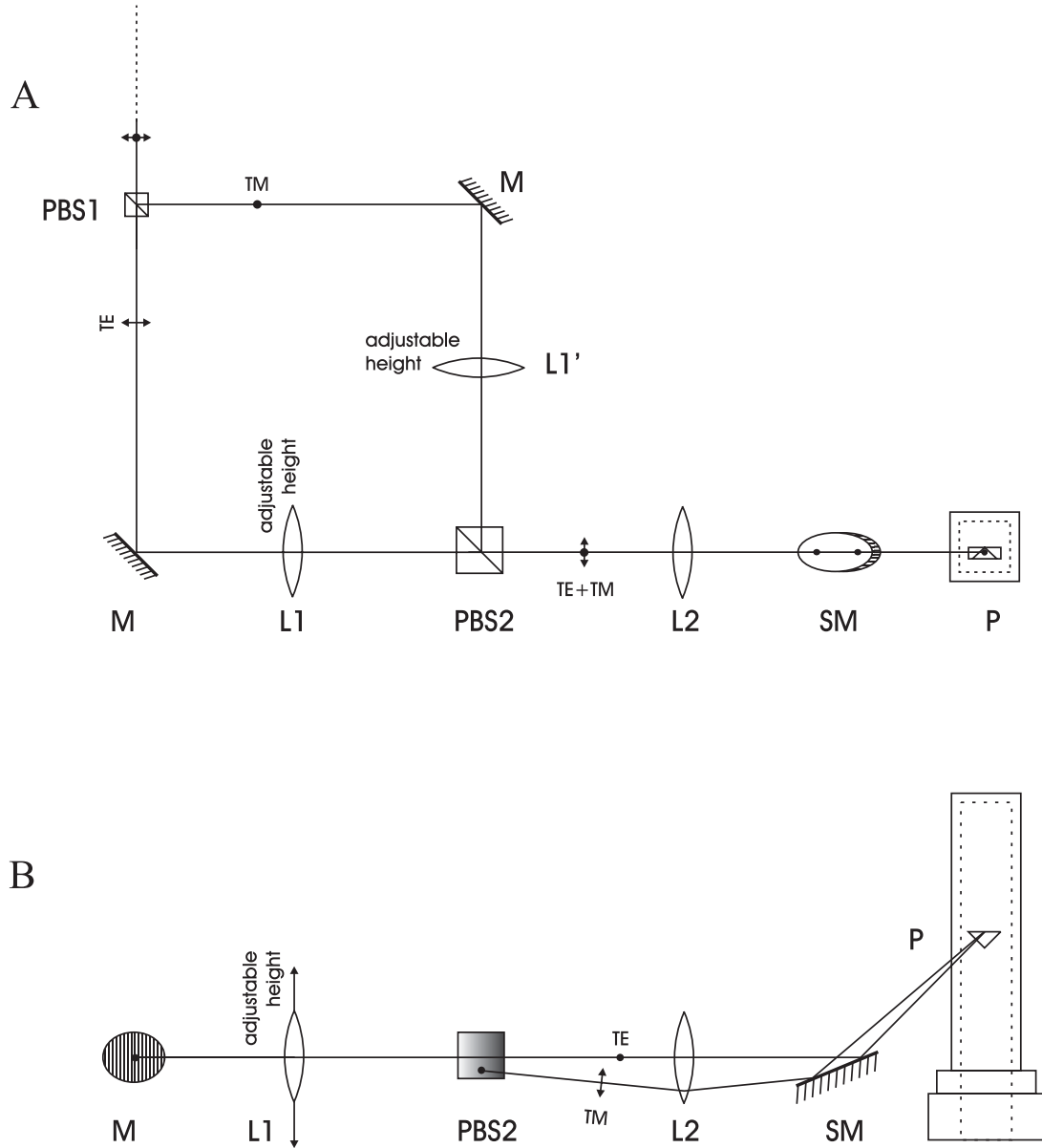
Figure 7.3: (a) top view and (b) side view of a schematic representation of the setup with which two evanescent waves with different decay lengths are created in the copropagating geometry. The two polarizations are split using a polarizing beam splitter PBS1 and are recombined with another polarizing beam splitter PBS2. Each of the arms passes a telescope with which the angle of incidence on the prism surface can be adjusted, as discussed in section 4.2. By moving the first lens (L1 or L1') up and down the angle of incidence of one of the beams is changed. Both arms share the second lens L2. (S)M: (silver) mirror, P: prism in cuvet.

pump beam. The parameters in question are the angle of incidence, i.e. the decay length of the evanescent field, the polarization and the intensity. Both theoretically optimal values and methods to obtain these in the experiment are presented. The first part focuses on finding the optimum polarization and frequency of the pump field. For our "copropagating" trap geometry we explain which alignment and polarization of the pump beam satisfies these conditions. In the second part a method is presented to optimize the pump beam intensity. It should not be too intense, since then all atoms will be pumped away before they reach the trap region, and not too weak, since then too few atoms will be pumped to the other state.

7.3.1 Pump field geometry and polarization

Table 7.1 shows the Raman transfer probabilities to a trapped state for the initial magnetic sub-levels $m_{F=1}$ of the $F = 1$ ground state. Values are given for the pump beam tuned to all possible excited states of both D lines and for several polarizations of the pump field. The numbers are the products of the probability of being excited to a state that can decay to the $|Fm\rangle = |2, \pm 2\rangle$ state and the probability to subsequently decay to the desired magnetic sub-state. They are calculated using the pumping efficiencies that are introduced in section 2.3.2 and are graphically depicted for the ^{87}Rb D lines in Fig. 2.4. For example we consider an atom initially in the $|1, 1\rangle$ state with the pump field resonant to the $F = 1 \rightarrow F' = 2$ transition of the D_1 line and polarized in an equal superposition of σ^+ and σ^-. The atom can be excited to both $|2, 0\rangle$ and $|2, 2\rangle$ with probabilities of $\frac{5}{35}$ and $\frac{30}{35}$ respectively. But only the latter excited state can decay to the $|2, 2\rangle$ ground state, with a probability of $\frac{20}{60}$. The pumping efficiency in this example is thus $\frac{30}{35}\frac{20}{60} = \frac{2}{7} \approx 0.286$.

The largest transfer probabilities obtained are for π ($\sigma^\pm$) polarized light on the $F = 1 \rightarrow F' = 1$ transition of the D_1 line, for atoms that are in the $|Fm\rangle = |1, \pm 1\rangle$ ($|Fm\rangle = |1, 0\rangle$) state. The major difference between the π and $\sigma^\pm$ polarized pumping field is that the former populates both the σ^+ and the σ^- polarized trap sites, whereas the latter populates only one of the two types of trap sites, depending on the polarization of the pump field. For an unpolarized incident sample of atoms it is possible to switch the periodicity of the atomic grating, formed by the lines of trapped atoms, by changing the polarization of the pump field.

In the remainder of this chapter we focus on loading the trap using a π polarized pump field, tuned to the $F = 1 \rightarrow F' = 1$ transition of the D_1 line. Besides the fact that it has the most efficient loading and that this polarization is easily created in the lab, it has an additional advantage. A trap site will only be loaded from one initial magnetic sub-state of the $F = 1$ ground state. Since the pump probability is different for each initial sub-state, this simplifies the optimization of the experimental trap parameters.

For our trap geometry with copropagating trapping beams, there is only one option to obtain a π polarized pump field. Only a TE polarized beam, incident (almost) perpendicular to the trapping beams, results in a π polarized pump field. As discussed in section 2.1.5 the quantization axis at the circularly polarized sites is rotated by a small angle χ with respect to the $\mathbf{k}_\parallel$ vectors. This angle depends
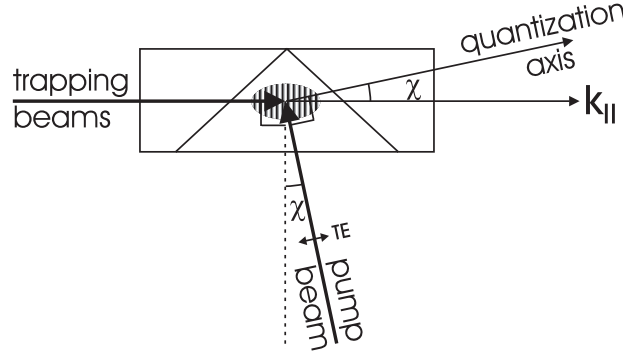
Figure 7.4: The plane of incidence of the TE polarized pump beam should be rotated slightly to compensate for the rotation of the quantization axis at the trap sites with respect to the $\mathbf{k}_{\parallel}$ vector.

excited state	final state $\lvert 2, m_{F=2} \rangle$	evanescent polarization $\sigma^+ \pm \sigma^-$ initial state $\lvert 1, m_{F=1} \rangle$			evanescent polarization π initial state $\lvert 1, m_{F=1} \rangle$		
		-1	0	1	-1	0	1
$5p\,{}^2P_{1/2}$ $F'=1$	-2	—	0.250	—	0.500	—	—
$F'=1$	$+2$	—	0.250	—	—	—	0.500
$F'=2$	-2	0.286	0.083	—	0.167	—	—
$F'=2$	$+2$	—	0.083	0.286	—	—	0.167
$5p\,{}^2P_{3/2}$ $F'=1$	-2	—	0.050	—	0.100	—	—
$F'=1$	$+2$	—	0.050	—	—	—	0.100
$F'=2$	-2	0.286	0.083	—	0.167	—	—
$F'=2$	$+2$	—	0.083	0.286	—	—	0.167

excited state	final state $\lvert 2, m_{F=2} \rangle$	evanescent polarization σ^+ initial state $\lvert 1, m_{F=1} \rangle$			evanescent polarization σ^- initial state $\lvert 1, m_{F=1} \rangle$		
		-1	0	1	-1	0	1
$5p\,{}^2P_{1/2}$ $F'=1$	-2	—	—	—	—	0.500	—
$F'=1$	$+2$	—	0.500	—	—	—	—
$F'=2$	-2	—	—	—	0.333	0.167	—
$F'=2$	$+2$	—	0.167	0.333	—	—	—
$5p\,{}^2P_{3/2}$ $F'=1$	-2	—	—	—	—	0.100	—
$F'=1$	$+2$	—	0.100	—	—	—	—
$F'=2$	-2	—	—	—	0.333	0.167	—
$F'=2$	$+2$	—	0.167	0.333	—	—	—

Table 7.1: Probabilities for an atom to end up from any of the magnetic sub-states of the $F=1$ ground state in a trappable state $\lvert 2, \pm 2 \rangle$ after making a spontaneous Raman transition induced by scattering a pump photon. The probabilities are given for several evanescent pump field polarizations and for the pump field to be resonant with all possible excited states of both the D_1 and the D_2 line.

on the angle of incidence of the TM polarized beam. The plane of incidence of the pump beam should be rotated over the same angle χ in order to be perpendicular to this quantization axis, as indicated in Fig. 7.4.

Beams with linear input polarizations that are incident from other directions lead in general to some superposition of σ^+ and σ^- polarization. A field with pure σ^+ or σ^- polarization is very difficult to realize, since it is not possible to measure whether the EW is circularly polarized. One thus has to calculate the necessary ellipticity of the incident beam, thereby relying on the knowledge of the Fresnel transmission coefficients of all the optics on its path. The same problem holds for any other polarization.

7.3.2 Pump field intensity and decay length

The repulsive potential for the $F = 1$ atoms is not an exponentially decaying function in space because it originates from two exponentially decaying potentials with different decay lengths and different polarizations. This makes also the polarization a function of the distance from the surface. We have to find a general, experimentally usable, solution to optimize the pump field decay length and the pump intensity, independent of the trajectory of the falling atoms. The decay length should be as short as possible, since this enhances the scattering close to the surface with respect to further away.

In the following analysis we will assume the atoms to be optically pumped to the magnetic sub-state from which the trapped state is loaded. In order to optimize the loading of the trappable states $|2, \pm 2\rangle$ the absolute scattering rate at the turning point of the atoms must be optimized. This depends on the remaining population n_1 of the magnetic sub-state that can be transferred to a trappable state and on the scattering rate. The trajectory of the falling atoms is given by $\zeta(t)$, with $\zeta(0) = z_0$ the turning point, which is determined by gravity and the repulsive potential. When an atom scatters a photon it has a probability p_1 to end up in its original state, a probability p_2 to end up in a trappable state, p_3 to end up in another magnetic sub-state of $F = 2$, and a probability p_4 to end up in another state of $F = 1$, with $p_1 + p_2 + p_3 + p_4 = 1$. The rate equation for n_1 is

$$\dot{n}_1(t) = (p_1 - 1)\eta(\zeta(t))n_1(t), \tag{7.3}$$

with $\eta(\zeta(t))$ the time dependent scattering rate the atom encounters. This can be derived from the local scattering rate $\eta(z)$, which in turn is proportional to the local pump intensity. This equation can be formally solved as

$$n_1(t) = n_1(t_0)e^{-\int_{t_0}^{t}(1-p_1)\eta(\zeta(\tau))\mathrm{d}\tau}. \tag{7.4}$$

Here $t_0 < 0$ is the time at which the atoms are released from the MOT.

The pump rate at the motional turning point $\eta(\zeta(0))n_1(0)$ can be maximized by optimizing the amplitude of $\eta(z)$. By substituting $\eta(z) = \eta_0\overline{\eta}(z)$ with $\overline{\eta}(\zeta(0)) = 1$ we have to optimize η_0 in order to maximize $\eta_0\overline{\eta}(\zeta(0))n_1(0)$. The solution of

$$\frac{\mathrm{d}}{\mathrm{d}\eta_0}\left(\eta_0\overline{\eta}(\zeta(0))n_1(t_0)e^{-\int_{t_0}^{0}(1-p_1)\eta_0\overline{\eta}(\zeta(\tau))\mathrm{d}\tau}\right) = 0 \tag{7.5}$$

satisfies this criterium. Here $n_1(0)$ has been evaluated using Eq. (7.4). Solving Eq. (7.5) yields

$$\int_{t_0}^{0} (1 - p_1)\eta_0 \overline{\eta}(\zeta(\tau)) \mathrm{d}\tau = 1, \tag{7.6}$$

i.e. the expectation number of the number of scattered photons that lead to the atom ending up in another than the initial state equals 1. This result is completely independent of the input trajectory and the distribution of the pumping field. After a full bounce the number of scattered photons will be twice this value, which leads to a final population of n_1 of $1/e^2$ of its original value $n_1(t_0)$.

This can be used to experimentally optimize the pump intensity. Using an absorption probe, which is resonant with the $F = 2 \rightarrow F' = 3$ transition, only atoms in $F = 2$ are detected. We can slightly adjust the trap parameters, which will be discussed in the next section, so that no trapping potential is present, and thus all atoms will bounce on the repulsive potential, but the scattering remains unchanged. The pump intensity can now be adjusted to optimize the fraction of atoms that is transferred to $F = 2$ during the bounce.

Depending on the specific pump transition, a certain fraction of the atoms that are pumped from the initial state will end up in the $F = 2$ ground state. For our chosen pump transition (π polarized pump field tuned to the $F = 1 \rightarrow F' = 1$ transition of the D_1 line) this fraction is $(p_2 + p_3)/(p_2 + p_3 + p_4) = \frac{50}{55}$. So after a full bounce a fraction $\frac{50}{55}(1 - \frac{1}{e^2}) \approx 78.6\%$ of the atoms should be in the $F = 2$ state at the optimal pump intensity. For an unpolarized initial sample of atoms an extra factor comes into play. In our case, atoms in the $|1, 0\rangle$ ground state are decoupled from the pump light and will not be pumped to the $F = 2$ ground state. The repulsive potential at a $\sigma^{\pm}$ trapping site, for atoms in the $|1, \mp 1\rangle$ state will typically be too low for the atoms to bounce, as is obvious from Fig. 7.5, and also these atoms will not contribute to the $F = 2$ population after a bounce. So only atoms which are initially in the $|1, \pm 1\rangle$ state at a $\sigma^{\pm}$ polarized trapping site will be pumped to $F = 2$. The fraction of atoms that should be transferred to the $F = 2$ ground state for an unpolarized sample should thus be approximately $\frac{1}{3} \times 78.6\% = 26.2\%$.

7.4   Optimization of trap parameters

In order to optimize the trap characteristics for a given laser power several parameters are at hand: the laser detuning δ, the beam waist w, the angles of incidence θ_{TE} and θ_{TM} of the two polarizations, and the distribution of the available power between the two polarizations. There are two quantities that have to be optimized: the scattering rate, which determines the life time of the trap, and the trapping fraction, which determines the initial number and density of trapped atoms.

The first part of this section explains some details about the potentials of these double EW geometries. These potentials are used subsequently to derive expressions for the scattering rate and the fraction of trapped atoms. Optimum values for the above mentioned experimental parameters will be derived by numerically optimizing the scattering rate in the trap and the trapping fraction by systematically changing

the experimental parameters. This is necessary since there is only a small window for the experimental parameters that yields a system in which atoms can be trapped.

7.4.1 Potentials

The potentials are calculated using the procedure described in section 2.3.2. Fig. 7.5 shows cross-sections of the potential curves of all the $F = 1$ and $F = 2$ ground states, through the center of a trap, one perpendicular to the surface and one parallel to the $\mathbf{k}_\parallel$ vectors and the surface. It is obvious from Fig. 7.5(a) that one of the $F = 2$ states has a local potential minimum at $z = z_0$. The potential at this minimum is smaller than 0 due to the Van der Waals attraction and the attractive potential due to far off-resonant coupling with the D_2 line. The steep decline of the potentials when $z = 0$ is approached is due to the Van der Waals attraction. The EW potential should be high enough near the surface to overcome the Van der Waals potential.

From Figs. 7.5(b, d) it is apparent that atoms that fall towards a trap region in the $F = 2$ potential fall on a potential maximum in the $F = 1$ state. They will thus be accelerated transversely, leading to a transverse displacement and an increase in kinetic energy. However, the displacement due to this acceleration is negligible with respect to the transverse period of the trap and the gained kinetic energy due to this acceleration is negligible with respect to the initial energy spread of the atoms. Both effects will be neglected in the following optimization procedure.

7.4.2 Life time

When the detuning from the D_1 line is small with respect to the fine-structure splitting between the D_1 and the D_2 line, the dominant contribution to the scattering rate is due to the atom moving out of the circularly polarized region. When the trap is approximated by an harmonic oscillator potential with energy levels $(\nu + \frac{1}{2})\hbar\omega$, with $\nu = 0, 1, 2, 3, \ldots$ and ω the harmonic trap frequency, the average potential energy U is half of this value due to the equipartition theorem. The average scattering rate is, according to Eq. (2.40), given by $\gamma = U\Gamma/(\hbar\delta)$, with δ the detuning with respect to the D_1 line. The scattering rate of atoms in the lowest vibrational state of a one dimensional harmonic oscillator is

$$\gamma_0 = \frac{\omega\Gamma}{4\delta}. \tag{7.7}$$

For an atom in the νth vibrationally excited state, the scattering rate is $2\nu + 1$ times higher. The trap frequency ω in the z direction, perpendicular to the surface, is much larger than in the other two directions. It will therefore dominate the trap loss, which justifies this one-dimensional oscillator approach. The scattering can be decreased by choosing a larger blue detuning, as long as it is small with respect to the D line fine-structure splitting.
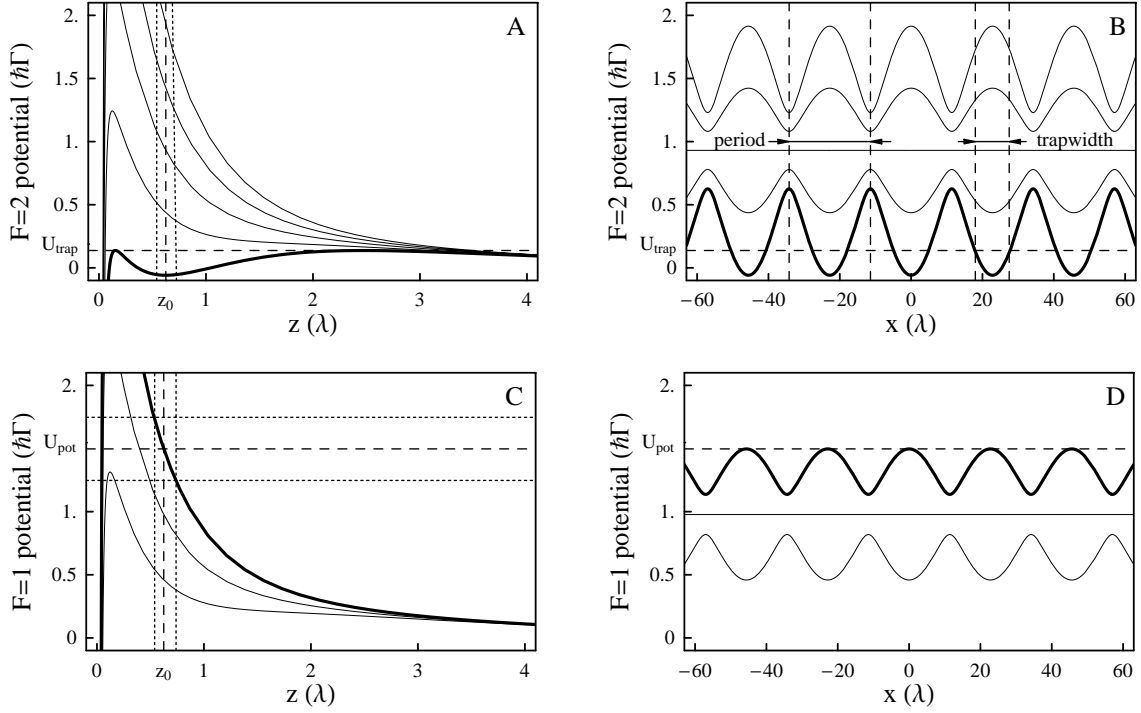
Figure 7.5: Cross sections of the potentials of all magnetic sub-states of the ground states of ^{87}Rb through the trap minimum. Shown are cross-sections for the $F = 2$ ground state, (a) perpendicular and (b) parallel to the $\mathbf{k}_{\parallel}$ vectors and the surface and cross-sections of the $F = 1$ ground state, (c) perpendicular and (d) parallel to the surface. The trapping potential for the $|2, \pm 2\rangle$ state and the repulsive potential for the state from which we load the trap $|1, \pm 1\rangle$ are drawn with a thick line. Note that the motional turning point of atoms incident on the $|1, \pm 1\rangle$ potential overlaps with the trap minimum. These potentials are calculated in the center of the evanescent field for the parameters $\theta_{\mathsf{TE}} = 450$ μrad, $\theta_{\mathsf{TM}} = 20$ mrad, 1 W total power, 300 μm beam waist, $\delta = 23.8 \times 10^3$ Γ and the fraction of power in the TE polarized beam is 27.4%,

7.4.3 Trapping fraction

The estimate of the realizable fraction of trapped atoms can be written as the product of two factors. The first, f_{x}, is the fraction of atoms that geometrically fall on an area with a confining potential. The second is the fraction of atoms that scatter a photon at the correct height in order to be transferred into the trap, which is denoted by f_{s}. This estimate is performed only for atoms with zero kinetic energy in the center of the original cloud of atoms. The energy spread due to the finite width and temperature is negligible with respect to the kinetic energy of the atoms when they arrive at the surface, and thus do not significantly influence the optimization of the parameters, as will be shown in the last part of section 7.4.4.

The geometric factor f_{x}, is estimated by the ratio of the trap width to the period of the trapping potential as depicted in Fig. 7.5(b). Here we take as the trap width the width of the regions where the potential is lower than the perpendicular trap

depth U_{trap},

$$f_{\text{x}} = \frac{\text{trap width}}{\text{period}}. \tag{7.8}$$

A typical number for $f_{\text{x}} \approx 0.5$. Note that in general the potential maxima parallel to the surface are larger than perpendicular to the surface.

The scattering factor f_{s} is determined by whether the atom scatters a photon at the correct height, so that it will be trapped. This will be determined by a classical and not a quantum-mechanical calculation, which will be justified in section 7.4.5. For an exponentially decaying pump field, the scattering rate at a certain height z above the surface is denoted $\eta(z)$. The pump field is normalized such that the criteria described in paragraph 7.3.2 are fulfilled. In these calculations we have chosen to have a relatively large angle of incidence $\theta_{\text{c}} + 4°$, which corresponds to a very small decay length of 0.4λ.

Since we chose a π polarized pump field tuned to the $F = 1 \to F' = 1$ transition of the D_1 line we only need to consider 2 potentials, as discussed in paragraph 7.3.1. The potential $U_{|1,\pm 1\rangle}$ is the repulsive potential encountered by the falling atoms in the $F = 1$ ground state and $U_{|2,\pm 2\rangle}$ is the trapping potential for atoms in the $F = 2$ ground state, depicted by the thick curves in Figs. 7.5(c) and 7.5(a) respectively. Whether the plus or the minus signs apply depends on whether a σ^+ or a σ^- polarized trap site is considered; the potential shape is the same for both cases.

For each height z we can calculate the remaining energy $E(z)$ of an atom that ends up in the $|Fm\rangle = |2, \pm 2\rangle$ state

$$E(z) = mg\zeta(t_0) - U_{|1,\pm 1\rangle}(z) + U_{|2,\pm 2\rangle}(z), \tag{7.9}$$

with $mg\zeta(t_0)$ the initial potential energy of the atom, with m the mass of the atom, g the gravitational acceleration constant, and $\zeta(t_0)$ the initial height of the atoms above the surface. This energy should be smaller than the trap height U_{trap} in order for the particle to be trapped. When the turning point of the falling atoms is within the trapping region, there is a time t_1 for which $E(\zeta(t_1)) = U_{\text{trap}}$. For $-t_1 < t < t_1$, $U(\zeta(t)) < U_{\text{trap}}$ holds. The total trapping fraction can be calculated by integrating over the absolute scattering rate between times $-t_1$ and t_1. This integral has to be multiplied by two factors in order to yield the scattering contribution f_{s} to the trapping fraction in the center of the trap. The first is the probability that the excited state will decay to the trapped state, $p_2/(p_2 + p_3 + p_4)$ as discussed in section 7.3.2. This is equal to $\frac{30}{55}$ for our pump geometry. The second is a correction factor p_{p} to take into account whether a polarized or an unpolarized sample is considered, equal to $\frac{1}{3}$ in our case for an unpolarized sample of atoms. Both factors are already explained in section 7.3.1. The scattering contribution to the trapping fraction is thus

$$f_{\text{s}} = p_{\text{p}} \frac{p_2}{p_2 + p_3 + p_4} \int_{-t_1}^{t_1} n_1(\tau)\eta(\zeta(\tau))\mathrm{d}\tau. \tag{7.10}$$

The trapping fraction f_{s} determines the density increase of the trapped atoms with respect to the falling atoms, whereas f_{x} only influences the number of trapped
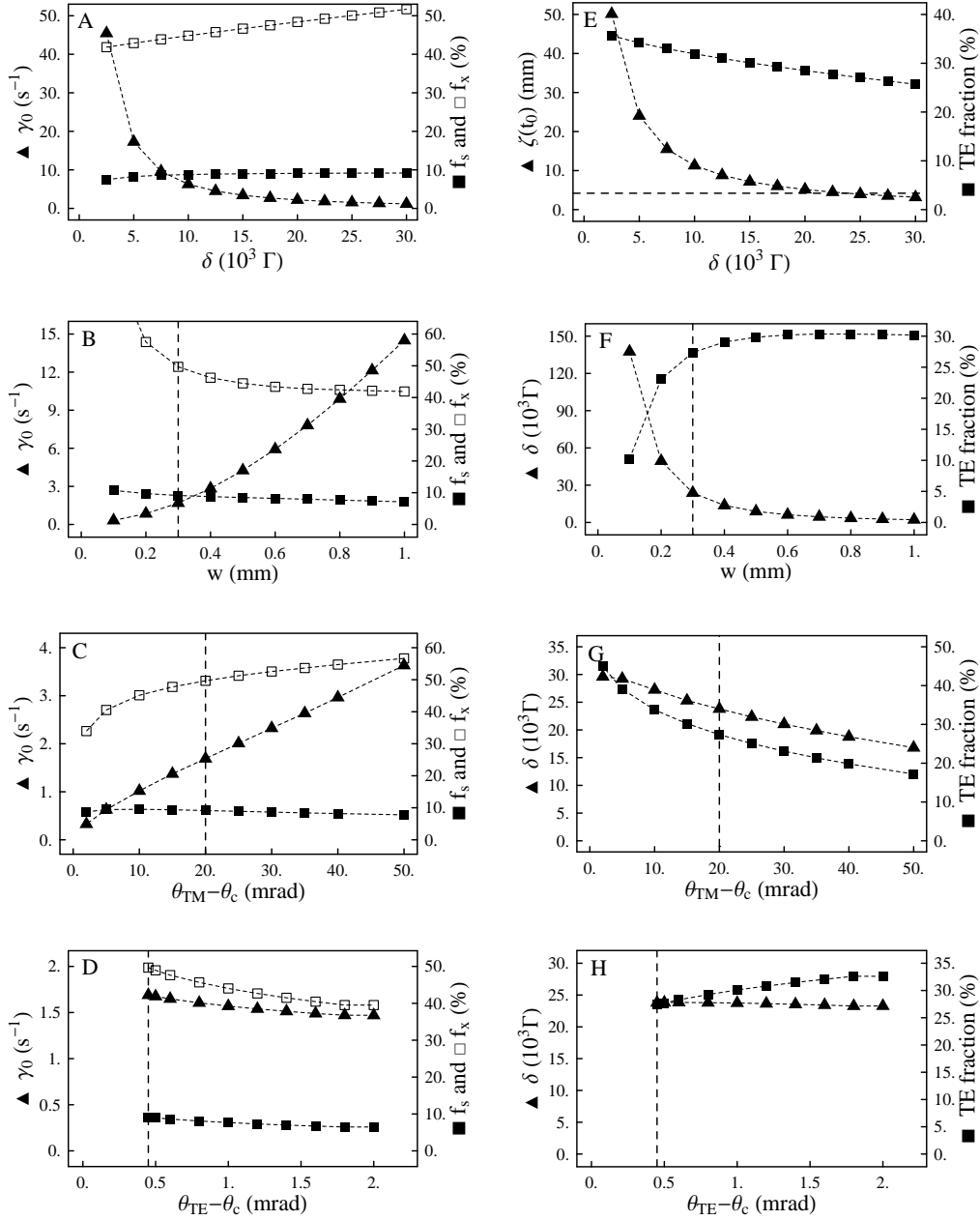
Figure 7.6: Determination of the scattering rate γ_0 and the trapping fractions f_s and f_x for (a) varying detuning δ, (b) varying beam waist w, and (c, d) varying angles of incidence θ_{TM} and θ_{TE}. Unless specified otherwise the parameters are taken as $\theta_{TM} = \theta_c + 20$ mrad, $\theta_{TE} = \theta_c + 450$ μrad, $P = 1$ W, $w = 300$ μm, $\zeta(t_0) = 4.2$ mm, and an unpolarized sample of falling atoms. The detuning δ (the initial height $\zeta(t_0)$ for (a)) and the distribution of power between the TE and TM polarized components is varied for each point in order to overlap the turning point with the trap minimum and to have the trap maximum closest and further from the surface at the same height. These optimized values are shown in (e, f, g, h).

atoms, but has no influence on the density. Therefore we will optimize the trap parameters for maximum f_s in the next section.

7.4.4 Parameter optimization

For a wide range of combinations of angles of incidence of the TE and the TM beams, denoted θ_{TE} and θ_{TM} respectively, there is a combination of detuning δ and power distribution between the TM and the TE polarization for which a confining potential is present. By changing the power distribution, the symmetry of the trap can be adjusted. The maximum closest to the surface can be increased by using a larger fraction of the power in the beam with the shorter decay length, because there is more power available to counteract the Van der Waals potential. The maximum farthest from the surface will consequently decrease. For a larger fraction of the power in the beam with the longer decay length, the reverse will happen. When the potential maxima closest to and farthest from the prism are equal the trap is maximally deep. By changing the detuning, the turning point of the falling atoms can be overlapped with the trap minimum. Mainly the amplitude of the $F = 1$ potential is changed, while the trap position is only shifted slightly. Using this parameter the loading can be optimized for every initial height of the atoms.

Figs. 7.6(a, b, c, d) show the optimized trap fractions f_x and f_s as discussed in the previous section, and the scattering rate γ_0 of the lowest vibrational state for varying detuning δ, beam waist w and angles of incidence of the TM and TE polarized beams θ_{TM} and θ_{TE} respectively. Unless specified otherwise, the parameters are taken as: initial height of the atoms $\zeta(t_0) = 4.2$ mm, the total laser power $P = 1$ W, beam waist $w = 300\,\mu$m, and the angles of incidence $\theta_{TM} = \theta_c + 20$ mrad, and $\theta_{TE} = \theta_c + 450$ μrad. Figs. 7.6(e, f, g, h) show the optimized values for the detuning (initial height of the atoms in case of Fig. 7.6(e)) and the fraction of power in the TE polarized beam.

In Fig. 7.6(a) the detuning δ is varied and for several values of δ the fall height for which the atoms turning point overlaps with the trap minimum is determined. This graph shows that both the scattering rate decreases and the loaded fraction f_s increases when the atoms are initially closer to the surface. In the experiment the MOT is at 4.2 mm above the surface, which is as close to the surface as experimentally possible. We come to the same conclusions for other choices for the angles of incidence for the TE and TM polarized beam.

Fig. 7.6(b) shows the trapped fraction and the scattering rate for different values of the beam waist. The graph shows that the trapped fraction increases slightly and the scattering rate decreases rapidly for decreasing beam waist, mainly because a larger detuning δ can be used. Similar results have been obtained for other values for the angles of incidence of the TE and TM polarized beams. Since the detected signal will be the sum over all trap sites, choosing a larger waist will result in more signal. We choose a waist of 300 μm as an intermediate.

Although we are free to choose whether TM or TE has the shorter or longer decay length, power considerations convinced us to choose the TM polarization to have the shorter decay length, since this is the higher power beam and the transmis-

sivity into the EW is highest for this polarization. The smallest angle of incidence should be further away from critical than its divergence angle, so that the EW can be approximated with an exponential decay in order to simplify the potential calculations, and to avoid propagating light. The largest possible angle of incidence is $\theta_c + 50$ mrad, which is limited by the size of the last mirror SM.

Figs. 7.6(c) and 7.6(d) show the results for varying the angles of incidence θ_{TM} and θ_{TE}. The influence of a variation of θ_{TE} on especially the scattering rate is very moderate. Choosing a very small value for θ_{TE} increases the trapped fraction relatively more than the scattering rate and thus seems to be a good choice. The scattering rate is strongly influenced by a change of θ_{TM}, whereas the trap fraction f_s is more or less independent of this parameter. We will use a value of 20 mrad, for which the scattering rate is at an appropriate level.

7.4.5   Consequences for the experiment

The "optimum" trap parameters for a total laser power of 1 W and an initial height of the atoms of 4.2 mm are thus $\theta_{TE} = 450$ μrad, $\theta_{TM} = 20$ mrad, $w = 300$ μm, $\delta = 23.8 \times 10^3$ Γ and the fraction of power in the TE polarized beam is 27.4%. Cross-sections through the center of the resulting potential are shown in Fig. 7.5. The trap depth is approximately 0.2 $\hbar\Gamma$ corresponding to 57 μK. The trap frequency perpendicular to the surface is 25.6 kHz. This leads to an estimate of 45 vibrational levels in the trap. This justifies the classical treatment for determining the trapped fraction as mentioned in section 7.4.3.

This trap is deep compared to the spread in initial kinetic energies of < 10 μK, but shallow compared to the spread in initial potential energies of 0.18 $\hbar\Gamma$ due to the finite width of the typically 1 mm $1/\sqrt{e}$ diameter of the atomic cloud. However this distribution in incident energies results only in a very moderate spread of turning points due to the steepness of the $|1, \pm 1\rangle$ potential as shown by the dotted lines in Figs. 7.5(a, c).

When the EWs are created by Gaussian incident beams, the intensity decreases towards the edges. Since the Van der Waals potential is constant over the surface, the main effect is a decrease of the potential maximum closest to the surface. In order to increase the area of the trap it is necessary to have an asymmetrical trapping potential in the center of the trap, with the potential maximum closest to the surface higher than the potential maximum furthest from the surface.

Due to the last two effects, energy spread of the falling atoms and EWs created by a Gaussian beam, the calculated optimum trap fraction f_s of 10% in the center of the trap for monochromatic incident atoms has to be treated as a maximum value. The ratio of the width of the initial cloud of atoms and the height of the EW trap, scaled with the trap fraction f_s yields an upper limit to the expected density increase. This yields a density increase of $\lesssim 130$ with respect to the MOT density. When the temperature of the atoms trapped in the EW trap is estimated by half the trap depth the phase-space density could be increased by a factor $\lesssim 75$.

The ground-state life time of the EW trap is the inverse of the scattering rate γ_0, given by Eq. (7.7). For our parameters this yields $\gamma_0 \approx 1.7$ s^{-1}, which corresponds

to a life time for atoms in the vibrational ground state of 590 ms. However, this life time decreases rapidly for atoms in excited vibrational states. For realistic initial temperatures in the trap the trap lifetime decreases to a few times 10 ms. E.g. the life time for atoms in the 20th excited state is equal to the value of 14.3 ms that was obtained for the SW trap, that was discussed in the previous chapter and [15]. Hence, the use of a dark-state trap does not lead to the intended trap life time increase. This is probably because for a dark-state trap, scattering a photon leads to the atom being lost from the trap with a probability of almost 1. This in contrast to the case of the SW trap, for which scattering a photon only results in a slight heating of the trapped atom.

7.5   Probing considerations

This section deals with the problem of detecting atoms in the trap, since the evanescent probing method of chapter 6 is not straightforwardly applicable anymore. The first part of this section discusses some adjustments that have to be made that enable us to use the in-situ evanescent-probing technique. The second part of this section discusses the option to launch the atoms away from the surface and detect them in free space.

7.5.1   In-situ detection

Detecting the atoms in these traps is more challenging than detecting atoms in the standing-wave trap of chapter 6. Detecting when the atoms are trapped is a challenge since only one magnetic sub-state is trapped. Using the EW probe described in chapter 6 requires every atom to scatter many photons in order to have a detectable absorption. However, scattering only a single probe photon (linearly polarized) will almost certainly result in losing the atom from the EW dark-state trap that is analyzed in this chapter.

A way to prevent this loss is to use a $\sigma^\pm$ polarized EW probe. The probe will excite the $|2, \pm2\rangle$ state to the $|3, \pm3\rangle$ excited state of the D_2 line, which can only decay back to the trapped state. The σ^+ and σ^- polarized trap sites can be detected independently by choosing either a σ^+ or a σ^- polarized probe. However, as already discussed in section 7.3.1, making a circularly polarized EW is very difficult. Moreover the probe has to be $\sigma^\pm$ polarized with respect to the quantization axis of the trapped atoms.

Another, perhaps more realistic possibility is to split the magnetic sub-levels by adding a small magnetic field parallel to the quantization axis of the trapped atoms. The closed transition $|2, \pm2\rangle \rightarrow |3, \pm3\rangle$ on the D_2 line can now be addressed independently from transitions to other magnetic sub-states by choosing the appropriate probe detuning. Also this probing scheme allows independent detection of the σ^+ and σ^- polarized trapping sites.

7.5.2   Time of flight detection

Another possibility is to release the atoms from the trap and detect them in free space during their flight. This can be done by e.g. pumping them back to the $F = 1$ ground state with a laser pulse tuned to the $F = 2 \rightarrow F' = 1$ or $F' = 2$ transition. It is also possible to slightly change the trap parameters, e.g. the distribution of the power between the TE and TM polarizations, to remove the trap and have the atoms roll down the potential gradient.

The detection can be performed using absorption imaging. However since the expected signal, especially during first attempts, will be low, one has to use a sensitive probing technique. We used a probe beam parallel to the prism surface which is focused with a cylindrical lens. This "flat" probe is very thin, so that it has a good time resolution for vertically moving atoms, but is also wide so that all atoms will be detected. The detection is done by measuring the difference signal between this probe beam and an extra reference beam of equal power that originates from the same laser. Although the probe is very weak in order to avoid saturation, we are able to detect absorption down to a level of 10^{-4} [16].

7.6   Experimental set-back: prism roughness

In practice we encountered experimental problems that prevented us from performing the experiment. The amount of stray light originating from the prism surface proved to be too much. Due to this problem the pump beam causes the atoms to be pumped to $F = 2$ before they enter the region of the EW field. This was apparent by trying to optimize the pump beam intensity using a "flat" probe as described in section 7.5, approximately 0.5 - 1 mm above the surface. In order to optimize the fraction of atoms that are pumped to the $F = 2$ state after the bounce, as described in section 7.3.2, we gradually increased the power of the pump beam. We observed, however, that falling atoms would already be pumped to the $F = 2$ state before reaching the prism surface. Loading of the dark-state trap is impossible while this problem exists.

We eliminated the possibility that stray beams cause this effect. We checked the system thoroughly for stray beams and eliminated them all until no more were present. Moreover all three entrance facets of the prism were tried to transmit the pump beam to further diminish the possibility of the scattering being caused by a stray reflection. This untimely pumping effect was persistent for different angles of incidence and the precise location and orientation of the beam on the prism surface.

Also the off-resonant repulsive EW caused atoms to be pumped over before reaching the prism surface. For parameters similar to the values used in [46] we were not able to observe atoms bouncing inelastically. All the atoms bounced from the surface with velocities expected for an elastic bounce. Pulsing the repulsive EW and decreasing the duration of the pulse did not improve the result.

We measured the amount of stray light with a calibrated CCD camera. It was calibrated without imaging optics using a beam of known power. By placing the camera above the prism we can determine the amount of scattered light in the solid
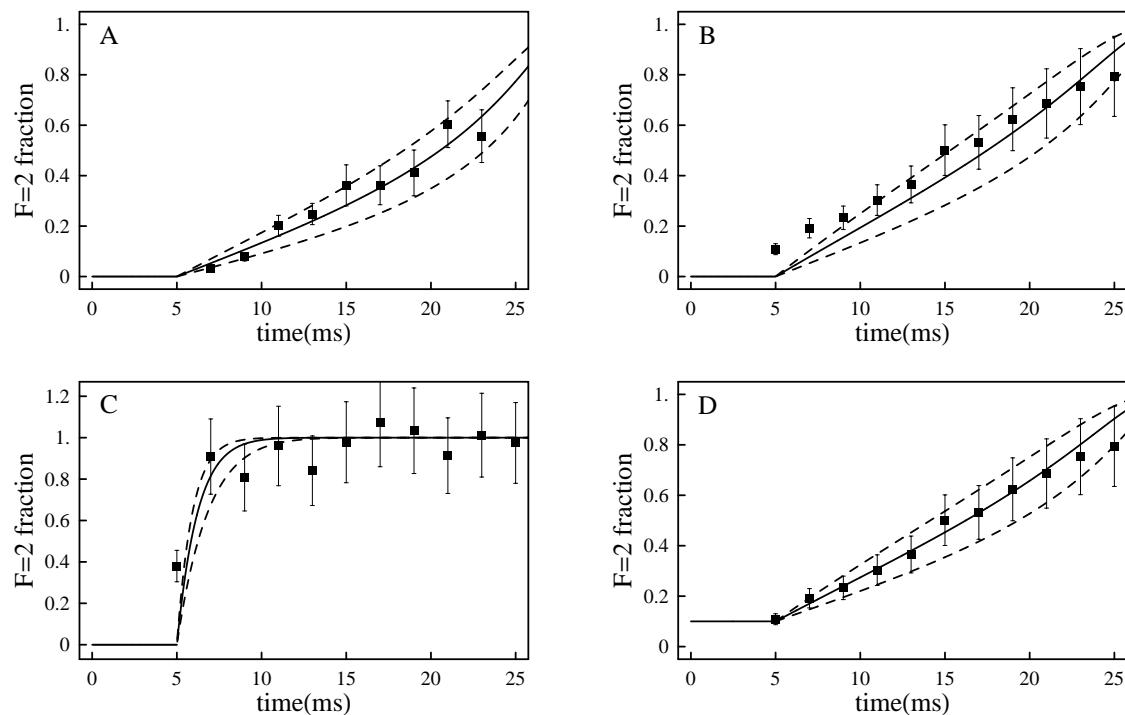
Figure 7.7: Atoms falling down in the $F = 1$ ground state are being pumped to the $F = 2$ ground state by stray light from a resonant pump beam with powers (a) 12.9 μW, (b, d) 19.4 μW (c) 401 μW, tuned to the $F = 1 \rightarrow F' = 2$ transition of the D_1 line. The black squares are measurements of the fraction of atoms that is pumped to the $F = 2$ ground state and the error bars correspond to an uncertainty of 10% in the atom number. The solid line is a calculation based on the measured fraction of stray light $9(3) \times 10^{-5}$ srad^{-1}, with the dashed lines calculations for the $1/e$ uncertainty limits of this value. In (d) the same data is shown as in (b), but for the calculated curves an initial fraction of 10% of the atoms in $F = 2$ is assumed, resulting in an even better agreement between measurement and theory.

angle of the imaging optics in front of the camera. This leads to a scattered fractional brightness of $9(3) \times 10^{-5}$ srad^{-1} with respect to the power incident on the prism. Within the measurement accuracy we observed no difference in scattering between TE or TM polarized incident light. From the image of the CCD camera, the waist of the beam at the prism surface was determined to be 1.0(1) mm. This measured fractional brightness is approximately 10 times higher than the fraction measured with the prism in the former setup that is described in section 4.3.1. For this setup D. Voigt reported a fraction of 5×10^{-6} in a solid angle of 5% [130].

With this information we can determine the rate at which atoms make a spontaneous Raman transition from $F = 1$ to $F = 2$ due to the scattered light at a certain height above the prism surface. Fig. 7.7 shows measurements of atoms prepared in $F = 1$ being pumped to $F = 2$ during their fall. The TM polarized pump beam was switched on 5 ms after the release of the atoms and was tuned to the $F = 1 \rightarrow F' = 2$ transition of the D_1 line. The measurement was performed

for 12.9 μW (Fig. 7.7(a)), 19.4 μW (Fig. 7.7(b)), and 401 μW (Fig. 7.7(c)) pump beam power. The error bars of the measurements correspond to a realistic uncertainty of 10% in the measurement of the number of atoms. The lines in the graphs are calculations using the fractional brightness. The source of the stray light is assumed to be a point source. The solid lines are calculations for the mean value of the fractional brightness, the dashed lines correspond to a fractional brightness one standard deviation away from the measured fractional brightness. The measurements are in perfect agreement with the calculations, indicating that the stray light from the surface is indeed the cause of the problem. The offset between the measurement and the theory curve in Fig. 7.7(b) suggests that the sample of atoms was not produced purely in the $F = 1$ state. Taking this into account results in an even better agreement as shown in Fig. 7.7(d).

After disassembling the prism from the vacuum setup, a visual inspection of its surface using an optical microscope showed point and line shaped structures. These features could not be cleaned, so that we have to assume that these are dents and scratches. The actual cause of these features cannot be determined anymore. A possibility is that the original commercial prism did not meet its specifications. However, since we did not encounter problems with an equal prism we used previously, we expect the polishing procedure of the extra optical surfaces on the prism, that are described in section 4.3.2, to be the cause. In order for these surfaces to be large enough for polishing, extra substrates of the same material were adhesively glued to the prism. After the polishing was finished these substrates were removed and the remaining glue was removed by cleaning with acetone and subsequent cleaning with methanol. Any hard particles in this glue might have caused the observed damage to the prism surface.

7.7   Conclusions

We have performed a numerical analysis of the loading of an evanescent-wave dark-state trap in order to find a set of suitable experimental parameters. Several trap geometries and their (dis)advantages were discussed. The analysis was performed for a geometry in which the two beams that create the evanescent dark-state trap are nearly copropagating. This trap is loaded from atoms that are transferred to the trapped state during their reflection from an evanescent-wave mirror. We derived that, independent of the trajectory of the atoms and the spatial distribution of the pump field, a fraction $1 - e^{-2}$ of the atoms should be transferred during a full reflection in order for the pump rate at the turning point of the atoms to be maximum.

By systematically varying the experimental parameters within the experimental limits, we found a set of optimized parameters for which the trapping fraction was maximum and the scattering rate was minimal. This resulted in a trap that was 57 μK deep with a trap frequency in the tightest direction of 25.6 kHz. We estimated that 10% of the atoms that fall onto a trap region can actually be trapped. A density increase of a factor 130 and a phase-space density increase with a factor 75 with

respect to the MOT values should be possible.

The life time is limited by the fact that scattering a photon leads to an almost immediate loss of the atom from the trap. Even though the trap life time for atoms in the lowest vibrational state can be as long as 600 ms, the expected life time for samples with realistic initial temperatures is comparable to the values that were achieved with the red detuned standing-wave trap that was discussed in the previous chapter.

We have found experimentally that the experiment poses very stringent requirements on the prism surface quality. The insufficient surface quality of our prism prevented the atoms from reaching the surface in $F = 1$, and thus from being loaded into the dark state trap. It should be expected that the surface quality will also be a limiting factor for the lifetime of atoms trapped in the EW dark state trap.

8 An atom interferometer using spontaneous decay

This chapter is based on the following paper:

R.A. Cornelussen, R.J.C. Spreeuw, and
H.B. van Linden van den Heuvell,
submitted for publication.

In this chapter we investigate the question of whether Michelson type interferometry is possible where the role of the beam splitter is played by a spontaneous Raman transition. This question arises from a detailed inspection of trajectories of atoms bouncing inelastically from an EW mirror. Each final velocity can be reached via two possible paths, with the Raman transition occurring either during the ingoing or the outgoing part of the trajectory.

At first sight, one might expect that the spontaneous character of the Raman transfer would destroy the coherence and thus the interference. We investigated this problem by numerically solving the Schrödinger equation and found that interference fringes in velocity space nevertheless are expected, even when random photon recoils are taken into account.

8.1   Introduction

Throughout this thesis we have considered processes where an atom undergoes spontaneous Raman pumping between two internal atomic states that interact differently with the applied evanescent fields. This process has been used as a mechanism to efficiently load low-dimensional traps. In earlier experiments we studied the behavior of atoms that reflect from an evanescent-wave mirror while undergoing such a spontaneous Raman transition during their reflection [46]. When the repulsive potential experienced by the final state is lower, the atoms lose kinetic energy during this process and hence bounce inelastically from the potential.

The final velocity of an atom depends on the position where it made the Raman transfer. Looking at the trajectories in detail we see that two trajectories can end up at the same final velocity. An atom can be transferred to the second state on the ingoing or the outgoing part of its trajectory, as is shown in Fig. 8.1(a). Cognet *et al.* [131] have performed similar experiments where the transfer to the second internal state was by a *stimulated* Raman transfer. They observed interference patterns, in the form of Stückelberg oscillations in the diffraction efficiency of atoms from polarization gradients in an evanescent-wave mirror.

This leaves the intriguing question whether interference is possible when the transfer is by a *spontaneous* Raman transition. At first sight one would answer this question negatively, since the spontaneously emitted photon could in principle be detected, and thus would provide "which way" information. Furthermore, a spontaneous process is generally considered incoherent and not deterministic due to the random direction in which the photon is emitted and the resulting random recoil to the atom. Intuitively, both effects would destroy the interference.

On the other hand there are several indications that spontaneous Raman transitions are not necessarily incoherent processes. Loudon [132] derives that the linewidth of the spontaneous emission of an atom that is optically driven by a weak field is equal to the linewidth of the driving field and not to the linewidth of the transition that is driven. Eichmann *et al.* [133] report interference of the spontaneous emission of two well localized trapped ions. The experiments of Cline *et al.* [134] show that the phase of the atomic wave function is preserved over the spontaneous process. They trapped ^{85}Rb atoms in a far off-resonance dipole trap with a detuning that is much larger than the fine-structure splitting between the D_1 and D_2 line. The observed trap life time could only be explained by coherently adding the spontaneous Raman scattering amplitudes of the D_1 and D_2 lines. The posed question will be answered in this chapter by solving the Schrödinger equation.

This chapter is structured as follows. We first present a semi-classical picture, that we use to make qualitative predictions about the behavior of the interference effects, if present. The question whether interference is possible will be answered by solving the Schrödinger equation in two different ways. The first method will employ stationary analytical solutions of the time-independent Schrödinger equation, but is limited to monochromatic wave functions. The second method will propagate a wave packet by numerically solving the time-dependent Schrödinger equation. The last section will focus on the implications and requirements of a future experiment.
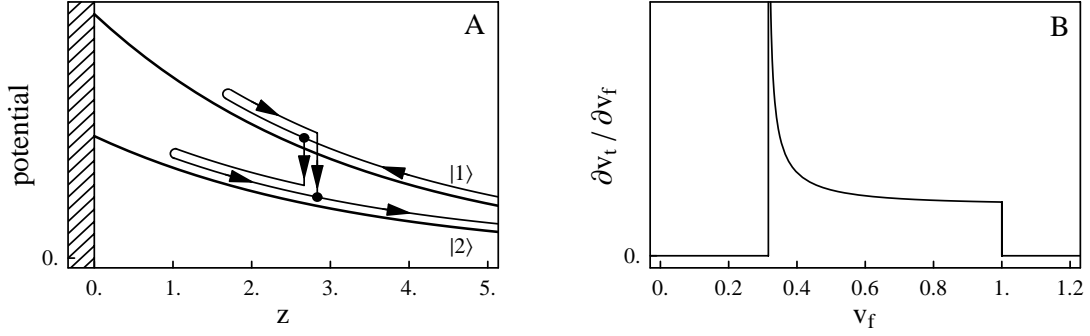
Figure 8.1: (a) An atom that is transferred from state $|1\rangle$ to state $|2\rangle$ can be transferred on the ingoing or the outgoing part of the trajectory. These two paths possibly interfere. (b) Caustic in the final velocity distribution of an inelastic EW mirror for initial velocity $v_i = 1$ and ratio between the potentials $\beta = 0.1$.

8.2 Semi-classical description

We start the description of inelastic bouncing in a (semi) classical way. In the first part we derive the classical velocity distribution of the inelastically bouncing atoms. After that we give a semi-classical picture of the phase difference between the two possible trajectories. Based on this picture we derive how the possible interference patterns change on variation of the available experimental parameters.

8.2.1 Primary rainbow caustic

We consider atoms bouncing inelastically from an evanescent-wave (EW) mirror, defined by a repulsive potential $V_1 \exp(-2\kappa z)$. Here κ^{-1} is the decay length of the EW field, as defined by Eq. (2.19). An atom in state $|1\rangle$, with incident velocity $-v_i$ ($v_i > 0$) moves, in a classical description, on a trajectory

$$z(t) = z_0 + \frac{1}{\kappa} \ln \left(\cosh \left(v_i \kappa t \right) \right), \tag{8.1}$$

with z_0 the position of the turning point of the atom, given by

$$z_0 = \frac{1}{2\kappa} \ln \left(\frac{2V_1}{mv_i^2} \right). \tag{8.2}$$

The atom's trajectory through phase space is given by

$$v_1^2(z) = v_i^2 - \frac{2V_1}{m} e^{-2\kappa z}. \tag{8.3}$$

While moving in the repulsive potential, the atom can make an optical Raman transition to state $|2\rangle$. The repulsive potential $V_2 \exp(-2\kappa z)$ experienced by this latter state is significantly lower. The ratio V_2/V_1 depends on the detuning of the EW with respect to the D_1 line. For convenience, we define $\beta = V_2/V_1$, thus $\beta < 1$. The transfer leads to a loss of potential energy of the atom so that it will leave

the potential with a velocity $v_f \leq v_i$. The trajectory through phase space after this transfer is given by

$$v_2^2(z) = v_f^2 - \frac{2\beta V_1}{m} e^{-2\kappa z}. \tag{8.4}$$

The velocity v_f with which an atom in state $|2\rangle$ leaves the potential depends on its velocity v_t at the moment of the transfer. By combining Eqs. (8.3) and (8.4) it follows that the final velocity v_f depends on the transfer velocity v_t as

$$v_f(v_t) = \sqrt{v_t^2 + \beta\left(v_i^2 - v_t^2\right)}. \tag{8.5}$$

The spontaneous Raman transfer leads to a caustic in the velocity distribution of atoms that leave the potential in state $|2\rangle$. There is a large population of the outgoing velocity class around $\sqrt{\beta}v_i$, which corresponds to atoms that are transferred in the turning point, with $v_t = 0$. A transfer in the motional turning point is most likely since atoms spend a long time there (classically zero velocity) and the scattering rate is highest, because the light intensity is highest. There is a tail to larger velocities, up to a maximum of v_{in}, which corresponds to atoms that are pumped over on their way in or their way out of the potential.

Classically, the caustic, the distribution of final velocities, is proportional to $\partial v_t/\partial v_f$. This distribution is shown in Fig. 8.1(b). In this description depletion of the initial state $|1\rangle$ is not taken into account, so the results are only valid for a small transfer rate.

Like many processes that occur near the edge of a classically allowed domain, this caustic maps on the well known description of the rainbow, as was already noticed earlier, and several analogies between the two phenomena are possible [46]. Furthermore, we have successfully observed and characterized this caustic distribution. The minimum final velocity $\sqrt{\beta}v_i$ is called the *rainbow velocity* in analogy with the *rainbow angle* for an optical rainbow caustic.

8.2.2 Supernumerary rainbows

There is, however, an intriguing question. According to Eq. (8.5) both atoms that are transferred to state $|2\rangle$ at velocities $\pm v_t$, i.e. on their way in and out of the potential, end up on the same trajectory through phase space and will thus leave the evanescent field with the same final velocity v_f. This is also shown in Fig. 8.1(a). This raises the question whether there could be interference between the part of the atomic wave function transferred on the ingoing trajectory and the part, describing the same atom, transferred on the outgoing trajectory. This interference would manifest itself in velocity space. Following the rainbow analogy, one could call these interference patterns *supernumerary rainbows*. In our case the question about interference is highly non-trivial, because a spontaneous Raman process is involved that may destroy the coherence between the paths.

We will give a semi-classical analysis of this problem and a method to determine the phase difference between the two paths. Furthermore two mechanisms will be discussed that could destroy the interference. The first is related to the atom's initial

phase-space distribution, which is an argument that is generally applicable to atom interferometers. The second is more specific for our case and involves the effect of the spontaneous recoil.

Phase difference between trajectories A schematic representation of two trajectories through phase space of atoms that enter the potential in state $|1\rangle$ and leave the potential in state $|2\rangle$, is shown in Fig. 8.2(a). The phase difference $\Delta\varphi$ between the two trajectories is given by

$$\Delta\varphi = \frac{m}{\hbar} \int_{-v_t}^{v_t} (z_1(v) - z_2(v)) \, \mathrm{d}v, \qquad (8.6)$$

where $z_1(v)$ and $z_2(v)$ correspond to the inverse of Eqs. (8.3) and (8.4) respectively. The transfer velocity v_t can be derived from Eq. (8.5). This phase difference in Eq. (8.6) is proportional to the area between the two curves, indicated in gray in Fig. 8.2(a). From the evaluation of the integral for various parameters we learn that the fringe period decreases for increasing initial velocities v_i, for increasing final velocities v_f, for smaller β and for larger decay length (smaller κ).

General argument for matter-wave interferometers The center-of-mass motion and position of an atom can be described by a wave packet which is subject to Heisenberg's uncertainty relation $\Delta z \Delta v_z \geq \hbar/2m$. The distribution of uncertainty between position z and momentum mv_z is determined by the experimental preparation procedure of the atoms.

For a wave packet that initially has a large spread in momentum, and a well defined position, it is not possible to unambiguously determine the phase difference between the two possible paths, since the wave packet is spread out over several classical trajectories through phase space. This is indicated by the dashed curves in Fig. 8.2(a). With such a wave packet it is possible to determine whether the atom transferred to state $|2\rangle$ on its ingoing or outgoing path, by observing the timing of the spontaneously emitted photon. The spatial compactness of the wave packet enables this measurement. Therefore, it is not expected that wave packets with this shape show interference.

On the other hand, a minimum uncertainty wave packet with a narrow initial momentum spread, and therefore some extension in the spatial dimension, will more closely follow a classical trajectory through phase space, as defined by Eqs. (8.3) and (8.4). This is indicated by the dotted curve in Fig. 8.2(a). Due to this, the phase difference between the two paths, equivalent to the gray area of phase space enclosed by the two paths, is well defined. It comes as no surprise that the two points in phase space where a transition to the final trajectory is possible are covered simultaneously by the wave packet. This is the reason that no "which way" information can be obtained by observing the spontaneously emitted photon.

Thus the initial trade-off between position and momentum uncertainty in a bandwidth limited wave packet determines whether interference can be a priori excluded
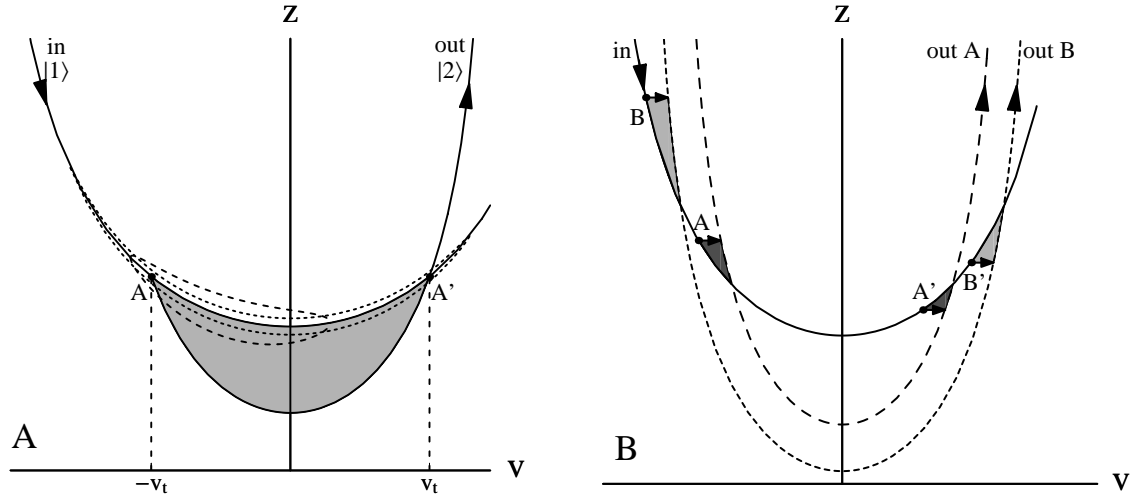
Figure 8.2: (a) Phase space trajectories of atoms being repelled by an evanescent potential. Atoms initially in state $|1\rangle$ can be transferred to state $|2\rangle$ and continue on a different path through phase space. The transfer to such a trajectory can occur either on the ingoing branch of the trajectory, at point A, or on the outgoing branch, at point A'. The accumulated phase difference between these two paths, indicated by the enclosed gray area, may give rise to interference effects. A wave packet with a large initial velocity spread, indicated by the dashed curve, can not overlap both transfer points at the same time. Therefore "which way" information can be obtained by observing the timing of the spontaneously emitted photon. We do not expect that such a wave packet will lead to interference. A wave packet with a small initial velocity spread, as indicated by the dotted curve, can overlap both transfer points simultaneously. No "which way" information can be obtained from the emitted photon and we expect that interference is possible in this case. (b) When the transfer is a spontaneous Raman process, the momentum kick due to the stochastic nature of the spontaneous emission process has to be taken into account. For a given z component of the recoil this gives rise to extra phase factors, indicated by the dark gray areas for a small final velocity and by the light gray areas for a higher final velocity.

or not. This requirement is necessary but not sufficient, since in the actual realization the incoherent nature of the transfer between states must yet be taken into account.

Specific argument for interferometers with spontaneous decay   The random direction of the spontaneously emitted photon can be taken into account in the motion of the atom by a random momentum jump. This makes the atom propagate on a different trajectory through phase space than it would have without the random recoil. Since we treat our atomic bounce as a one-dimensional problem, only the z component of the recoil is of importance to us. The momentum changes are indicated by horizontal arrows in the phase-space diagram of Fig. 8.2(b).

For a single atom, or a collection of distinguishable atoms, the size and sign of the z component of the spontaneous recoil could be measured by detecting in which direction the photon was emitted. Due to this possibility there will be a set

of interference patterns, each with a well defined recoil direction. By disregarding the information present in the scattered photons, we probe the incoherent sum of all these interference patterns [135].

The transfer moments that contribute to a particular final velocity of one of these interference patterns are not symmetrical around the moment of closest approach anymore, as indicated by the points A and A' in Fig. 8.2(b). The phase difference between the two paths is different with respect to the recoilless case, and it depends on the direction of the recoil. It is indicated by the dark gray areas in Fig. 8.2(b). In order for the interference to be experimentally observable the difference between the interference patterns with a certain recoil direction should not be too large. This means that the phase difference between recoil components in the $\pm z$ directions should be less then π. For larger final velocities these phase corrections get larger as is apparent from the larger area around the points B and B' in Fig. 8.2(b). So we expect the visibility of the interference to decrease for larger final velocities.

8.3 Time-independent approach

The question whether interference is visible will be answered by considering analytical stationary solutions of the Schrödinger equation for particles with a total energy $p_0^2/2m$. We show that the interference survives the incoherent nature of the spontaneous Raman transfer to state $|2\rangle$ for various experimental parameters. Furthermore the qualitative predictions of section 8.2 are confirmed.

8.3.1 Analytical stationary solutions

The time-independent Schrödinger equation

$$-\frac{\hbar^2}{2m}\frac{\partial^2}{\partial z^2}\psi_1(z) + V_1 e^{-2\kappa z}\psi_1(z) = \frac{p_0^2}{2m}\psi_1(z),\qquad(8.7)$$

describes stationary states with a total energy $p_0^2/2m$ on the potential $V_1\exp(-2\kappa z)$. It thus describes particles with momenta $\pm p_0$ in the asymptotic limit of large z. This is one of the few examples where the eigenfunctions of the Schrödinger equation are analytically known. The solutions are given by [136]

$$\psi_1(z) = \sqrt{\frac{4}{\pi\kappa}\sinh\left(\frac{\pi p_0}{\hbar\kappa}\right)}K_{ip_0/\hbar\kappa}\left(\frac{\sqrt{2mV_1}}{\hbar\kappa}e^{-\kappa z}\right),\qquad(8.8)$$

where $K_\alpha(\beta)$ is the Bessel-K function of order α evaluated for argument β [137].

Figure 8.3 shows $|\psi_1(z)|^2$ for an evanescent-wave potential with $\kappa = k_0/8$, with k_0 the wave vector of a photon, and for several values of the initial momentum p_0. To separate them, for better visibility, they are shown at an offset of their own energy $p_0^2/2m$. It is clearly visible that far from the surface, where the exponential potential vanishes, the wave function closely resembles that of a free particle. Also obvious is that the higher energy solutions move deeper into the evanescent wave potential. Note that in the classically forbidden region the wave function vanishes very rapidly, more rapidly than exponential.
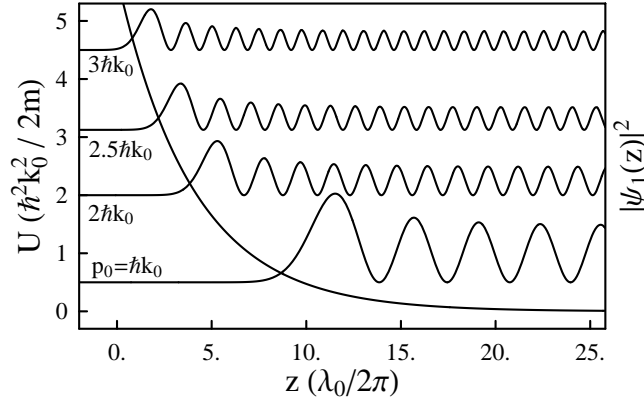
Figure 8.3: Examples of density distribution $|\psi_1(z)|^2$ with $\psi_1(z)$ a stationary solution of Schrödinger's equation with an exponentially decaying potential as given by Eq. (8.8). Plots are shown for initial momenta of $p_0 = \hbar k_0$, $2\hbar k_0$, $2.5\hbar k_0$, and $3\hbar k_0$, and are shown at an offset of their own energy $p_0^2/2m$. The decay length of the evanescent wave is $\kappa^{-1} = k_0/8$.

8.3.2 Spontaneous Raman transfer

An atom with initial momentum p_0 that is initially in state $|1\rangle$ can make a Raman transition to state $|2\rangle$ by scattering photons from the optical evanescent potential. In this new state the interaction of the atoms with the evanescent potential is changed and they are now repelled by a lower potential of height V_2. The atom can make a transition to several of the eigenfunctions $\psi_{2,p}(z)$ with final momentum p in the potential $V_2 \exp(-2\kappa z)$.

The final wave function in momentum space is given by

$$\phi_k(p) \sim \int_0^\infty \psi_1(z) e^{-\kappa z - ikz} \psi_{2,p}(z) \mathrm{d}z, \tag{8.9}$$

where the recoil due to the spontaneous Raman transition is taken into account by projecting the initial wave function with an extra momentum factor $\psi_1(z) \exp(-ikz)$ onto the eigenfunction $\psi_{2,p}(z)$. Here $\hbar k$ is the momentum component of the recoil in the z direction. The coupling between these two states is determined by the Rabi frequency, which is proportional to the electric field amplitude, and is thus given by $\exp(-\kappa z)$ and not by $\exp(-2\kappa z)$ which is proportional to the evanescent-wave intensity. As already discussed in section 8.2.2, there will be interference patterns $|\phi_k(p)|^2$ for every value $\hbar k$ of the recoil. A measurement constitutes of the sum of all these possible interference patterns. In this derivation we will assume an isotropic distribution of the recoil momentum $\hbar k$. This is not straightforward, since the distribution depends on the polarization of the spontaneously emitted photon. We will come back to this point in section 8.5.3. This leads to

$$|\phi(p)|^2 = \int_{-k_0}^{+k_0} |\phi_k(p)|^2 \mathrm{d}k. \tag{8.10}$$
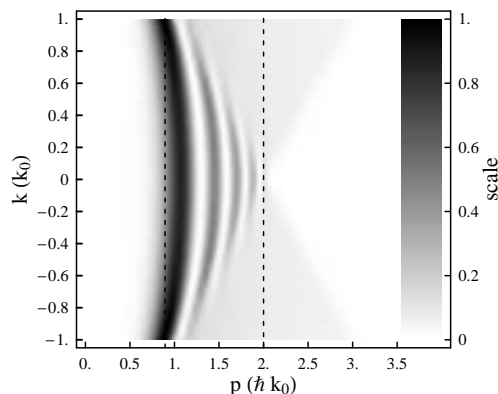
Figure 8.4: The behavior of the interference pattern $|\phi_k(p)|^2$ versus the final momentum p for various values of the z component of the photon recoil $\hbar k$ for parameters $p_0 = 2\hbar k_0$, $\kappa = k_0/8$, and $\beta = 0.2$. The dotted lines indicate the initial momentum and the rainbow momentum.

8.3.3 Results and discussion

Fig. 8.4 shows the behavior of the momentum distribution for various values of the z component of the photon recoil $\hbar k$. It is calculated using Eq. (8.9), with an initial momentum $p_0 = 2\hbar k_0$, a potential steepness $\kappa = k_0/8$, and potential reduction $\beta = 0.2$. Some points are immediately apparent from this graph. First of all, as expected, the main part of the momentum distribution extends between the initial momentum p_0 and the rainbow momentum $\sqrt{\beta}p_0$, both indicated by vertical dotted lines. The distributions "peak" near the rainbow velocity, resembling the caustic distribution. Secondly, for every recoil direction there are supernumerary rainbows visible. Although the interference washes out for larger values of the recoil, the remaining interference fringes are present at more or less the same final momenta. They only shift slightly to lower final momenta for larger values of the recoil. This already indicates that the spontaneous recoil does not completely wash out the interference. The behavior of the interference is independent of the direction of the recoil. This makes sense if one realizes that a photon emitted on the ingoing part of the trajectory has the same effect on the momentum distribution as a photon that is emitted in the opposite direction on the outgoing part of the trajectory.

Fig. 8.5 shows the results of calculations of Eq. (8.10) for different experimental parameters. The dashed lines are calculations of $|\phi_0(p)|^2$, without a spontaneous recoil, so the expected interference patterns for a coherent splitting process. The solid lines are calculations of $|\phi(p)|^2$ in which the effect of the recoil has been incorporated. Indeed the summation over the spontaneous recoil does not destroy the interference pattern, even for these extremely low initial momenta. The small parts of the distribution $|\phi_0(p)|^2$ at momenta smaller than the rainbow momentum and larger than the incident momentum are evanescent matter waves that extend into the classically forbidden regions.

Several of our predictions that were made for the general case of a coherent interferometer are noticeable in these graphs. Indeed the fringe spacing decreases
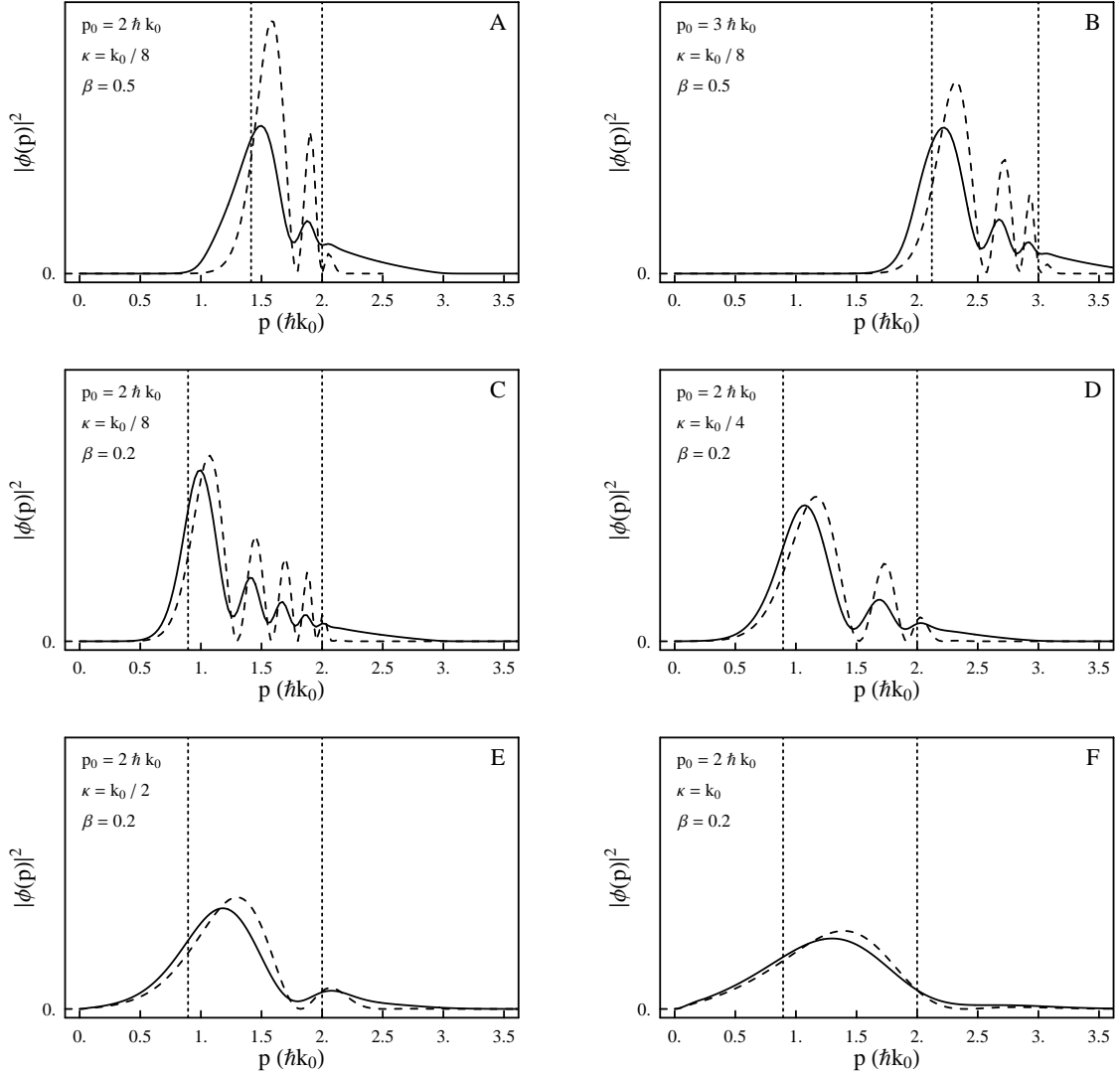
Figure 8.5: Interference patterns calculated for different parameters. Solid lines: $|\phi(p)|^2$, with the effect of a spontaneous recoil, and dashed lines: $|\phi_0(p)|^2$, without the effect of a spontaneous recoil. The dotted lines indicate the initial momentum and the rainbow momentum.

for larger initial and final momenta, for longer decay lengths κ^{-1} of the evanescent field, and for smaller values of β. Furthermore, as predicted for the case of an incoherent interferometer, the visibility of the graphs in which the effect of the recoil has been taken into account decreases for larger final momenta.

8.4 Time-dependent approach

In the previous section we have shown that the incoherent nature of the spontaneous Raman transfer does not prevent us to observe interference. In this section we will show that the interference phenomena will also be visible for a wave packet with
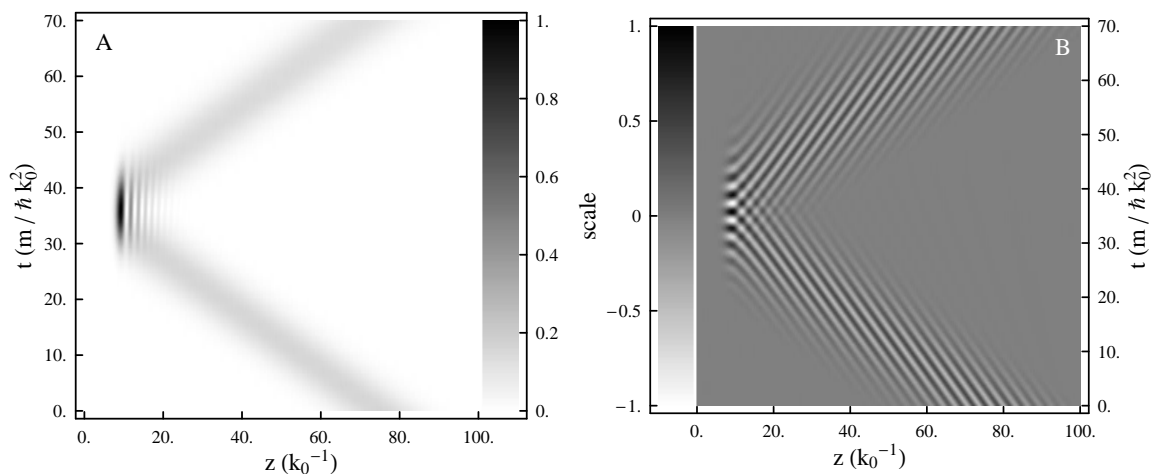
Figure 8.6: Evolution of (a) the density distribution $|\psi_1(z,t)|^2$ and (b) the real part of the wave packet $\psi_1(z,t)$, calculated for an evanescent wave with $\kappa = k_0/8$, and a wave packet with initial height $z_0 = 75/k_0$, initial width $\sigma_z = 7/k_0$, and initial momentum $p_0 = 2\hbar k_0$.

a finite momentum spread. In the analysis we will closely follow the Monte-Carlo wave-function approach [138, 139].

8.4.1 Transfer-free evolution

We consider the evolution of a diffraction limited wave packet in state $|1\rangle$

$$\psi_1(z, t = 0) = \sqrt{\frac{1}{(2\pi)^{1/2}\sigma_z}} e^{ik_z z} e^{-\frac{(z-z_0)^2}{4\sigma_z^2}} \tag{8.11}$$

with initial height z_0, initial width σ_z, and initial momentum $p_0 = \hbar k_z$. It is normalized such that $\int |\psi(z,0)|^2 dz = 1$ and $\int (z - z_0)^2 |\psi(z,0)|^2 dz = \sigma_z^2$. The evolution of the wave packet is calculated by numerically solving the time-dependent Schrödinger equation

$$i\hbar\frac{\partial}{\partial t}\psi_1(z,t) = -\frac{\hbar^2}{2m}\frac{\partial^2}{\partial z^2}\psi_1(z,t) + V_1 e^{-2\kappa z}\psi_1(z,t), \tag{8.12}$$

when it reflects from the evanescent-wave potential with a potential height V_1 at $z = 0$ using the *Quantum kernel* [141] package in *Mathematica* [140]. This results in a wave packet $\psi_1(z,t)$ at time t.

An example of such an evolution is shown in Fig. 8.6, where the density distribution and the real part of the wave function are plotted versus position z and time t. This graph is calculated for an evanescent wave with $\kappa = k_0/8$, and a wave packet with initial height $z_0 = 75/k_0$, initial width $\sigma_z = 7/k_0$, and initial momentum $p_0 = 2\hbar k_0$. The spatial width leads to a width of the momentum distribution of $\sigma_p = \hbar k_0/7$.

In these graphs several characteristics of the wave packet are visible. In Fig. 8.6(b) the difference between the phase velocity and the group velocity is apparent. Furthermore the dispersion of the wave packet is observable: its initial width is smaller than its final width. Also the slight tilt of the interference fringes during the reflection is due to dispersion. Atoms that arrive later in their turning point are the slower atoms that move less deep into the evanescent potential.

8.4.2   Spontaneous Raman transfer

At a time τ a transition to state $|2\rangle$ occurs, and the evolution abruptly continues on a potential that is a factor β lower. This corresponds to a Raman transition of an atom to another internal state that has a weaker interaction with the evanescent wave.

Immediately after the transfer the wave function in state $|2\rangle$ is described by

$$\psi_{\tau,k}(z,\tau) = \mathcal{N}\psi_1(z,\tau)e^{-\kappa z}e^{-ikz}, \tag{8.13}$$

where $\mathcal{N}$ denotes a normalization factor. The first exponent represents the mode function of the absorbed evanescent photon, and the second exponent the mode function of the spontaneously emitted photon. The evolution of this wave function can now be continued up to a time t_{end}, leading to a wave function $\psi_{\tau,k}(z,t_{\mathrm{end}})$. When t_{end} is large enough the entire wave packet effectively propagates in free space, so that the momentum distribution remains constant. The Fourier transform

$$\phi_{\tau,k}(p) \sim \mathcal{F}\left(\psi_{\tau,k}(z,t_{\mathrm{end}})\right) \tag{8.14}$$

of the wave packet at this time is the wave function in momentum space that endured a momentum kick $\hbar k$ at its transfer time τ.

Every atom of the sample that is transferred to state $|2\rangle$ is transferred at a random transfer time τ and undergoes a random recoil kick $\hbar k$ due to the spontaneously emitted photon. The transfer rate $\Gamma(\tau)$ at a certain time τ is given by

$$\Gamma(\tau) \sim \int_0^\infty \psi_1^*(z,\tau)V_1(z)\psi_1(z,\tau)\mathrm{d}z. \tag{8.15}$$

We again assume an isotropic distribution of the recoil momentum $\hbar k$. We have to add contributions with different τ and k in an incoherent way. In contrast to the original description of the Monte-Carlo wave-function method we do not evaluate the momentum distribution for a discrete number of random transfer moments τ and recoil momenta $\hbar k$, but integrate numerically over these values. For the momentum distribution as a function of the wave vector of the spontaneously emitted photon we get

$$|\phi_k(p)|^2 \sim \int_0^{t_{\mathrm{end}}} \Gamma(\tau)|\phi_{\tau,k}(p)|^2\mathrm{d}\tau. \tag{8.16}$$

A subsequent integration over this wave vector yields

$$|\phi(p)|^2 = \int_{-k_0}^{k_0} |\phi_k(p)|^2\mathrm{d}k \tag{8.17}$$

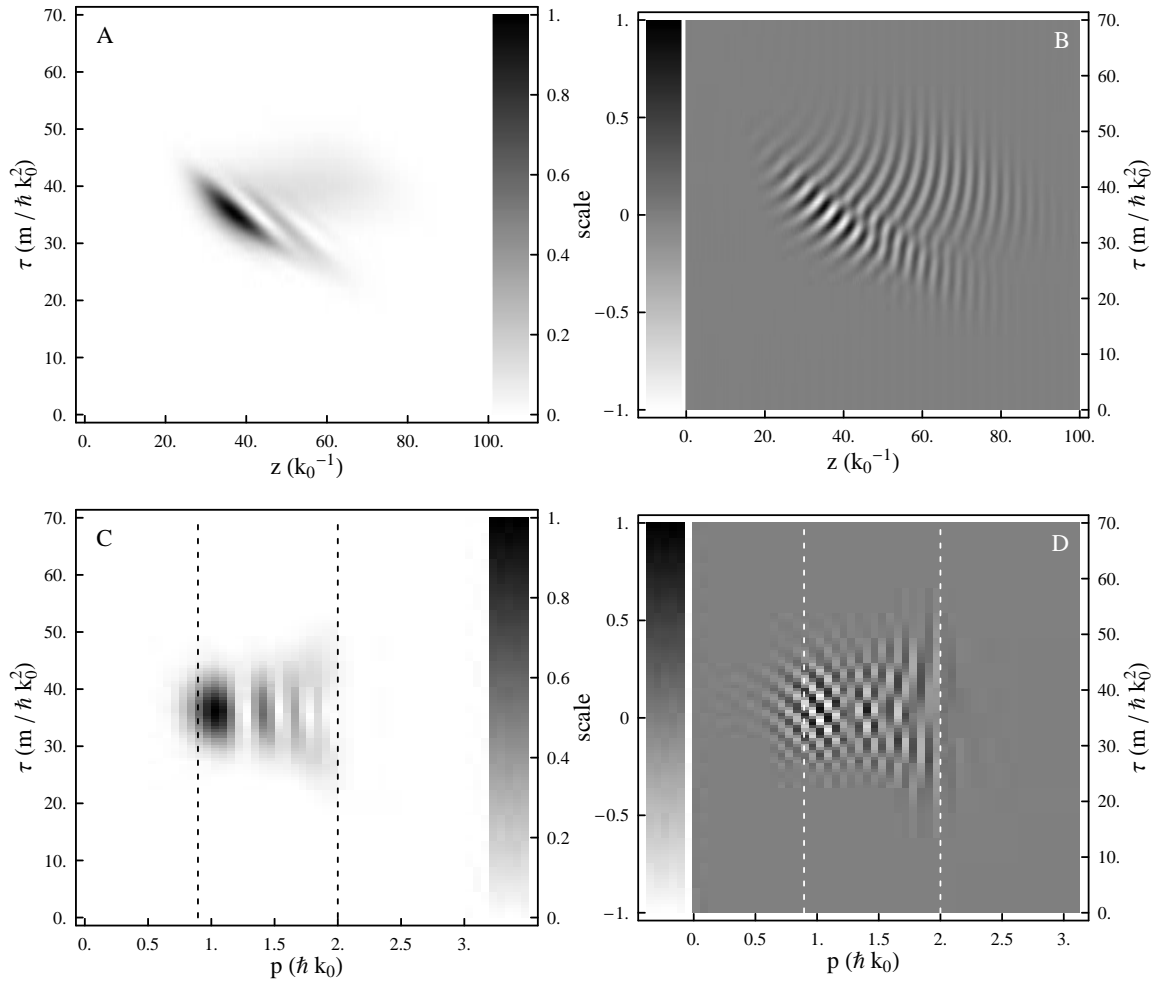for the momentum distribution of a sample of atoms.

Figure 8.7: (a) density distribution $|\psi_{\tau,0}(z, t_{\text{end}})|^2$, (b) real part of the wave packet $\psi_{\tau,0}(z, t_{\text{end}})$, (c) momentum distribution $|\phi_{\tau,0}(p)|^2$, and (d) real part of the momentum distribution $\phi_{\tau,0}(p)$. All these graphs are calculations without recoil, thus for $k = 0$. The data for a certain value of transfer time τ represent the wave function at the final time t_{end} if the evanescent field had been switched on for a very short time at time τ. These results are given at a large $t_{\text{end}} = 70 m/\hbar k_0^2$, so that the wave packet effectively evolves in free space, as is visible in Fig. 8.6. The graphs are calculated for an evanescent wave with $\kappa = k_0/8$ and $\beta = 0.2$, and a wave packet with initial height $z_0 = 75/k_0$, initial width $\sigma_z = 7/k_0$, and initial momentum $p_0 = 2\hbar k_0$. The dotted lines indicate the initial momentum and the rainbow momentum.

8.4.3   Results and discussion

Fig. 8.7 shows examples of the density and momentum distributions as a function of the transfer time τ in the absence of recoil, thus for $k = 0$. The data for a certain value of time τ represents the final wave function if the evanescent field had been switched on for a very short time at time τ. The plots are calculated for
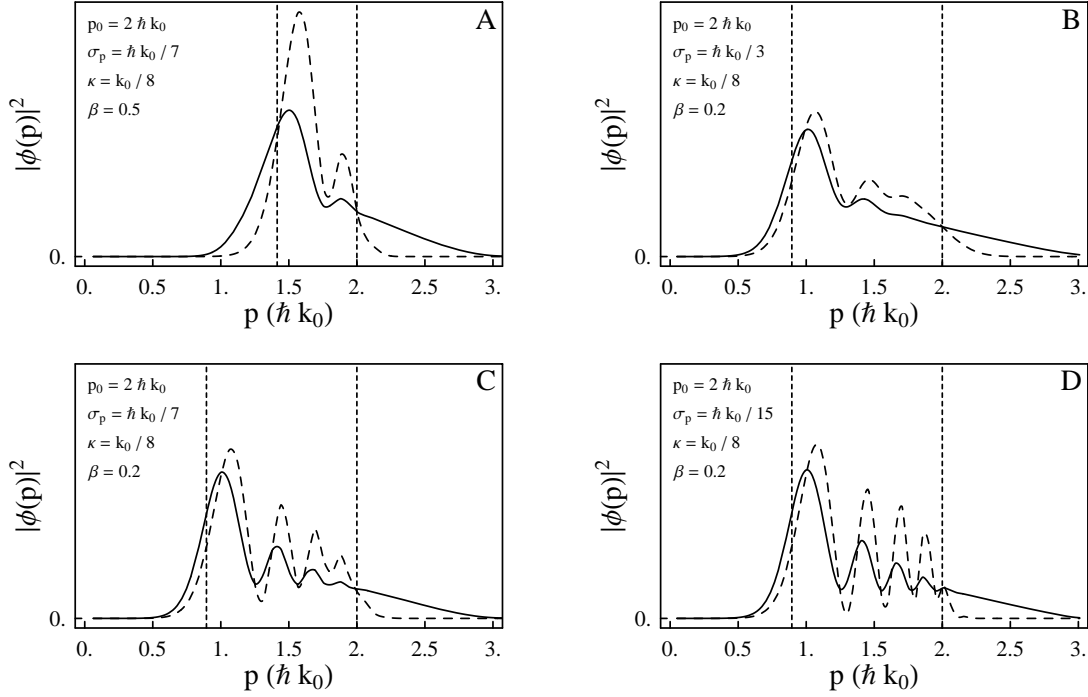
Figure 8.8: Interference patterns calculated for different parameters. Solid lines: $|\phi(p)|^2$, with the effect of a spontaneous recoil, and dashed lines: $|\phi_0(p)|^2$, without the effect of a spontaneous recoil. The dotted lines indicate the initial momentum and the rainbow momentum.

an evanescent wave with a decay length $\kappa^{-1} = 8/k_0$, a ratio of the two potentials $\beta = 0.2$ and a wave packet with initial height $z_0 = 75/k_0$, initial width $\sigma_z = 7/k_0$ and initial momentum $p_0 = 2\hbar k_0$. The momentum spread due to the finite size of the wave packet is $\sigma_p = \hbar k_0/7$. Both the density distribution $|\psi_{\tau,0}(z, t_{\text{end}})|^2$ and the real part of the wave function $\psi_{\tau,0}(z, t_{\text{end}})$, and the momentum distribution $|\phi_{\tau,0}(p)|^2$ and the real part of the wave function in momentum space $\phi_{\tau,0}(p)$ are shown.

Figs. 8.7(a) shows a line with high density that we interpret as atoms that are transferred in their turning point. It is extended in time due to the finite width of the wave packet and it is slanted because atoms that are transferred later have less time to fly away from the potential. We interpret the less intense area at larger distances and larger transfer times as atoms that are transferred on the outgoing part of their trajectory and thus leave the potential with a large velocity. In Figs. 8.7(c, d) is visible that atoms which are transferred either very early or very late, indeed leave the potential with unchanged momentum. Fig. 8.7(c) also shows that around the motional turning point, for τ approximately between $30 \ m/\hbar k_0^2$ and $45 \ m/\hbar k_0^2$, a large population near the rainbow momentum $\sqrt{\beta}p_0$ is created. It is furthermore visible that the supernumerary rainbow contributions that are created at different transfer times τ have the same final momentum. The phase fluctuations in momentum space, that are visible in Fig. 8.7(d), are of no importance since the various τ contributions add incoherently.

Fig. 8.8 shows graphs of $|\phi(p)|^2$ for some parameters. Fig. 8.8(a) must be

compared with Fig. 8.5(a), Figs. 8.8(b)-(d) must be compared with Fig. 8.5(c). It is obvious that even for a wave packet with a finite momentum spread the interference effects are still present. The parameters for Figs. 8.8(b)-(d) are equal except for the initial width σ_z of the wave packet and thus the momentum spread $\sigma_p = \hbar/\sigma_z$. It is clear that the interference fringes are more apparent for a wave packet with a smaller momentum spread.

8.5   Experimental considerations

This section discusses the implications of the results of the calculations that are presented in this chapter for an actual experiment. Several aspects are considered. Firstly the implication of the low initial velocity that is used in the calculations. Secondly proper physical levels of ^{87}Rb atoms are chosen to fulfill the role of states $|1\rangle$ and $|2\rangle$. Subsequently we consider the implications of a real probability distribution of directions in which the spontaneously emitted photon is emitted. This distribution has been taken isotropic throughout this chapter. Finally we consider a method to detect the resulting final momentum distribution.

8.5.1   Computational limitations - experimental implications

The calculations presented in this chapter are for unrealistically low initial velocities v_i. This is because both calculation procedures turned out to be limited by computational resources. The calculation time becomes inconveniently long to evaluate the procedure for experimentally realistic incident velocities of ~ 30 cm/s [46], which corresponds to $\sim 50 v_{rec}$, with v_{rec} the recoil velocity of the atom due to the scattering of a photon.

For the time-independent approach the evaluation in *Mathematica* [140] of the Bessel-K functions of high imaginary order becomes very slow, even though these functions are analytically known. For the time-dependent approach the number of sampling points, necessary for the numerical evaluation, becomes too large due to the highly oscillatory character of the incident wave packet. However, we expect even better signals for realistic values for the initial velocity v_i, so the calculation represents a worst case.

8.5.2   Rb levels and optical pumping

So far we have considered levels $|1\rangle$ and $|2\rangle$ without discussing which physical level they correspond to. In reality we usually deal with multi-level atoms, that moreover include sub-structure. Each of these (sub-)levels has a different interaction with the evanescent field. If more (sub-)levels contribute to the signal the predicted interference can be washed out.

For ^{87}Rb atoms a convenient choice for state $|1\rangle$ would be the $|Fm\rangle = |1,0\rangle$ ground state and the $|Fm\rangle = |2,\pm 1\rangle$ ground states for the $|2\rangle$ state. The evanescent field needs to be linearly polarized and blue detuned with respect to the $F = 1 \rightarrow$

$F' = 2$ transition of either the D_1 or D_2 line. For this choice of parameters, atoms in state $|1\rangle$ can only make transitions to state $|2\rangle$. Transitions via the $F' = 0$ excited state can not decay to state $|2\rangle$, and hence do not contribute to the signal. Transitions via the $|F'm'\rangle = |1,0\rangle$ or $F' = 3$ excited stated are forbidden due to selection rules. Only a transition over the $|F'm'\rangle = |2,0\rangle$ excited state contributes to the transition from state $|1\rangle$ to state $|2\rangle$. This excited state can decay to either of the $|2,\pm1\rangle$ ground states. Since these states interact identically with the evanescent field, their interference patterns will overlap.

We performed experiments to observe the interference effects that are described in this chapter. Our attempts were hampered by the fact that the incident atoms were not optically pumped [90]. If interference was present it was obscured by the superposition of several of these interference patterns. Moreover the velocity spread of the sample of atoms might have been too large to observe interference.

8.5.3   Distribution of the spontaneously emitted photons

The distribution of wave vectors of the spontaneously emitted photon has been assumed isotropic throughout this chapter. In reality the polarization of the photon is either linear or circular, each having a corresponding wave-vector distribution.

The intensity distribution of a linearly polarized photon is given by $I(\theta) = \frac{3}{8\pi}\sin^2\theta$, with θ the angle with the z axis. This leads to a distribution of the z component of the wave vector of $\frac{3}{4}(1 - (k/k_0)^2)$. For a $\sigma^\pm$ circularly polarized photon the intensity distribution is given by $I(\theta) = \frac{3}{16\pi}(1 + \cos^2\theta)$, which leads to a distribution of the z component of the wave vector of $\frac{3}{8}(1 + (k/k_0)^2)$. For the intensity distributions, see e.g. [47].

From these distributions it is clear that a linearly polarized spontaneously emitted photon is advantageous in order to maximize the visibility of the interference pattern, since the components for small $|k|$ contribute more than the components for larger $|k|$. However, as discussed in the previous sub-section, for ^{87}Rb atoms the spontaneously emitted photon needs to be either σ^+ or σ^- polarized. This will lead to a decrease of the interference visibility as compared to the graphs calculated in the previous two sections. However, it will still be possible to observe interference.

8.5.4   Detection

In an actual experiment the momentum distribution eventually maps on the position distribution since the decay length of the evanescent wave κ^{-1} is short with respect to the height of the motional turning point due to gravity. One way to perform this experiment is similar to the inelastic bouncing experiments [46]. The velocity distribution can be determined from e.g. an absorption image of the sample of atoms at a sufficiently long time after the reflection.

Another possibility is to perform a beam experiment with an atomic beam incident at a grazing angle with respect to the dielectric surface that is used to create the evanescent wave. The velocity component of the atoms parallel to the surface will not be altered, while the velocity component perpendicular to the surface will

show the interference as discussed in this chapter. A spatially resolving detector down the path of the atomic beam will show the interference patterns. This setup has the advantage of being a continuous experiment, which will enhance the signal to noise ratio.

8.6   Discussion and conclusions

By solving the Schrödinger equation numerically we have been able to answer the question "Is it possible to have an atom interferometer on basis of beam splitters that involve spontaneous emission?" with an unambiguous yes.

The intuitive objections to whether this is possible have been refuted. The semi-classical arguments that were presented in section 8.2 have been confirmed by the full quantum-mechanical calculations. "Which way" information due to the possibility of detecting the spontaneously emitted photon can be prevented by choosing a sufficiently narrow velocity uncertainty. A wave packet can cover both transfer points in phase space simultaneously if its velocity is defined accurately enough. The incoherent nature of a spontaneous emission process due to the random recoil direction of the atom is visible in all the calculated interference curves, but does not lead to a complete scrambling of the interference. For larger final velocities, for which the transfer points are separated more and the acquired random phase is consequently larger, the visibility of the interference fringes indeed decreases. Furthermore the fringe period indeed qualitatively shows the behavior that was predicted on the basis of the semi-classical calculations.

References

[1]   S. Chu, *The manipulation of neutral particles*, Rev. Mod. Phys. **70**, 685 (1998).

[2]   E.L. Raab, M. Prentiss, A. Cable, S. Chu, and D.E. Pritchard, *Trapping of neutral sodium atoms with radiation pressure*, Phys. Rev. Lett, **59**, 2631 (1987).

[3]   C.N. Cohen-Tannoudji, *Manipulating atoms with photons*, Rev. Mod. Phys. **70**, 707 (1998).

[4]   W.D. Phillips, *Laser cooling and trapping of neutral atoms*, Rev. Mod. Phys. **70**, 721 (1998).

[5]   D.-J. Han, S. Wolf, S. Oliver, C. McCormick, M.T. DePue, and D.S. Weiss, *3D Raman sideband cooling of cesium atoms at high density*, Phys. Rev. Lett. **85**, 724 (2000).

[6]   T. Ido, Y. Isoya, and H. Katori, *Optical-dipole trapping of Sr atoms at a high phase-space density*, Phys. Rev. A **61**, 061403(R) (2000).

[7]   R.J. Cook, and R.K. Hill, *An electromagnetic mirror for neutral atoms*, Opt. Comm. **43**, 258 (1982).

[8]   V.I. Balykin, V.S. Letokov, Yu.B. Ovchinikov, and A.I. Sirorov, *Reflection of an atomic beam from a gradient of an optical field*, Pis'ma Zh. Eksp. Teor. Fiz. **45**, 282 (1987) [JETP Lett. **45**, 353 (1987)].

[9]   M.A. Kasevich, D.S. Weiss, and S. Chu, *Normal-incidence reflection of slow atoms from an optical evanescent wave*, Opt. Lett. **15**, 607 (1990).

[10]   D.V. Laryushin, Yu.B. Ovchinikov, V.I. Balykin, and V.S. Letokov, *Reflection cooling of sodium atoms in an evanescent light wave*, Opt. Comm. **135**, 138 (1997). [Pis'ma Zh. Eksp. Teor. Fiz. **62**, 102 (1995).]

[11]   Yu. B. Ovchinnikov, I. Manek, and R. Grimm, *Surface trap for Cs atoms based on evanescent-wave cooling*, Phys. Rev. Lett. **79**, 2225 (1997).

[12]   Yu.B. Ovchinnikov, S.V. Shul'ga, and V.I. Balykin, *An atomic trap based on evanescent light waves*, J. Phys. B: At. Mol. Opt. Phys. **24**, 3173 (1991).

[13]   M. Hammes, D. Rychtarik, B. Engeser, H.-C. Nägerl, and R. Grimm, *Evanescent-wave trapping and evaporative cooling of an atomic gas at the crossover to two dimensions*, Phys. Rev. Lett. **90**, 173001 (2003).

[14]   A. Aspect, R. Kaiser, N. Vansteenkiste, P. Vignolo, and C.I. Westbrook, *Nondestructive detection of atoms bouncing on an evanescent wave*, Phys. Rev. A **52**, 4704 (1995).

[15]   R.A. Cornelussen, A.H. van Amerongen, B.T. Wolschrijn, R.J.C. Spreeuw, and H.B. van Linden van den Heuvell, *Cold trapped atoms detected with evanescent waves*, Eur. Phys. J. D **21**, 347 (2002).

[16] V.V. Ivanov, R.A. Cornelussen, R.J.C. Spreeuw, and H.B. van Linden van den Heuvell, *Observed modified radiative properties of cold atoms in vacuum near a dielectric surface*, J. Opt. B: Quantum Semiclass. Opt. **6**, 454 (2004).

[17] S. Bose, *Plancks Gesetz und Lichtquantenhypothese.*, Z. Phys. **26**, 178 (1924).

[18] A. Einstein, *Quantentheorie des einatomigen idealen Gases*, Sitzungsber. Kgl. Preuss. Akad. Wiss. 261 (1924).

[19] A. Einstein, *Quantentheorie des einatomigen idealen Gases: Zweite Abhandlung*, Sitzungsber. Kgl. Preuss. Akad. Wiss. 3 (1925).

[20] R. J. C. Spreeuw, D. Voigt, B. T. Wolschrijn, and H. B. van Linden van den Heuvell, *Creating a low-dimensional quantum gas using dark states in an inelastic evanescent-wave mirror*, Phys. Rev. A **61**, 053604 (2000).

[21] H. Gauck, M. Hartl, D. Schneble, H. Schnitzler, T. Pfau, and J. Mlynek, *Quasi-2D Gas of laser cooled atoms in a planar matter waveguide*, Phys. Rev. Lett. **81**, 5298 (1998).

[22] R.J.C. Spreeuw, T. Pfau, U. Janicke, and M. Wilkens, *Laser-like scheme for atomic-matter waves*, Eur. Phys. Lett. **32**, 469 (1995).

[23] S. Inouye, T. Pfau, S. Gupta, A. P. Chikkatur, A. Görlitz, D. E. Pritchard, and W. Ketterle, *Phase-coherent amplification of atomic matter waves*, Nature **402**, 641 (1999).

[24] M.H. Anderson, J.R. Ensher, M.R. Matthews, C.E. Wieman, and E.A. Cornell, *Observation of Bose-Einstein condensation in a dilute atomic vapor*, Science **269**, 198 (1995).

[25] K.B. Davis, M.-O. Mewes, M.R. Andrews, N.J. van Druten, D.S. Durfee, D.M. Kurn, and W. Ketterle, *Bose-Einstein condensation in a gas of sodium atoms*, Phys. Rev. Lett. **75**, 3969 (1995).

[26] C.C. Bradley, C.A. Sackett, and R.G. Hulet, *Bose-Einstein condensation of lithium: observation of limited condensate number*, Phys. Rev. Lett. **78**, 985 (1997).

[27] C.C. Bradley, C.A. Sackett, J.J. Tollett, and R.G. Hulet, *Evidence of Bose-Einstein condensation in an atomic gas with attractive interactions*, Phys. Rev. Lett. **75**, 1687 (1995).

[28] M.-O. Mewes, M.R. Andrews, D.M. Kurn, D.S. Durfee, C.G. Townsend, and W. Ketterle, *Outcoupler for Bose-Einstein condensed atoms*, Phys. Rev. Lett. **78**, 582 (1997).

[29] M. R. Andrews, C. G. Townsend, H.-J. Miesner, D. S. Durfee, D. M. Kurn, and W. Ketterle, *Observation of interference between two Bose condensates*, Science **275**, 637 (1997).

[30] B.P. Anderson, and M.A. Kasevich, *Macroscopic quantum interference from atomic tunnel arrays*, Science **282**, 1686 (1998).

[31] I. Bloch, T.W. Hänsch, and T. Esslinger, *Atom laser with a cw output coupler*, Phys. Rev. Lett. **82**, 3008 (1999).

[32] E.W. Hagley, L. Deng, M. Kozuma, J. Wen, K. Helmerson, S.L. Rolston, and W.D. Phillips, *A well collimated quasi-continuous atom laser*, Science **283**, 1706 (1999).

[33] E.A. Cornell, and C.E. Wieman, *Nobel lecture: Bose-Einstein condensation in a dilute gas, the first 70 years and some recent experiments*, Rev. Mod. Phys. **74**, 875 (2002).

[34] W. Ketterle, *Nobel lecture: When atoms behave as waves: Bose-Einstein condensation and the atom laser*, Rev. Mod. Phys. **74**, 1131 (2002).

[35] S. Jochim, M. Bartenstein, A. Altmeyer, G. Hendl, S.C. Chin, J. Hecker Denschlag, and R. Grimm, *Bose-Einstein Condensation of molecules*, Science **302**, 2101 (2003).

[36] M. Greiner, C.A. Regal, and D.S. Jin, *Emergence of a molecular Bose-Einstein condensate from a Fermi gas*, Nature **426**, 539 (2003).

[37] S. Dürr, T. Volz, A. Marte, and G. Rempe, *Observation of molecules produced from a Bose-Einstein condensate*, Phys. Rev. Lett. **92**, 020406 (2004).

[38] W. Hänsel, P. Hommelhoff, T.W. Hänsch, and J. Reichel, *Bose-Einstein condensation on a microelectronic chip*, Nature **413**, 498 (2001).

[39] H. Ott, J. Fortagh, G. Schlotterbeck, A. Grossmann, and C. Zimmermann, *Bose-Einstein condensation in a surface microtrap*, Phys. Rev. Lett. **87**, 230401 (2001).

[40] M.D. Barrett, J.A. Sauer, and M.S. Chapman, *All-optical formation of an atomic Bose-Einstein condensate*, Phys. Rev. Lett. **87**, 010404 (2001).

[41] G. Cennini, G. Ritt, C. Geckeler, and M. Weits, *Bose-Einstein condensation in a CO_2-laser dipole trap*, Appl. Phys. B **77**, 773 (2003).

[42] Y. Colombe, D. Kadio, M. Olshanii, B. Mercier, V. Lorent, and H. Perrin, *Schemes for loading a Bose-Einstein condensate into a two-dimensional dipole trap*, J. Opt. B: Quantum Semiclass. Opt. **5**, S155 (2003).

[43] D. Rychtarik, B. Engeser, H.-C. Nägerl, and R. Grimm, *Two-dimensional Bose-Einstein condensate in an optical surface trap*, Phys. Rev. Lett. **92**, 173003 (2004).

[44] M. Hammes, D. Rychtarik, H.-C. Nägerl, and R. Grimm, *Cold-atom gas at very high densities in an optical surface microtrap*, Phys. Rev. A **66**, 051401(R) (2002).

[45] H. Wiseman, and M. Collett, *An atom laser based on dark-state cooling*, Phys. Lett. A **202**, 246 (1995).

[46] B.T. Wolschrijn, D. Voigt, R. Janssen, R.A. Cornelussen, N. Bhattacharya, R.J.C. Spreeuw, and H.B. van Linden van den Heuvell, *Stochastic rainbow caustic observed with cold atoms*, Phys. Rev. A **64**, 065403 (2001).

[47] J.D. Jackson, *Classical electrodynamics*, 3rd edition, (John Wiley & Sons, 1999).

[48] M. Born, and E. Wolf, *Principles of optics*, (Pergamon press, 1959).

[49]   F.L. Pedrotti, and L.S. Pedrotti, *Introduction to optics*, 2nd edition, (Prentice-Hall international editions, 1993).

[50]   E. Hecht, and A. Zajac, *Optics*, (Addison-Wesley publishing company, 1974).

[51]   C. Cohen-Tannoudji, J. Dupont-Roc, and G. Grynberg, *Atom-photon interactions*, (John Wiley& Sons, 1998).

[52]   I.I. Sobelman, *Atomic spectra and radiative transitions*, (Springer-Verlag, 1977).

[53]   M. Weisbluth, *Atoms and molecules*, (Academic Press, 1978).

[54]   R.N. Zare, *Angular momentum - understanding spatial aspects in chemistry and physics*, (John Wiley & Sons, 1988).

[55]   H.J. Metcalf, and P. van der Straten, *Laser cooling and trapping*, (Springer, 1999).

[56]   D.R. Lide (ed.), *CRC handbook of chemistry and physics*, 81st ed. (CRC press, Boca Raton, 2000).

[57]   D.A. Steck, *Rubidium 87 D line data*, `http://steck.us/alkalidata` (2001).

[58]   J.-Y. Courtois, J.-M. Courty, and J.C. Mertz, *Internal dynamics of multilevel atoms near a vacuum-dielectric interface*, Phys. Rev. A **58**, 1862 (1996).

[59]   A. Landragin, J.-Y. Courtois, G. Labeyrie, N. Vansteenkiste, C.I. Westbrook, and A. Aspect, *Measurement of the van der Waals force in an atomic mirror*, Phys. Rev. A **77**, 1464 (1996).

[60]   D. Voigt, B.T. Wolschrijn, R.A. Cornelussen, R. Jansen, N. Bhattacharya, H.B. van Linden van den Heuvell, and R.J.C. Spreeuw, *Elastic and inelastic evanescent-wave mirrors for cold atoms*, Comptes Rendus de l'Académie des Sciences - Série IV- Physique **t. 2**, 619 (2001).

[61]   A. Banerjee, D. Das, and V. Natarajan, *Precise fine-structure and hyperfine-structure measurements in Rb*, arXiv:physics/0209019 (2002).

[62]   J. Ye, S. Swartz, P. Jungner, and J.L. Hall, *Hyperfine structure and absolute frequency of the ^{87}Rb $5P_{3/2}$ state*, Opt. Lett. **21**, 1280 (1996).

[63]   U. Volz, and H. Schmoranzer, *Precision lifetime measurements on alkali atoms and on helium by beam-gas-laser spectroscopy*, Physica Scripta **T65**, 48 (1996).

[64]   S. Bize, Y. Sortais, M.S. Santos, C. Mandache, A. Clairon, and C. Salomon, *High-accuracy measurement of the ^{87}Rb ground-state hyperfine splitting in an atomic fountain*, Europhys. Lett. **45**, 558 (1999).

[65]   G.P. Barwood, P. Gill, and W.R.C. Rowley, *Frequency measurements on optically narrowed Rb-stabilised laser diodes at 780 nm and 795 nm*, Appl. Phys. B **53**, 142 (1991).

[66]   G. Cennini, G. Ritt, C. Geckeler, and M. Weitz, *All-optical realization of an atom laser*, Phys. Rev. Lett. **91**, 240408 (2003).

[67] T. Takekoshi, J.R. Yeh, and R.J. Knize, *Quasi-electrostatic trap for neutral atoms*, Opt. Comm. **114**, 421 (1995).

[68] Y. Takasu, K. Maki, K. Komori, T. Takano, K. Honda, M. Kumakura, T. Yabuzaki, and Y. Takahashi, *Spin-singlet Bose-Einstein condensation of two-electron atoms*, Phys. Rev. Lett. **91**, 040404 (2003).

[69] T. Weber, J. Herbig, M. Mark, H.-C. Nägerl, and R. Grimm, *Bose-Einstein condensation of cesium*, Science **299**, 232 (2003).

[70] S.R. Granade, M.E. Gehm, K.M. O'Hara, and J.E. Thomas, *All-optical production of a degenerate Fermi gas*, Phys. Rev. Lett. **88**, 120405 (2002).

[71] C.S. Adams, H.J. Lee, N. Davidson, M. Kasevich, and S. Chu, *Evaporative cooling in a crossed dipole trap*, Phys. Rev. A **74**, 3577 (1995).

[72] S.J.M. Kuppens, K.L. Corwin, K.W. Miller, T.E. Chupp, and C.E. Wieman, *Loading an optical dipole trap*, Phys. Rev. A **62**, 013406 (2000).

[73] D. M. Stamper-Kurn, H.-J. Miesner, A. P. Chikkatur, S. Inouye, J. Stenger, and W. Ketterle, *Reversible Formation of a Bose-Einstein Condensate*, Phys. Rev. Lett. **81**, 2194 (1998).

[74] Y. Takasu, K. Honda, K. Komori, T. Kuwamoto, M. Kumakura, Y. Takahashi, and T. Yabuzaki, *High-density trapping of cold ytterbium atoms by an optical dipole force*, Phys. Rev. Lett. **90**, 023003 (2003).

[75] S. Friebel, R. Scheunemann, J. Walz, T.W. Hänsch, and M. Weitz, *Laser cooling in a CO_2-laser optical lattice*, Appl. Phys. B **67**, 699 (1998).

[76] K.D. Bonin, and M.A. Kadar-Kallen, *Theory of the light force technique for measuring polarizabilities*, Phys. Rev. A **47**, 944 (1993).

[77] K.D. Bonin, and M.A. Kadar-Kallen, *Linear electric-dipole polarizabilities*, Int. J. Mod. Phys. B **8**, 3313 (1994).

[78] J.R.P. Angel, and P.G.H. Sandars, *The hyperfine structure Stark effect. I. Theory*, Proc. Roy. Soc. London A **305**, 125 (1968).

[79] A. Khadjavi, A. Lurio, and W. Happer, *Stark effect in the excited states of Rb, Cs, Cd, and Hg***, Phys. Rev. **167**, 128 (1968).

[80] T.M. Miller, and B. Bederson, *Atomic and molecular polarizabilities - a review of recent advances*, Adv. At. Mol. Phys. **13**, 1 (1977).

[81] C. Krenn, W. Scherf, O. Khait, M. Musso, and L. Windholz, *Stark effect investigations of resonance lines of neutral potassium, rubidium, europium and gallium*, Z. Phys. D **41**, 229 (1997).

[82] M.S. Safronova, C.J. Williams, and C.W. Clark, *Optimizing the fast Rydberg quantum gate*, Phys. Rev. A **67**, 040303(R) (2003).

[83] M.S. Safronova, C.J. Williams, and C.W. Clark, *Relativistic many-body calculations of electric dipole matrix elements, lifetimes and polarizabilities in rubidium.*, Phys. Rev. A **69**, 022509 (2004).

[84] W.C. Martin, J.R. Fuhr, D.E. Kelleher, A. Musgrove, L. Podobedova, J. Reader, E.B. Saloman, C.J. Sansonetti, W.L. Wiese, P.J. Mohr, and K. Olsen *NIST Atomic Spectra Database (version 2.0)*,

http://physics.nist.gov/asd, (National Institute of Standards and Technology, Gaithersburg, MD, 1999).

[85] A.A. Radzig, and B.M. Smirnov, *Reference data on atoms, molecules, and ions*, (Springer-Verlag, 1985).

[86] W.R. Johnson, D. Kolb, and K.-N. Huang, *Electric-dipole, quadrupole, and magnetic-dipole susceptibilities and shielding factors for closed-shell ions of the He, Ne, Ar, Ni (Cu^+), Kr, Pb, and Xe isoelectronic sequences*, Atomic data and nuclear data tables **28**, 333 (1983).

[87] R.W. Molof, H.L. Schwartz, T.M. Miller, and B. Bederson, *Measurements of electric dipole polarizabilities of the alkali-metal atoms and the metastable noble-gas atoms*, Phys. Rev. A **10**, 1131 (1974).

[88] K.E. Miller, D. Krause, Jr., and L.R. Hunter, *Precise measurements of the Stark shift of the rubidium and potassium D_1 lines*, Phys. Rev. A **49**, 5128 (1994).

[89] D. Voigt, *Evanescent-wave mirrors for cold atoms*, Ph.D. thesis, University of Amsterdam (2000, unpublished).

[90] B.T. Wolschrijn, *Inelastic bouncing and optical trapping of cold atoms*, Ph.D. thesis, University of Amsterdam (2001, unpublished).

[91] C.E. Wieman, and L. Hollberg, *Using diode lasers for atomic physics*, Rev. Sci. Instr. **62**, 1 (1991).

[92] K.B. MacAdam, A. Steinbach, and C. Wieman, *A narrow band tunable diode laser system with grating feedback, and a saturated absorption spectrometer for Cs and Rb*, Am. J. Phys. **60**, 1098 (1992).

[93] L. Ricca, M. Weidemüller, T. Esslinger, A. Hemmerich, C. Zimmermann, V. Vuletic, W. König, and T.W. Hänsch, *A compact grating-stabilized diode laser system for atomic physics*, Opt. Comm. **117**, 541 (1995).

[94] G.C. Bjorklund, *Frequency-modulation spectroscopy: a new method for measuring weak absorptions and dispersions*, Opt. Lett. **5**, 15 (1980).

[95] G.C. Bjorklund, M.D.Levenson, W. Lenth, and C. Ortiz, *Frequency modulation (FM) spectroscopy*, Appl. Phys. B **32**, 145 (1983).

[96] W. Ketterle, D.S. Durfee, and D.M. Stamper-Kurn, *Making, probing and understanding Bose-Einstein condensates*, in *Proceedings of the International School of Physics 'Enrico Fermi'. Bose-Einstein condensation in atomic gases*, ed. by M. Inguscia, S. Stringari, and C.E. Wieman (IOS Press, Amsterdam, 1999). also published at arXiv: cond-mat/9904034.

[97] C. Wieman, G. Flowers, and S. Gilbert, *Inexpensive laser cooling and trapping experiment for undergraduate laboratories*, Am. J. Phys **63**, 317 (1995).

[98] J. Fortagh, A. Grossmann, T.W. Hänsch, and C. Zimmerman, *Fast loading of a magneto-optical trap from a pulsed thermal source*, J. Appl. Phys. **84**, 6499 (1998).

[99]   K.L. Moore, T.P. Purdy, K.W. Murch, S. Leslie, S. Gupta, and D.M. Stamper-Kurn, *Collimated, single-pass atom source from a pulsed alkali metal dispenser for laser-cooling experiments*, arXiv:physics/0409011 (2004).

[100]   R.A. Cornelussen, T.N. Huussen, R.J.C. Spreeuw, and H.B. van Linden van den Heuvell, *Power-efficient frequency switching of a locked laser*, Appl. Phys. B **78**, 19 (2004).

[101]   E. Gehrig, B. Beier, K.-J. Boller, and R. Wallenstein, *Experimental characterization and numerical modelling of an AlGaAs oscillator broad area double pass amplifier system*, Appl. Phys. B **66**, 287 (1998).

[102]   I. Shvarchuck, K. Dieckmann, M. Zielonkowski, and J.T.M. Walraven, *Broad-area diode-laser system for a rubidium Bose-Einstein condensation experiment*, Appl. Phys. B **61**, 475 (2000).

[103]   D. Voigt, E.C. Schilder, R.J.C. Spreeuw, and H.B. van Linden van den Heuvell, *Characterization of a high-power tapered semiconductor amplifier system*, Appl. Phys. B **72**, 279 (2001).

[104]   G.R. Hadley, *Injection locking of diode lasers*, IEEE J. Quantum Electr. **QE-22**, 419 (1986).

[105]   P. Spano, S. Piazzolla, and M. Tamburrini, *Frequency and intensity noise in injection-locked semiconductor lasers: theory and experiments*, IEEE J. Quantum Electr. **QE-22**, 427 (1986).

[106]   U. Schünemann, H. Engler, M. Zielonkowski, M. Weidemüller, and R. Grimm, *Magneto-optic trapping of lithium using semiconductor lasers*, Opt. Comm. **158**, 263 (1998).

[107]   W. Hänsel, J. Reichel, P. Hommelhoff, and T.W. Hänsch, *Magnetic conveyor belt for transporting and merging trapped atom clouds*, Phys. Rev. Lett. **86**, 608 (2001).

[108]   D. Müller, E.A. Cornell, M. Prevedelli, P. Schwindt, A. Zozulya, and D. Anderson, *A waveguide atom beamsplitter for laser-cooled neutral atoms*, Opt. Lett. **25**, 1382 (2000).

[109]   D. Cassettari, B. Hessmo, R. Folman, T. Maier, and J. Schmiedmayer, *Beam Splitter for Guided Atoms*, Phys. Rev. Lett. **85**, 5483 (2000).

[110]   K. Kiersnowski, L. Józefowski, and T. Dohnlik, *Effective optical anisotropy in evanescent wave propagation in atomic vapor*, Phys. Rev. A **57**, 4079(R) (1998).

[111]   K. Zhao, Z. Wu, and H.M. Lai, *Optical determination of alkali metal vapor number density in the vicinity ($\sim 10^{-5}$ cm) of cell surfaces*, J. Opt. Soc. Am. B **18**, 1904 (2001).

[112]   F. Goos, and H. Hänchen, *Ein neuer und fundamentaler Versuch zur Totalreflexion*, Ann. Phys. Lpz. **1**, 333 (1947).

[113]   C. Chiu Chan, and T. Tamir, *Beam phenomena at and near critical incidence upon a dielectric interface*, J. Opt. Soc. Am. A **4**, 655 (1987).

[114] F.I. Baida, D. van Labeke, and J.-M. Vigoureux, *Numerical study of the displacement of a three-dimensional Gaussian beam transmitted at total internal reflection. Near-field applications*, J. Opt. Soc. Am. A **17**, 858 (2000).

[115] D. Voigt, B.T. Wolschrijn, N. Bhattacharya, R.J.C. Spreeuw, and H.B. van Linden van den Heuvell, *Observation of radiation pressure exerted by evanescent waves*, Phys. Rev. A **61**, 063412 (2000).

[116] An up to date list of atomic physics groups can be found on `http://www.uibk.ac.at/c/c7/c704/ultracold/atomtraps.html`, many of them are working on BEC experiments.

[117] B. DeMarco, and D.S. Jin, *Onset of Fermi degeneracy in a trapped atomic gas*, Science **285**, 1703 (1999).

[118] A.G. Truscott, K.E. Strecker, W.I. McAlexander, G.B. Partridge, R.G. Hulet, *Observation of Fermi pressure in a gas of trapped atoms*, Science **291**, 2570 (2001).

[119] C.A. Regal, M. Greiner, and D.S. Jin, *Observation of resonance condensation of fermionic atom pairs*, Phys. Rev. Lett. **92**, 040403 (2004).

[120] C. Chin, M. Bartenstein, A. Altmeyer, S. Riedl, S. Jochim, J. Hecker Denschlag, and R. Grimm, *Observation of the pairing gap in a strongly interacting Fermi gas*, Science **305**, 1128 (2004).

[121] E.A. Hinds, and I.G. Hughes, *Magnetic atom optics: mirrors, guides, traps, and chips for atoms*, J. Phys. D: Appl. Phys. **32**, R119 (1999).

[122] S. Eriksson, F. Ramirez-Martinez, E.A. Curtis, B.E. Sauer, P.W. Nutter, E.W. Hill, and E.A. Hinds, *Micron-sized atom traps made from magneto-optical thin films*, arXiv: cond-mat/0406482 (2004).

[123] D.S. Petrov, M. Holzmann, G.V. Shlyapnikov, *Bose-Einstein condensation in quasi-2D trapped gases*, Phys. Rev. Lett. **84**, 2551 (2000).

[124] D.S. Petrov, G.V. Shlyapnikov, and J.T.M. Walraven, *Regimes of quantum degeneracy in trapped 1D gases*, Phys. Rev. Lett. **85**, 3745 (2000).

[125] A. Görlitz, J.M. Vogels, A.E. Leanhardt, C. Raman, T.L. Gustavson, J.R. Abo-Shaeer, A.P. Chikkatur, S. Gupta, S. Inouye, T. Rosenband, and W. Ketterle, *Realization of Bose-Einstein condensates in lower dimensions*, Phys. Rev. Lett. **87**, 130402 (2001).

[126] F. Schreck, L. Khaykovich, K.L. Corwin, G. Ferrari, T. Bourdel, J. Cubizolles, and C. Salomon, *Quasipure Bose-Einstein condensate immersed in a Fermi sea*, Phys. Rev. Lett. **87**, 080403 (2001).

[127] B. Paredes, A. Widera, V. Murg, O. Mandel, S. Fölling, I. Cirac, G.V. Shlyapnikov, T.W. Hänsch, and I. Bloch, *Tonks-Girardeau gas of ultracold atoms in an optical lattice*, Nature **429**, 277 (2004).

[128] Yu.B. Ovchinnikov, J. Söding, and R. Grimm, *Cooling atoms in dark gravitational laser traps*, JETP Lett. **61**, 21 (1995).

[129] J. Söding , R. Grimm, and Yu.B. Ovchinnikov, *Gravitational laser trap for atoms with evanescent wave cooling*, Opt. Comm. **119**, 652 (1995).

[130]   D. Voigt, private communication.

[131]   L. Cognet, V. Savalli, G.Zs.K. Horvath, D. Holleville, R. Marani, N. West-brook, C.I. Westbrook, and A. Aspect, *Atomic interference in grazing incidence diffraction from an evanescent wave mirror*, Phys. Rev. Lett. **81**, 5044 (1998).

[132]   R. Loudon, *The quantum theory of light*, 2nd edition (Clarendon Press, 1983).

[133]   U. Eichmann, J.C. Bergquist, J.J. Bollinger, J.M. Gilligan, W.M. Itano, D.J. Wineland, and M.G. Raizen, *Young's interference experiment with light scattered from two atoms*, Phys. Rev. Lett. **70**, 2359 (1993).

[134]   R.A. Cline, J.D. Miller, M.R. Matthews, and D.J. Heinzen, *Spin relaxation of optically trapped atoms by light scattering*, Opt. Lett. **19**, 207 (1994).

[135]   C. Kurtsiefer, O. Dross, D. Voigt, C.R. Ekstrom, T. Pfau, and J. Mlynek, *Observation of correlated atom-photon pairs on the single-particle level*, Phys. Rev. A **55**, 2539 (1997).

[136]   C. Henkel, J.-Y. Courtois, R. Kaiser, C. Westbrook, and A. Aspect, *Phase shifts of atomic de Broglie waves at an evanescent wave mirror*, Laser Physics **4**, 1042 (1994).

[137]   M. Abramowitz, and I.A. Stegun (eds.) *Handbook of mathematical functions*, 9th edition, (Dover publications, 1972).

[138]   J. Dalibard, Y. Castin, and K. Mølmer, *Wave-function approach to dissipative processes in quantum optics*, Phys. Rev. Lett. **68**, 580 (1992).

[139]   K. Mømer, Y. Castin, and J. Dalibard, *Monte Carlo wave-function method in quantum optics*, J. Opt. Soc. Am. B **10**, 524 (1993).

[140]   S. Wolfram, *Mathematica© 5*, (Wolfram research, 2003).

[141]   M. Liebmann, and B. Thaller, *Quantum kernel* (1998), distributed with B. Thaller, *Visual quantum mechanics* (Springer-Verlag, 2000), or available at `http://www.kfunigraz.ac.at/imawww/vqm/pages/dlschroed.html`.

Summary

This thesis describes our efforts to exploit the unique properties of evanescent waves in the field of cold atoms. We have demonstrated detection of cold atoms in close proximity of a dielectric surface. Other efforts were focussed to obtain a sample of atoms with high phase-space density in a completely optical way, without using evaporative cooling.

In chapter 2 we described the theoretical background that is needed for the rest of the thesis. Light, and especially evanescent light, is described. We extend the concept of light intensity to an effective light intensity which is also applicable for evanescent waves. The interaction of atoms with light is described, both for near-resonant and far off-resonant radiation. This is applied to the case of ^{87}Rb atoms. Some attention is paid to the Van der Waals interaction of atoms with a dielectric surface.

Chapter 3 discussed a slightly different subject. In the literature it is claimed that the success of Bose-Einstein condensation in dipole traps of a CO_2 laser is due to the sign of the polarizability of the excited state that is used in the laser cooling process. We have calculated the level shifts of the ground and excited state for radiation with wavelengths higher than 700 nm. Based on these calculations we found that the level shifts have the same sign as the DC value for wavelengths between 1366 nm and approximately 1400 nm and for wavelengths larger than 1529 nm. The magnitude of the light shift and the current day availability of high power and single spatial mode cw lasers lead to the conclusion that a laser with a wavelength of 2 μm is a promising alternative for a CO_2 laser.

The experimental setup that is used to perform the experiments is described in chapter 4. The laser beams that are used in the experiment are discussed. For beams that create evanescent waves, a very accurate method to determine the angle of incidence with respect to the critical angle is discussed. An accuracy below the diffraction limit was obtained. The components of the vacuum setup are discussed. In particular the quartz cell that provides the optical access for the experiments, the custom made prism that is used to create the various evanescent fields for the experiments and the dispenser that is used to get a low Rb vapor in the vacuum system are discussed in detail.

It is often necessary to quickly change a laser frequency during the experiment. This is convenient to, e.g. switch between a frequency needed for magneto-optic trapping to a frequency needed for polarization gradient cooling. In chapter 5 a method is discussed to perform this task very efficiently. Its effect is demonstrated using a diode laser system. The laser frequency is changed by changing the laser current, while this change is compensated by an AOM for the light that is used for spectroscopy. This way the laser will stay in lock even for very fast changes of the

frequency.

In chapter 6 we demonstrate a method to *in situ* detect atoms very close ($\sim \lambda$) to a dielectric surface. We measure the absorption of a weak, resonant evanescent wave in order to detect atoms that are present in the volume of the evanescent wave. The method was tested by detecting the absorption of atoms falling onto the surface. In order to qualitatively understand the absorption of the evanescent wave for angles of incidence very close to the critical angle, the Gaussian character of the incident beam had to be taken into account. We also demonstrated loading of only a few potential minima of a standing-wave dipole trap by making use of the highly localized scattering of an evanescent-wave mirror. We used the evanescent probing technique to determine the number of trapped atoms. We determined that we have trapped more than 1.5×10^4 atoms initially. We infer a density increase of two orders of magnitude.

Chapter 7 presents a numerical analysis of an evanescent-wave dark-state trap. Several trap geometries were discussed. For a geometry of two nearly co-propagating incident beams a more detailed analysis was performed. We optimized the experimental parameters within realistic limits for a large trapping fraction and a low scattering rate. We concluded that a trapping fraction of 10% could be realized, which leads to a density increase of a factor 130 and a phase-space density increase of a factor 75 with respect to the MOT values. Because scattering even a single photon is very likely to lead to loss from the trap, the life time of this trap is its weak point. The realization of this experiment was prevented by the inferior quality of the surface of the prism that was used to create the evanescent fields.

As an example of the unexpected possibilities of the combination of cold atoms and evanescent wave potentials may serve chapter 8. Atoms that reflect inelastically from an evanescent-wave mirror are transferred to a different internal state during the reflection from the potential. This transition can occur on the ingoing or the outgoing part of the trajectory. By numerically solving the Schrödinger equation we have shown that it is possible to observe interference between these two trajectories even though the transfer process is a spontaneous Raman transition, which is intuitively an incoherent process. This is possible if the initial velocity of the wave packet is well defined. The atoms then follow a trajectory that closely resembles a classical trajectory through phase space, but the wave packet is spread out along this trajectory such that both transfer points are covered simultaneously. This prevents knowledge of "which way" information by detecting the spontaneously emitted photon. The random direction of the recoil does not lead to a complete scrambling of the interference.

Samenvatting

De afgelopen jaren is mij vaak gevraagd om uit te leggen wat mijn onderzoek eigenlijk inhoudt. Deze uitleg heb ik met wisselend succes gegeven. De reden hiervoor is, denk ik, duidelijk als je door dit proefschrift heen bladert. Aan de ene kant is wiskunde de taal waarmee veel effecten het makkelijkst worden beschreven. Een poging om dit in *gewoon Nederlands* te doen strandt al snel in een warrig verhaal. Warrig doordat het moeilijk en misschien zelfs onmogelijk is om alle subtiele effecten die in de formules verstopt zitten in gewoon Nederlands te vertellen. Aan de andere kant staan de effecten die ik heb onderzocht ver van het leven van alledag. Weinig mensen kunnen zich er iets bij voorstellen.

Toch wil ik, nu ik het in alle rust kan opschrijven, nog een poging doen. Om een helder verhaal te krijgen zal ik veel subtiliteiten moeten weglaten. Iemand die hierin geïnteresseerd is raad ik aan om toch maar dit proefschrift door te lezen. En vragen stellen kan natuurlijk altijd.

Lichtkracht Normaal gesproken merk je het niet, maar licht oefent een kracht uit op materie. De kracht die het licht van de zon op jou uitoefent is te vergelijken met de kracht van een snipper confetti die op je ligt. Een voorbeeld van deze lichtkracht is de staart van een komeet. Deze staart staat niet, zoals veel mensen denken, langs de baan van de komeet, maar hij staat altijd van de zon af. Hij bestaat uit stofdeeltjes van de komeet die door het licht van de zon worden weggeduwd. In figuur S.1 is een foto te zien van komeet Hale-Bopp toen hij in 1997 door ons zonnestelsel vloog. De staart van de komeet is duidelijk te zien.

De experimenten die beschreven zijn in dit proefschrift zijn gedaan met rubidium-atomen. Op deze atomen oefent het licht een veel grotere kracht uit. Deze kracht kan zo groot zijn als 10.000 keer de zwaartekracht! Dit is mogelijk door gebruik te maken van een eigenschap van deze atomen; ze zijn bijzonder gevoelig voor een bepaalde kleur van het licht. Dat bepaalde atomen een voorkeur hebben voor een bepaalde kleur licht is bijvoorbeeld te zien aan natrium-atomen. Natriumlampen, de gele lampen boven de snelweg, hebben een heel specifieke gele kleur. Deze kleur is ook te zien als je keukenzout (ofwel natrium-chloride) in vuur gooit. De rubidium-atomen die wij gebruiken in onze experimenten zijn in veel opzichten vergelijkbaar met natrium-atomen, maar de speciale kleur van rubidium-atomen ligt in het infrarood.

Figuur S.1: De staart van een komeet ontstaat door stofdeeltjes van de komeet die door licht van de zon worden weggeduwd. Foto van komeet Hale-Bopp die in 1997 langs de aarde vloog.

Koelen met laserlicht Om deze bijzondere kleur goed aan te spreken is een speciale lichtbron nodig die precies de goede kleur licht levert. Normale lampen voldoen niet, omdat hun licht bestaat uit heel veel kleuren. In plaats daarvan gebruiken wij lasers die precies één kleur leveren. Heel toevallig is de kleur licht die de lasertjes in CD-spelers leveren precies de kleur die wij nodig hebben.

In de experimenten die beschreven zijn in dit proefschrift worden veel lasers gebruikt. Allemaal met een iets andere kleurnuance, maar allemaal infrarood, in de buurt van de voorkeurskleur van rubidium. De experimenten beginnen allemaal door zes laserbundels met de goede eigenschappen (intensiteit en kleur) te kruisen in een glazen potje waarin een klein beetje rubidiumdamp zit. Deze zes laserbundels, in combinatie met een goed gekozen magnetische put, zorgen ervoor dat er van alle kanten tegen de atomen wordt geduwd. De atomen verzamelen zich in het kruispunt van de laserbundels en worden tegelijkertijd afgeremd. Een foto van deze opstelling is te zien in figuur S.2.

Omdat op atoomschaal de snelheid van de atomen een maat is voor de temperatuur van gas, wordt het wolkje atomen dus afgekoeld. Voor een gas op kamertemperatuur (20°C of ongeveer 293 Kelvin) is deze snelheid gemiddeld ongeveer de geluidssnelheid, oftewel 300 m/sec. Bij het absolute nulpunt, ($-273,15$°C, oftewel 0 Kelvin, kouder kan niet), staan de atomen helemaal stil. In onze experimenten worden ongeveer 10 miljoen atomen een factor 10.000 afgeremd tot een gemiddelde snelheid van ongeveer 3 cm/sec. Dit komt overeen met een temperatuur van 5 μK (micro-Kelvin), oftewel -273,149995°C. Dit is 0,000005 graad boven het absolute nulpunt en is veel lager dan de temperatuur van het heelal! In 1997 is voor deze koeltechniek de Nobelprijs uitgereikt aan S. Chu, C. Cohen-Tannoudji en W. Phillips. Door deze lage temperatuur, en dus lage snelheid van de atomen, blijft het ingevangen gaswolkje bij elkaar als de laserbundels worden uitgezet. Het wolkje valt door de zwaartekracht naar beneden terwijl het maar minimaal groter wordt. Dit is te zien in de bovenste rij experimentele plaatjes in figuur S.3. Bij hogere temperaturen zou het wolkje direct uit elkaar spatten.
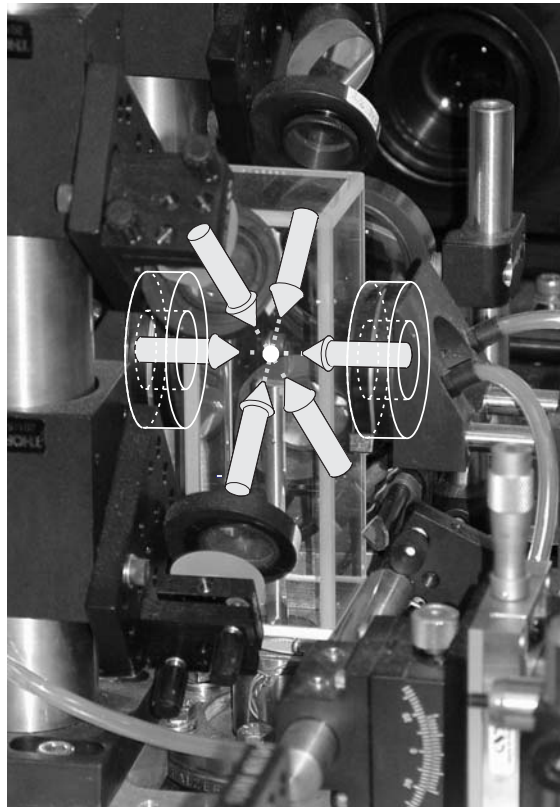
Figuur S.2: Foto van het potje met rubidiumdamp. De zes laserbundels om de atomen in te vangen en af te koelen zijn met pijlen in de foto getekend. De cirkels geven de spoelen aan die de magnetische put maken om de atomen op hun plaats te houden. Ook te zien zijn sommige van de spiegeltjes die de laserbundels het potje in reflecteren.
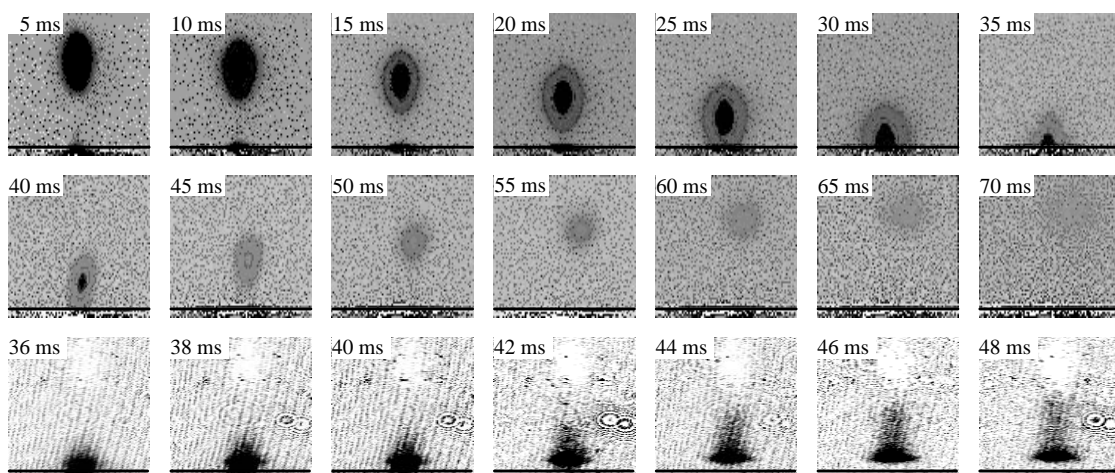
Figuur S.3: (bovenste rij) Een wolkje atomen dat is afgekoeld tot 5 μK valt als een baksteen naar beneden. (middelste rij) De vallende atomen worden afgestoten door een evanescent lichtveld. Dit lichtveld vormt een spiegel voor atomen of een atomaire trampoline. (onderste rij) Als tijdens deze stuitering de atomen worden overgepompt naar toestand $F = 2$ stuiteren ze minder hoog op. De tijd die is aangegeven in de plaatjes is de tijd die verstreken is sinds de atomen zijn losgelaten.
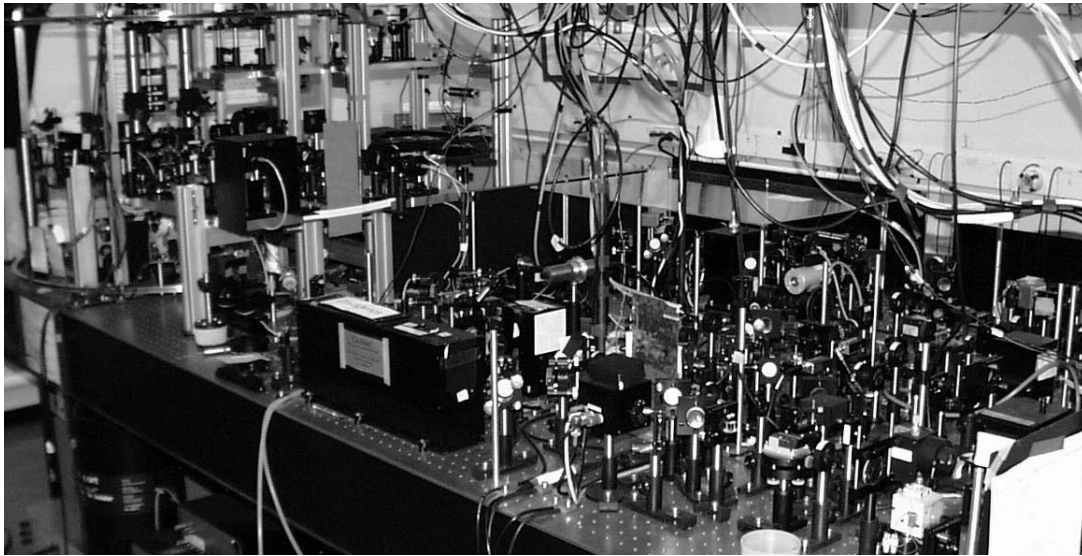
Figuur S.4: Foto van de opstelling. Tafel waarop de lasers en optische elementen staan opgesteld.

Nog kouder   Er is een koelmethode die tot nog lagere temperaturen leidt. Deze koelmethode wordt afdampkoelen genoemd en is gebaseerd op verdampen, net als een kop koffie die afkoelt. Het komt erop neer dat de warmste deeltjes ontsnappen en je daardoor vanzelfsprekend de koudste overhoudt. Bij de temperaturen en dichtheden die op deze manier gehaald kunnen worden treedt een bijzonder effect op. De atomen gaan allemaal hetzelfde gedrag vertonen en het is niet meer mogelijk om ze van elkaar te onderscheiden. Verder gaan de atomen zich steeds meer als golven in plaats van deeltjes gedragen. Dit gedrag wordt Bose-Einstein condensatie genoemd. Het is in 1925 voorspeld door de natuurkundigen Bose en Einstein. In 1995 is het voor het eerst waargenomen. Hiervoor is in 2001 de Nobelprijs uitgereikt aan E. Cornell, W. Ketterle en C. Wieman. Om dit gedrag te beschrijven is quantum-mechanica nodig; de beschrijving van de natuurkunde van het hele kleine. Het gas gaat zich gedragen als een quantumgas. Dit betekent dat alle atomen gaan zich hetzelfde gaan gedragen.

Beïnvloeden van atomen met laserlicht   Een rubidium-atoom kan in twee toestanden voorkomen. Deze toestanden worden genummerd met $F = 1$ en $F = 2$. In onze experimenten is het effect van licht op $F = 1$ atomen veel groter dan op atomen in de $F = 2$ toestand. Verder lijken deze toestanden erg op elkaar. Een atoom kan van de ene in de andere toestand worden gebracht. Ook dat gebeurt weer met behulp van laserlicht. Weer een andere laser wordt gebruikt om atomen waar te nemen door te kijken naar de schaduw die de atomen in de lichtbundel achterlaten.

Voor al deze toepassingen is laserlicht met een iets andere kleurnuance nodig. In ons laboratorium hebben we dan ook een heel park met lasers, optische elementen zoals spiegels en lenzen en electronica om te zorgen dat we al deze kleurnuances kunnen maken. In figuur S.4 is een foto van de tafel te zien waarop al deze lasers en optische elementen staan.
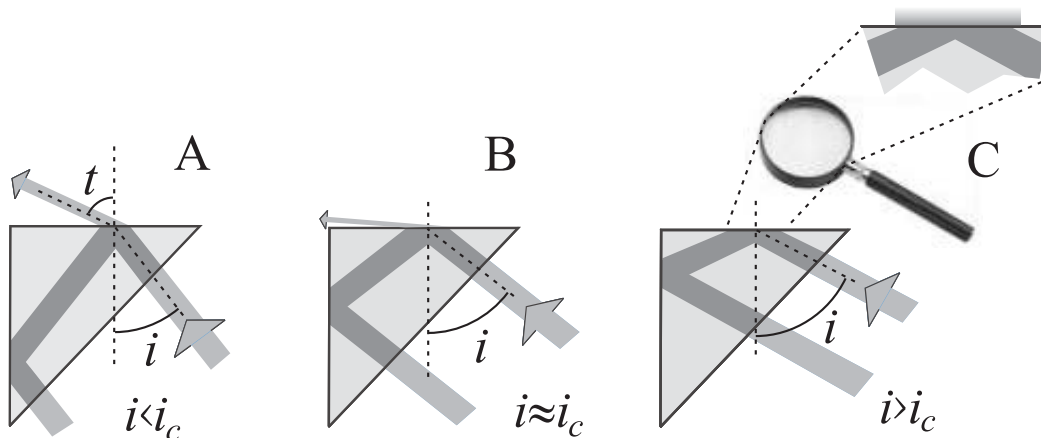
Figuur S. 5: (a) Licht *breekt* aan een oppervlak tussen een dicht (glas) en minder dicht (lucht of vacuüm) medium: de hoek van uittreding t is groter dan de hoek van inval i. (b) Als de hoek van inval i groter wordt, is er op een gegeven moment een hoek i_c waarvoor het uittredende licht parallel aan het oppervlak loopt. (c) Als hoek i nog groter wordt, is er geen uittredende lichtstraal meer, maar alleen een dun laagje licht: een evanescent lichtveld.

Evanescent licht   Naast lasers die gebruikt worden als *lichtstraal*, een bundel licht die door de ruimte loopt, worden ze ook gebruikt om *evanescente* (Nederlandse vertaling: uitdovende) lichtvelden te maken. Deze velden ontstaan als een laserbundel van een optisch dicht medium (zoals glas) verder gaat in een optisch minder dicht medium (zoals lucht of vacuüm). Bij zo'n overgang reflecteert een gedeelte van het licht aan het oppervlak tussen de twee media en een gedeelte van het licht gaat door in het nieuwe, minder dichte, medium. Dit doorgaande licht *breekt* aan het oppervlak. De hoek van uittreding t is groter dan de hoek van inval i, zoals te zien is in figuur S.5(a). Als de hoek van inval i groter wordt, is er op een gegeven moment een hoek i_c waarvoor het uittredende licht parallel aan het oppervlak loopt. Dit is te zien in figuur S.5(b). Als hoek i nog groter wordt, is er geen uittredende lichtstraal meer, maar alleen een dun laagje licht, zoals is weergegeven in figuur S.5(c). Dit wordt een evanescent lichtveld genoemd en heeft hele bijzondere eigenschappen.

Atomen waarnemen met evanescent licht   In de experimenten die beschreven zijn in dit proefschrift valt het wolkje koude atomen op een glazen oppervlak waarboven zo'n evanescent lichtveld is gemaakt. We hebben onder andere een techniek ontwikkelt om met evanescent licht atomen zeer dicht boven het glazen oppervlak waar te nemen. We hebben het hier over afstanden van ongeveer 0.5 μm of 0.0005 mm. Door deze kleine afstand is het heel moeilijk om deze atomen op een andere manier te bekijken.

Spiegel voor atomen   Evanescente velden kunnen niet alleen gebruikt worden om atomen waar te nemen, maar ook om ze te beïnvloeden. Door de kleur van het licht goed te kiezen kan dit evanescente veld afstotend werken voor atomen. Op deze manier kan een atoomspiegel of trampoline voor atomen worden gemaakt. Plaatjes die gemaakt zijn met onze opstelling staan in de middelste rij in figuur S.3. Deze stuitering kan worden beïnvloed (onderbroken) door tijdens de stuitering de atomen over te pompen van toestand $F = 1$ naar toestand $F = 2$. Atomen in deze laatste toestand worden veel minder sterk afgestoten waardoor ze minder hoog opstuiteren. Dit is te zien in de onderste rij plaatjes in figuur S.3.

Vangen van atomen met evanescent licht   Waar we uiteindelijk in geïnteresseerd zijn is het vangen van atomen vlak boven een glazen oppervlak. Dit hebben we gedaan door een lichtveld te maken dat ervoor zorgt dat atomen na het overpompen naar toestand $F = 2$ niet wegstuiteren maar gevangen zitten in dit lichtveld. We hebben experimenten gedaan waarbij het evanescente veld gecombineerd wordt met een bundel licht die van het bovenoppervlak reflecteert. Hierbij is het ons gelukt om de wolk atomen in hele dunne plakjes boven het oppervlak te vangen. Ook hebben we experimenten gedaan met een combinatie van twee evanescente lichtvelden. Deze combinatie levert een lijntjespatroon op waarin atomen gevangen kunnen worden. Omdat de structuren van atomen die we maken één- (lijntjes) of twee-dimensionaal (plakjes) zijn, zullen de atomen een ander gedrag vertonen dan normaal gesproken in drie dimensies.

Door atomen op deze manier te vangen verwachten we dat we de dichtheid kunnen verhogen. Een relatief grote wolk atomen wordt immers samengeperst in een platte schijf of zelfs nauwe lijntjes. Door de dichheid voldoende te verhogen kun je ook een Bose-Einstein condensaat maken. Het is ons gelukt om de dichtheid in de plakjesstructuur te verhogen met een factor 100. Niet genoeg voor een Bose-Einstein condensaat, maar wel ongeveer hetzelfde als andere mensen in een vergelijkbaar experiment hebben behaald. Berekeningen die we gedaan hebben aan de lijntjesstructuren laten zien dat ook hier de grens ligt op ongeveer een factor 100.

Nawoord

Dit hele proefschrift is geschreven in de derde persoon enkelvoud. Uiteraard is dit geen *pluralis majestatis* maar het betekent dat ik dit proefschrift niet had kunnen schrijven zonder de hulp van veel mensen. Allereerst zijn dat natuurlijk mijn promotor en co-promotor Ben van Linden van den Heuvell en Robert Spreeuw. De grote vrijheid die ik gekregen heb tijdens mijn onderzoek heb ik altijd heel erg gewaardeerd. Gelukkig stonden jullie altijd klaar om mee te denken als er problemen waren die ik niet zelf opgelost kreeg. Jullie verschillende aanpak van vraagstukken, een verhelderend analoog fenomeen door Ben en een verklarend subtiel effect dat de onbegrijpelijke resultaten logisch maakt door Robert, leidde meestal snel tot een goed begrip.

Gedurende mijn hele promotie heb ik samengewerkt met een groep leuke collega's: Aaldert van Amerongen, Bas Wolschrijn, Carolijn van Ditzhuijzen, Cor Snoek, Dirk Voigt, Esther Schilder, Iuliana Barb, Jan-Joris van Es, Klaasjan van Druten, Nandini Bhattacharya, René Gerritsma, Rik Jansen, Tycho Huussen, Veronica Ahufinger, Vlad Ivanov en Yu Tao Xing. Cor, jouw enthousiasme en manier van onderzoek doen hebben me direct geïnspireerd. Als er een hulpstuk nodig was dan maakte je dat even, of je haalde iets te voorschijn uit de grote, bijna historische verzameling instrumenten. Klaasjan, je stond altijd klaar om mee te denken. Bedankt voor je opmerkingen over hoofdstuk 3. Dirk, door jouw alom aanwezige initialen heb ik al die tijd niet om je heen gekund. Je originele insteek in discussies was altijd leuk. Bas, samen met jou heb ik lange dagen in het lab doorgebracht. Die dagen waren nooit saai of vervelend en we vulden elkaar perfect aan. Trouwens, *furby* is nog steeds een onderdeel van mijn woordenschat. Aaldert, jou moet ik bedanken voor het feit dat er een hoofdstuk 6 is in dit proefschrift. Als afstudeerstudent was je er zo van overtuigd dat het mogelijk moest zijn om absorptie van evanescent licht waar te nemen dat we gelukkig uiteindelijk een serieuze poging gedaan hebben. Tycho, bedankt voor je bijdrage aan hoofdstuk 5. Vlad, it's your experiment already for some time and it is in good hands. Jan-Joris en Carolijn, jullie zijn begonnen toen ik eigenlijk al klaar was. Succes met jullie projecten. Throughout my Ph.D. period I've shared an office with several people. I want to mention in particular Nandini, Iuliana and René, I couldn't have wished for better office mates. Our serious and less serious talks were always a pleasure. Nandini, your ability to always see things from a positive side has always amazed me. Iuliana, despite all your efforts my pronounciation of *Romani* is still horrible. Tea? René, jij hebt me uiteindelijk overgehaald om de vrijdagavonden een nuttiger invulling te geven.

Soms is apparatuur te koop, heel vaak is het dat niet en moet het speciaal gemaakt worden. Hierbij wil ik alle mensen van de instrumentmakerij, het constructiebureau en de electronica-werkplaats bedanken voor de altijd plezierige samen-

werking. In de instrumentmakerij en het constructiebureau heb ik voornamelijk samengewerkt met Diederik Kwakkestein, Fred van Anrooij, Joost Overtoom, Floris van de Woude, Harry Beukers, Mattijs Bakker (ook bedankt voor al je hulp bij het printen van de vele posters), en Willem van Aartsen. Wim, Fred en Harry, jullie waren altijd bereid om kleine (en zelfs minder kleine) aanpassingen even tussen jullie andere werk door te doen. Dit heeft mij enorm geholpen. Ik ben bang dat door alle reorganisaties mijn opvolgers deze luxe steeds minder zullen hebben. Op de electronica-afdeling heb ik voornamelijk samengewerkt met Alof Wasskink, Ben Harrisson, Edwin Baaij, Frans Pinske, Herman Prins, Johan te Winkel, Peter Waterman, Pieter Sannes en Ronald Nieuwendam. Ik wil jullie bedanken voor al jullie hulp en advies. Alof en Johan, jullie waren geregeld het slachtoffer als ik zelf dingen wilde maken die ik beter aan jullie over had kunnen laten. Maar jullie waren gelukkig altijd bereid om me te helpen als ik vastliep.

Voor de ICT voorzieningen kon ik altijd rekenen op Damien van Zijst, Derk Bouhuijs, Marc Brugman, Marnix Rozenga en Roelof Brandsma. Jullie waren zelfs bereid om me te helpen met mijn privé laptop. Voor advies en hulp op allerlei terreinen kon ik terecht bij Bert Zwart, Flip de Leeuw, Hugo Schlatter, Huib Luigjes, Paul Vlaanderen en Ton Riemersma. Mariet Bos, Rita Vinig en Roos Visser bedankt voor alle hulp bij de contractuele, financiële en administratieve zaken.

Een zwart onderdeel van mijn promotie is de sluiting van het Van der Waals-Zeeman laboratorium vanwege de vondst van asbest in het gebouw en de verhuizing die nu al een paar keer ter sprake is gekomen. Er kon een ruim half jaar niet geëxperimenteerd worden en vervolgens moest de werkende opstelling worden afgebroken en verhuisd naar een nieuwe laboratoriumruimte in een ander gebouw. Dit heeft nog eens een half jaar gekost. Ren Moolenaar bedankt voor al het plan- en regelwerk en Jan Tromp en "de Jantjes" voor de goed verlopen verhuizing. Ik ben nog steeds blij dat die optische tafels niet in de gracht zijn beland. Co Zoutberg en de mensen van de scheikunde-instrumentmakerij bedankt voor het inrichten van de labruimtes.

On a regular basis, but definitely not regularly, there was a *Quantum Collective* meeting, a meeting of atomic physicists working in Amsterdam and surroundings. These meetings I valued both for the exchange of information and for the opportunity to meet people from the Amolf institute and the VU. In this context I want to mention Dima Petrov, Igor Shvarchuck, Jeroen Koelemeij, Jook Walraven, Jora Shlyapnikov, Kai Dieckmann, Louw Feenstra, Norbert Hershbach, Paul Tol, Roland Stas, Stefan Petra, Tom Hijmans, Wim Vassen and Wolf von Klitzing.

Als laatste wil ik de mensen bedanken die privé veel voor me betekend hebben. Chéa, bedankt voor al je steun en de leuke tijd de afgelopen jaren. Ten slotte mijn ouders, voor jullie steun, stimulans en omdat jullie altijd voor me klaarstonden. Bedankt!